Muon induced secondary electrons at the KATRIN experiment
Detector installation and setup & data analysis

Diploma Thesis of

Philipp Rovedo

At the Department of Physics
IKP - Institut fuer Kernphysik - KIT Karlsruhe

Reviewer:	Prof. Dr. Guido Drexlin
Second reviewer:	Prof. Dr. Ulrich Husemann
Advisor:	Dr. Nancy Wandkowsky
Second advisor:	Benjamin Leiber

Duration:: September 27th 2012 – September 27th 2013

I declare that I have developed and written the enclosed thesis completely by myself, and have not used sources or means without declaration in the text.

PLACE, DATE

. . . .

(**YOUR NAME**)

Contents

List of Figures

List of Tables

Die drei Neutrinos, nach der Postulation durch Pauli inzischen etabliertes Elementarteilchen, sind die einzigen Teilchen des Standardmodells, deren Masse bisher unbekannt ist. Zahlreiche Oszillationsexperimente haben gezeigt, dass die Masse nicht null sein kann, finden jedoch nur Zugang zu den Differenzen der Massenquadrate. Die Bestimmung einer dieser Massen, die des Elektron-Neutrino, hat sich das KATRIN Experiment (Karlsruher Tritium Neutrino Experiment) zum Ziel gesetzt. Dabei nutzt es eine, im Gegensatz zu neutrinolosem doppeltem Beta-Zerfall oder kosmologischen Betrachtungen, modellunabhängige Methode. Die Zerfallselektronen des Tritium werden mit Hilfe eines MAC-E Filters

Das Myon detektions System, das in dieser Arbeit beschrieben wird, ist Teil des KATRIN Experiments.

1. Introduction

Ever since the beginning of the 19th century science in general but especially the field of physics has been undergoing an unbelievably quick and vast development. The possibilities arising from automated analysis through the use of advanced computation grids connected to the optimization of manufacturing processes for detectors leave the world - and even scientist - amazed. Nevertheless, with more and more phenomena well understood, the remaining tasks often require huge projects and large collaborations. One of these projects, and a magnificent one at that, is the KATRIN experiment. Working on the project is a liaison of 15 universities and research facilities with over 150 coworkers aspiring to find the absolute neutrino mass scale. So at first, a introduction covering the postulation and discovery of the neutrino as well as latest results from research is given.
Another important topic for this thesis are cosmic rays: Both the particle most significant for KATRIN, the neutrino, and the background inducing muon are generated in different interactions with the atmosphere. That is why a part of this introduction will be devoted to the description of air showers.

1.1. Neutrinos - the early years

The neutrino was not discovered in the conventional meaning but postulated by Wolfgang Pauli, then under the name of “neutron”, as a explanation for the spectrum of the beta decay showing a continous energy distribution which did not concur with the idea of a two body decay [1].

$$\mathrm{p} \longrightarrow \mathrm{n} + \mathrm{e}^- \tag{1.1}$$

Coservation laws of energy, momentum and angular momentum were violated. The neutrino solved this problem by being a carrier of different kinetic energies thus allowing for a continuous spectrum.

$$\mathrm{p} \longrightarrow \mathrm{n} + \mathrm{e}^- + \bar{\nu}_e \tag{1.2}$$

To be compliant with the laws of conversation, the new particle needed to be of spin 1/2 and chargeless. The first experimental evidence for this particle was then given by Cowan and Reines [2] who observed the reaction of electron-anti-neutrinos and free protons in the large neutrino flux of a nearby nuclear reactor.

$$\bar{\nu}_e + \mathrm{p} \longrightarrow \mathrm{e}^+ + \mathrm{n} \tag{1.3}$$

They then looked for two events: a pair of 511 keV photons from electron-positron annihilation as well as the γ from neutron capture some µs afterwards. Following the electron

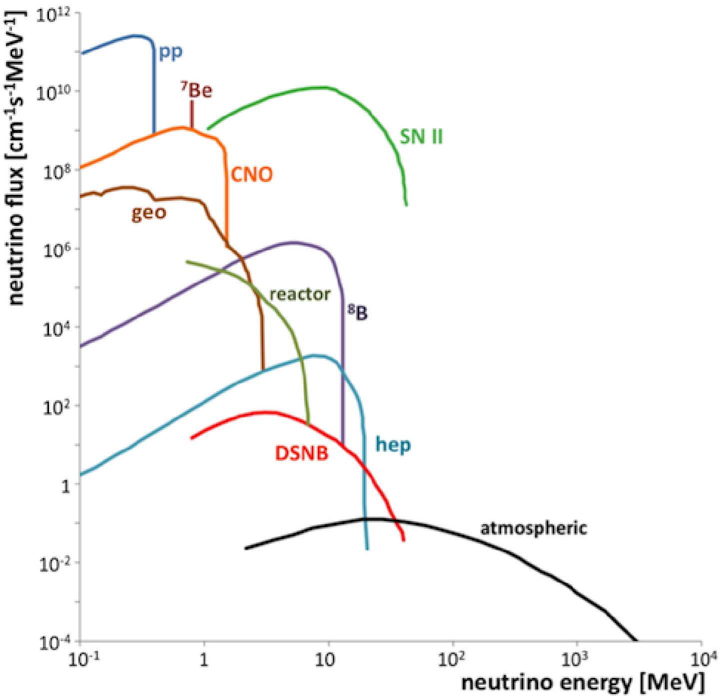

Figure 1.1.:
A graph for different neutrino sources both natural and artificial. In the upper left, solar reactions creating a large integral flux. In the upper mid, the supernovae type II. Peaking at around 10^5 s^{-1} cm^{-2} MeV^{-1}, geoneutrinos. Right of it reactor neutrinos and ^{8}B, the β^+ decaying boron isotope. Following below are the diffuse super novae background, another solar reaction, hep, and, last and least, the atmospheric neutrinos.

neutrino, both other known neutrino generations have been attested for in various experiments, the first ones to find evidence for ν_μ and ν_τ were to be Danby and Gaillard [3] and the DONUT experiment [4] respectively.

1.2. Neutrino sources

Next to the first indicator of neutrinos, the beta decay with its continuous spectrum, many other reactions produce neutrinos besides easily detectable products. An overview over natural sources creating the largest flux through earth as well as experimental sources is given below, figure

- **Primordial neutrinos**
  Lingering around since the "Big Bang", neutrinos with rather low, thermal energies form a cosmic neutrino background at $T_\nu \approx 1.95\,\mathrm{K}$. These neutrinos discoupled shortly after the Big Bang when densities rapidly dropped and with it the weak force's reaction rate that before kept an equilibrium between protons, neutrons electrons and neutrinos. This process of "freezing out" alone leads to a static number density of $336\,\mathrm{cm}^{-3}$ for the sum over all three neutrino flavors.

- **Supernovae neutrinos** Supernovae type II, which occur less often than the type I and only in stars with $M > 8M_\odot$, are known to produce large quantities of neutrinos. Inside the burned out collapsing star, the electrons' degeneracy pressure leads to de-leptonization of the core by electron capture.

$$\mathrm{e}^- + \mathrm{p} \longrightarrow \mathrm{n} + \nu_e \tag{1.4}$$

  This process produces high energy neutrinos leaving the core and carrying away energy in the process - and large quantities of that: about 99 % of the energy released during a type II supernova cooling phase is carried away by neutrinos.

- **Solar neutrinos**
  Our sun's *pp* reaction chain equation (1.5) - dominant in its energy production -

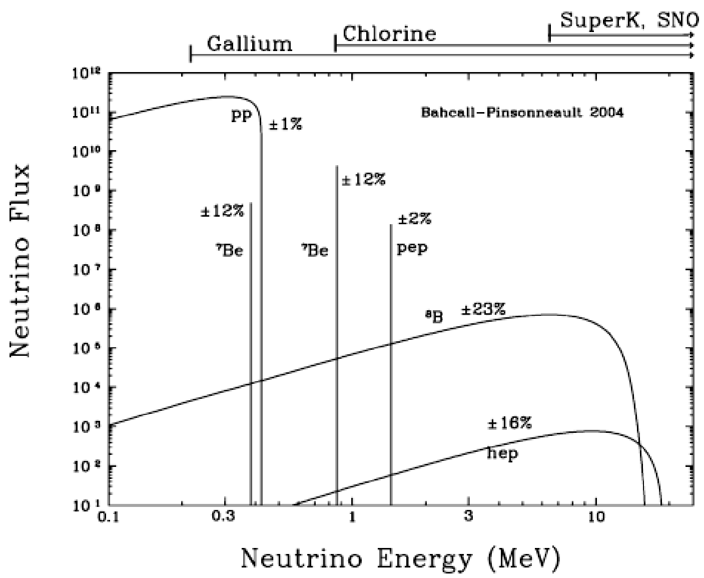

Figure 1.2.: The graph shows the theoretical solar neutrino flux in $\mathrm{cm^{-2}\,s^{-1}\,MeV^{-1}}$ over the neutrino energy - for line sources in $\mathrm{cm^{-2}\,s^{-1}}$. Different processes are shown, the dominant pp process is visible in the upper left. CNO fluxes are dropped in this figure. On the very top, the sensitivities of different experiments are shown.

produces neutrinos in a continuous energy range (upper energy limit given) together with other, less dominant reactions.

$$^1\mathrm{H} + {}^1\mathrm{H} \longrightarrow {}^2\mathrm{He} + \mathrm{e}^+ + \nu_e \qquad (0.42\,\mathrm{MeV}) \tag{1.5}$$

$$^8\mathrm{B} \longrightarrow {}^8\mathrm{Be} + \mathrm{e}^+ + \nu_e \qquad (14.06\,\mathrm{MeV}) \tag{1.6}$$

$$^3\mathrm{He} + \mathrm{p} \longrightarrow {}^4\mathrm{He} + \mathrm{e}^+ + \nu_e \qquad (18.77\,\mathrm{MeV}) \tag{1.7}$$

Further on, electron capture processes add line spectra to the picture

$$^7\mathrm{Be} + \mathrm{e}^- \longrightarrow {}^7\mathrm{Li} + \nu_e \tag{1.8}$$

$$^1\mathrm{H} + {}^1\mathrm{H} + \mathrm{e}^- \longrightarrow {}^2\mathrm{H} + \nu_e(1.55\,\mathrm{MeV}) \tag{1.9}$$

where ^{7}Be emits at two energies: mostly at 0.86 MeV(90 %) and another, lower energy line at 0.38 MeV (10 %) [5]. These reactions are responsible for the largest part of the solar neutrino flux through the earth. Predictions on this flux are shown in figure 1.2 together with other model calculations on flux expectations. Solar neutrinos were essential for oscillation research and by that for the proof that neutrinos are in fact massive (see chapter 1.4).

- **Atmospheric neutrinos**
  As described in section 1.7 cosmic rays, consisting mostly of hadrons, which, in turn, are mostly protons, constantly impact onto the upper layers of the atmosphere. Here, they create air showers, cascades of the initially high energy particles into thousands of particles of lower energies. In that process, not only muons relevant considering background processes in KATRIN, but also neutrinos originate raising the flux through earth.
- **Reactor neutrinos**
  Nuclear fission produces large quantities of neutrons that decay following

$$\mathrm{n} \longrightarrow \mathrm{p} + \mathrm{e}^- + \bar{\nu}_e \tag{1.10}$$

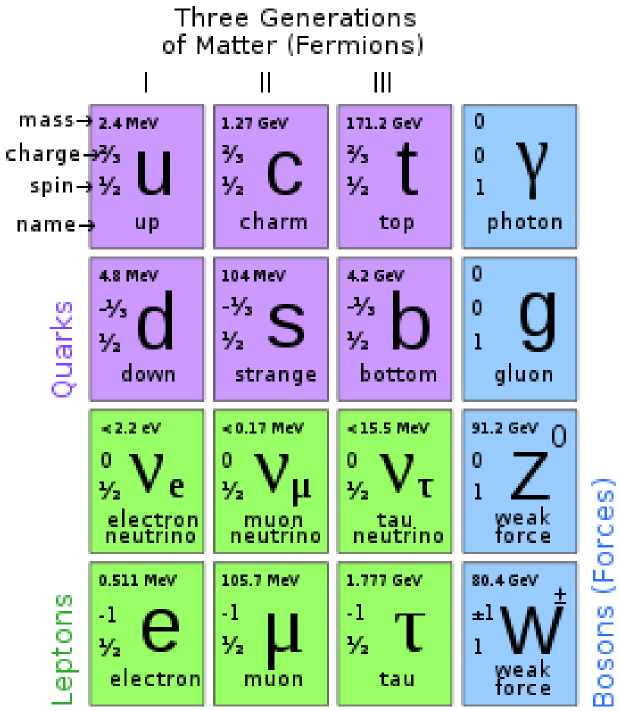

Figure 1.3.: Particles stated in the standard model. On the upper left quarks, on the lower left leptonic particles. The very right row contains the bosonic force particles. Note the absence of the graviton.[9]

A fission reactor, in which many of these reactions concur, is hence a strong source of neutrinos, depending on the reactor's size of course. On an average GW reactor, around 6 neutrinos per fission reaction emerge. These sources are used in many experiments, among other things to prove the existence of neutrino oscillations (see chapter **??**). The Daya Bay experiment for example was able to attest the disapperance of $\bar{\nu}_e$ in a baseline experiment [6].

- **Neutrinos from β decays**
  Very important for the KATRIN experiment are neutrinos from beta decays, more precisely the tritium beta decay. This is described in more detail in chapter 2.1.

1.3. Neutrinos in the standard model

During the second part of the 20th century, a model stating 16 particles has been developed to describe a huge portion of known phenomena - the standard model. It contains six quarks and six leptons (both made up of three particle generations) making up the matter as well as four types of Gauge Bosons. The latter are carriers of the standard model's interactions of the former particles, meaning all interactions of matter are based on the exchange of one or more of the Gauge Bosons. Lately, proof for the Higgs particle, a scalar boson, stated as a carrier of mass seems to have been found at CERN [7, 8]. It is the last particle to complete the standard model. For our universe, gravity, the graviton generated force, plays a major role for formation and stability of almost all larger structures. In particle physics however, it can mostly be neglected. Here, only the strong and weak as well as the electromagnetic interaction make for noticeable contributions to phenomena observed. That is why, in the standard model, gravity as well as its carrier, the graviton, are disregarded.

Most of what we can observe with our bare eyes or in basic experiments is attributable to the electromagnetic force or gravity, however, strong and weak interaction do play a major role when it comes to high energy physics. Here, the limited reach of the two is overcome by small distances between interacting particles. In case of the neutrino, detection and by that the study of its characteristics is even more difficult as it interacts only gravitationally and weakly. Now, as mentioned before, gravity is indeed long range, but very weak in force. And although weak intraction is a lot stronger compared to gravity, it is still weak compared to both electromagnetic and strong interactions. That is why the neutrino is considered elusive, detection efficiencies are low and only large scale detectors are able to detect statistically relevant amounts of neutrinos. One method used quite frequently is the Cherenkov radiation emitted by particles travelling through matter at speeds above the speed of light. The occuring cones of light, comparable to the supersonic cones planes cause in air, can be detected by standard photomiltiplier tubes. The problem is that, as mentioned above, the volumes to be able to make dependable statements on directions and energies need to be large. This is why most experiments make use of "natural" detectors such as water [10] or even ice [11]. Other approaches are to catch neutrinos in reactions where those are required such as inverse beta decays in reactors

$$\bar{\nu}_e + \mathrm{p} \longrightarrow \mathrm{e}^+ + \mathrm{n}. \tag{1.11}$$

In the standard model, neutrinos are considered massless. Many experiments though have shown that the weightless neutrino is a wrong assumption. Most of these were experiments proving neutrino oscillations with both reactor neutrinos and solar neutrinos such as Kamiokande[12], the Daya Bay experiment [13] or SNO [14]. Important for those experiments is the known source location making baseline analysis possible.

Up till now, only the differences of the squared masses are known. This leads to different relations depending on how masses are distributed between the flavors, see figure 1.4, and how large they are absolutely, see figure 1.5. This problem is solved by the knowledge of one of the masses. KATRIN is on the verge of finding the ν_e's mass. Two mass schemes are possible: the normal and the inverted one. Normal means that the smallest number also describes the smallest mass state, i.e. $m_{\nu_1} < m_{\nu_2} < m_{\nu_3}$. In the inverted scheme, the squared mass difference of eigenstates two and three is not directed upwards, but pushes the m_{ν_3} mass below the other two.

1.4. Neutrino Oscillations

If the neutrinos were without mass, its mass eigenstates would equal its flavor eigenstates. First doubts concerning this assumptions occurred as inconsistencies between the measured and the calculated solar ν-flux occurred at the Homestake mines [15]. As the count on ν_e was too low, the theory of neutrino oscillations emerged, stating that a mixture of flavors was possible as the flavors were made up of all three of the mass eigenstates. The mixture is described by the so called Pontecorvo-Maki-Nakagawa-Sakata matrix:

$$\begin{pmatrix} |\nu_e> \\ |\nu_\mu> \\ |\nu_\tau> \end{pmatrix} = \begin{pmatrix} U^*_{e,1} & U^*_{e,2} & U^*_{e,3} \\ U^*_{\mu,1} & U^*_{\mu,2} & U^*_{\mu,3} \\ U^*_{\tau,1} & U^*_{\tau,2} & U^*_{\tau,3} \end{pmatrix} \begin{pmatrix} |\nu_1> \\ |\nu_2> \\ |\nu_3> \end{pmatrix} \tag{1.12}$$

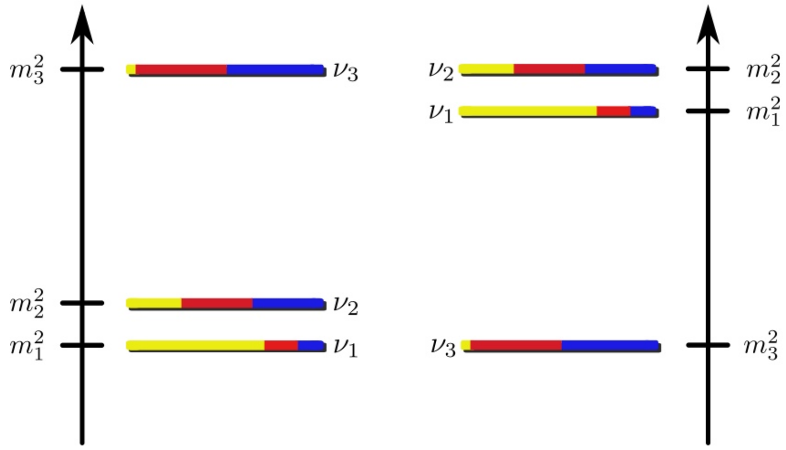

Figure 1.4.: The possible mass hierarchies for neutrinos. Left, the normal scheme with $m_{\nu_1} < m_{\nu_2} < m_{\nu_3}$, on the right the normal scheme where $m_{\nu_1} < m_{\nu_2}$ is still true, though both $m_{\nu_3} < m_{\nu_1}$ and $m_{\nu_3} < m_{\nu_2}$. The colored bars represent the matrix elements for each flavor, i.e. the probabilities of measuring the mass eigenstate while detecting a pure flavor. Yellow stands for ν_e, red for ν_μ and blue for ν_τ.

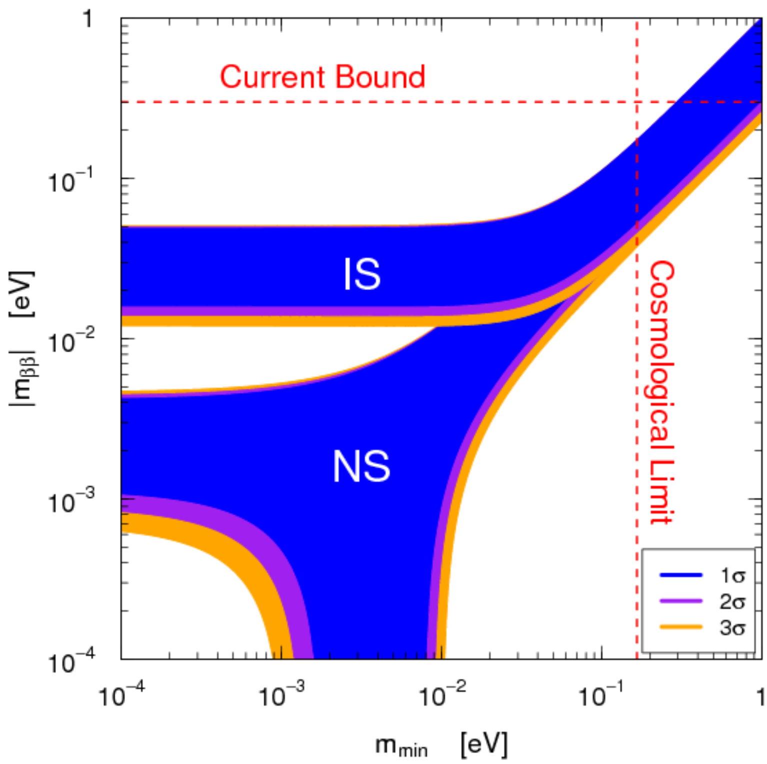

Figure 1.5.: The possible effective masses for neutrinos depending on the lightest neutrino mass m_{min} shown on the x-axis. Normal and inverted scheme are marked NS and IS. The current bound from $0\nu\beta\beta$ decay is displayed as well as cosmological limitations.

parameter	value
$\sin^2(2\Theta_{12})$	0.875 ± 0.024
$\Delta m^2{}_{21}$	$(7.50 \pm 0.20) \times 10^{-5}\,\mathrm{eV}^2$
$\sin^2(2\Theta_{23})$	>0.95
$\Delta m^2{}_{32}$	$(2.32 \pm 0.12)\,\mathrm{eV}^2$
$\sin^2(2\Theta_{13})$	0.095 ± 0.010

Table 1.1.: Given are the latest known mixing angles and squared mass differences. For $\sin^2(2\Theta_{23})$, the lower limit is given.

Though mixing angles are known pretty well, there are still experiments being built that challenge the current error margins such as the LENA experiment which might be able to raise the precision of the mixing angle Θ_{12} by a factor of 10 and may even find the still unknown mixing angle Θ_{13} ([17]).

In this equation, the matrix U can be parametrized through a combination of three rotation matrices and a complex phase factor δ_D as well as two complex majorana phases δ_M

$$U = \begin{pmatrix} 1 & 0 & 0 \\ 0 & c_{23} & s_{23} \\ 0 & -s_{23} & c_{23} \end{pmatrix} \begin{pmatrix} c_{13} & 0 & s_{13}e^{-i\delta_D} \\ 0 & 1 & 0 \\ -s_{13}e^{-i\delta_D} & 0 & c_{13} \end{pmatrix} \cdot \\ \cdot \begin{pmatrix} c_{12} & s_{12} & 0 \\ -s_{12} & c_{12} & 0 \\ 0 & 0 & 1 \end{pmatrix} \begin{pmatrix} e^{i\delta_{M1}} & 0 & 0 \\ 0 & e^{i\delta_{M2}} & 0 \\ 0 & 0 & 1 \end{pmatrix} \tag{1.13}$$

where $c_{ij} = \cos\theta_{ij}$ and $s_{ij} = \sin\theta_{ij}$.

Now the pure eigenstate of a neutrino for t=0 can be described by three matrix elements and the corresponding mass eigenstates.

$$|\nu(t=0)\rangle = |\nu_\alpha\rangle = U^*_{\alpha 1}|\nu_1\rangle + U^*_{\alpha 2}|\nu_2\rangle + U^*_{\alpha 3}|\nu_3\rangle \tag{1.14}$$

The time evolution of this state now reveals the oscillations of the neutrino from flavor to flavor, as the time evoluted states are not flavor eigenstates for every point in time.

$$|\nu_\alpha(t>0)\rangle = U^*_{\alpha 1}e^{-iE_{\alpha 1}t}|\nu_1\rangle + U^*_{\alpha 2}e^{-iE_{\alpha 2}t}|\nu_2\rangle + U^*_{\alpha 3}e^{-iE_{\alpha 3}t}|\nu_3\rangle \neq |\nu_\alpha\rangle \tag{1.15}$$

This means that the probability to find a state different from the initial one is non-zero for most times.

$$|\nu_\alpha(t)\rangle = \sum_{k=1,2,3} U^*_{\alpha k}\exp(-iE_k t)|\nu_k\rangle \tag{1.16}$$

for every state $|\nu_\alpha\rangle$. If the mass eigenstates in turn are expressed as a mixture of flavor eigenstates, one can extract the prefactor of the sums components as the transition probability for each single flavor:

$$P(\nu_\alpha \to \nu_\beta) = |\langle\nu_\beta|\ \nu_\alpha(t)\rangle| = \left|\sum_{k=1,2,3} U^*_{\alpha k}\exp(-iE_k t)U_{\beta k}\right|^2 \tag{1.17}$$

Various baseline experiments have found results for all mixing angles except Θ_{23} for which a lower limit is known according to [16]

1.5. Indirect measurement of neutrino mass

One approach to get access to the neutrino mass is on indirect ways, i.e. using data that is affected by neutrinos but does not directly involve them. Two main techniques are to be indicated here.

First, the search for neutrinoless double beta decay, $0\nu\beta\beta$. The double beta decay $2\nu\beta\beta$ in which two neutrinos are emitted only occurs if the single β decay is prohibited by a heavier ${}^{A}_{Z+1}X$ core and follows the equation

$$ {}^{\mathrm{A}}_{\mathrm{Z}}\mathrm{X} \longrightarrow {}^{\mathrm{A}}_{\mathrm{Z+2}}\mathrm{X} + 2\,\mathrm{e}^- + 2\,\bar{\nu}_e. \tag{1.18} $$

Compared to this $2\nu\beta\beta$ decay the $0\nu\beta\beta$ decay can exist only if the neutrino is its own anti-particle, a so called Majorana neutrino. Then, if a nucleus double beta decays, the neutrino from one vertex can be absorbed in the second as an anti-neutrino with inversed helicity - or vice versa. As this change in helicity is only possible for a massive particle, the $0\nu\beta\beta$ decay would be further proof of a massive neutrino. Furthermore, as the probability for a helicity change is correlated to particle mass the rate, and with it the half life $t_{1/2}$, would depend on the effective Majorana neutrino mass square [18].

$$ \Gamma_{0\nu\beta\beta} \propto \left| \sum U_{ei}^2 m\left(\nu_i\right) \right|^2 \tag{1.19} $$

Secondly, the problem can be approached by calculations using astrophysical data.
For one, the formation of galaxies and other structures in the universe depends on the neutrino mass. In the formation, neutrinos wash out the structures as they act as hot dark matter. A galaxy's power spectrum's fluctuation is supressed by massive neutrinos. Using long term spectroscopic galaxy surveys like SDSS[19] or studying the cosmic microwave background like WMAP [20] or Planck [21], a upper limit of 0.6 eV on $\sum_\nu m_\nu$ can be given.
As the indirect methods for neutrino mass measurements depend at least to some point on model assumptions, the direct methods in the next section play a key role in finding standalone values or limits for neutrino mass.

1.6. Direct measurement of neutrino mass

Direct measurements of the neutrino mass require a reaction known to include neutrinos in its equation, usually the previously mentioned β decay. Advantageous for direct measurements is the only assumption made is the applicability of the relativistic energy-momentum-relation $E^2 = m^2c^4 + p^2c^2$. This makes the results mostly model independent. There are both spectrometric and calorimetric approaches. While the scale of spectrometers is getting bigger and bigger, calorimetric approaches seem to be a reasonable alternative, although the slow detector response - the detector material itself is decaying - requires for large arrays of detectors leading to extensive space requirements as well at some point. The luminosity of spectrometer experiments though is unachieved by any other. That is why the KATRIN collaboration is working on a setup to measure electrons from Tritium decay to determine the neutrino mass. Tritium is advantageous for several reasons listed below.

- A high luminosity is ensured by the short half life of $t_{1/2} = 12.3\,\mathrm{a}$. This makes small amounts of the emitter sufficient to ensure good statistical results.
- At the same time, the inverse of the cubic endpoint energy $(1/E_0^3)$ defines the amount of electrons emitted in the endpoint region (up to 1 eV below the endpoint). Tritium's low endpoint energy of 18.6 keV, undercut only by one β emitter, rhenium, that has other disadvantages, ensures high luminosity at the detector.

- According to [22], as the tritium beta decay is superallowed , the matrix element $|M_{had}|$ is energy independent making corrective energy calculations unnecessary. This simplifies analysis procedures.
- Another simplification compared to different emitters is the easily calculable electron shell configuration. Excited states and their energies are accessible in theory for all decaying particles.
- As far as scattering is concerned, tritium is a well suited material as well. Its low atomic number makes for small cross sections for inelastic scattering. This reduces energy smearing inside the source volume.

These reasons make tritium the element of choice for KATRIN.

The above mentioned rhenium is used in the calorimetric approach. Experiments like MARE [23] use rhenium in bolometers as both emitter and detector. The lower endpoint energy of 2.47 keV guarantees a rather big fraction of electrons with energies near the endpoint, but this is largely compensated for by the much longer half life of $t_{1/2} = 4.32 \times 10^{10}$ a. Still, the mass of rhenium required to gain statistically relevant results remains below the tritium mass used in KATRIN. The MARE strategy is to split the radioactive material and use it in many small microbolometers. That is benefitial as readout is slow and the rate per bolometer is reduced by lowering the emitter mass. Thermistors then sample the temperature catching peaks induced by electrons from β decays scattering inside the solid source. The experiment set up by the Milano collaboration has set upper limits of

$$m_{\bar{\nu}_e} < 15\,\mathrm{eV} \text{ at } 90\,\%\,\mathrm{C.L.}. \tag{1.20}$$

This limit shall be pushed to 0.2 eV according to [23].

1.7. Cosmic rays from the viewpoint of KATRIN

When high energy particles hit the upper parts of the atmosphere, a cascade of particles generated from the interaction with atmospheric molecules and atoms follows. Most primary particles are nucleons, most of which again are free protons (85%), i.e. Hydrogen ions, followed by α particles (15%). Helium nucleons' fluxes are already about an order of magnitude below the hydrogen ones, higher mass number nuclei show even lower rates, see figure 1.6 [24]. **(insert right side graphic from TODOR)** By different forms of interaction, roughly dividable into the three groups of electromagnetic, inelastic hadronic and nuclear phenomena, secondary particles are created [24, 26]. **ToDo**

- **Nuclear fragmentation**
  For very high energy primary particles above the separation energy E_s according to

$$E_s \simeq E_b(N,Z) - E_b(N_F,Z_F) - E_b(N-N_F,N-Z_F) - \frac{Z_F(Z-Z_F)}{(A-F)^{1/3}} \tag{1.21}$$

  it is possible to fragment a nucleous. The first three terms describe the binding energies of the nuclei involved, the last term accounts for the coulomb barrier. Of course, especially for higher order nuclei, more effects become relevant and one has to rely on empirical descriptions of the problem.
- **Inelastic hadronic interaction**
  For high energies, quantum chromo dynamics describe the interactions of particles pretty well, while for energies below 1 TeV one has to rely on phenomenological descriptions. These interactions are prominent in the production of secondary particles like pions or kaons.

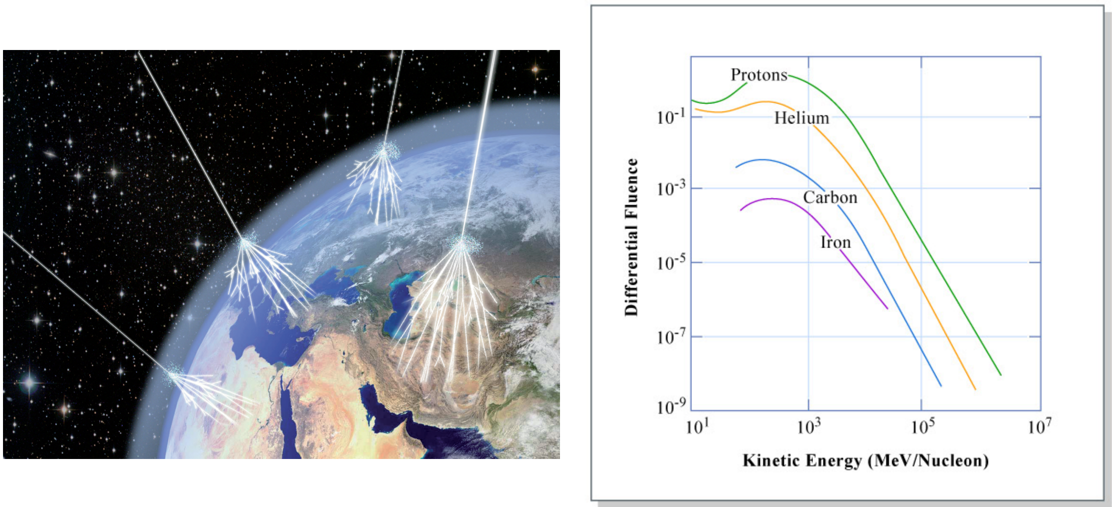

Figure 1.6.: On the left, an artistic impression of various cosmic rays hitting the atmosphere [25]. On the right, the measured composition for cosmic nuclei is shown: on top, the lightest particle, the proton. further down, all with orders of magnitude smaller rates, heavier ions, figure from [24].

- **Electromagnetic interaction**
  The electromagnetic component is the main interaction channel for lighter, charged particles like muons or electrons but also for photons. As the propagation of muons is especially important here, these interactions will be described in some more detail.

  - **Coulomb scattering**
    If one charged particle passes another, it is deflected in its field according to

    $$\tan\frac{\theta}{2} = \frac{zZe^2}{Mv^2 b} \tag{1.22}$$

  - **Ionization losses**
    Through ionization and excitation of molecules, incident particles loose energy in a medium, in this case the atmosphere, according to

    $$\frac{dE}{dx} = -\frac{N_A Z}{A}\frac{2\pi\left(ze^2\right)^2}{M'nu^2}\left[\ln\frac{2Mv^2\gamma^2}{W}I^2 - 2\beta^2\right] \tag{1.23}$$

    Z is the atomic, A the mass number of the medium, I the average ionization potential. N_a is Avogadro's number, ze the particle charge, v its velocity and M its mass. $\beta = v/c$ and $\gamma = 1/\sqrt{1 - /\beta^2}$ and W the maximum energy deposit [27].
    This is the effect used for muon detection in the KATRIN experiment, see 3.

  - **Compton scattering & inverse compton effect**
    Compton scattering is the photonic counterpart to ionization by charged particles. In the process, a photon interacts with bound electrons and excites or ionizes the corresponding atom. In the process the photon looses energy shifting it towards longer wavelengths.
    The inverse compton effect, as the name suggests, describes a photon gaining energy from an atom's hull electron.

  - **Bremsstrahlung & synchrotron radiation**
    When charged particles are deflected in electric fields, photons are emitted and

the particle looses energy. The same is applicable for magnetic fields, where the effect is called synchrotron radiation and a time dependent energy loss occurs. The total energy loss for electric fields can be described by

$$\frac{dE}{dx} = \frac{4N_A Z^2}{A} \alpha r_e^2 E \ln\left(183 Z^{1/3}\right) = \frac{E}{X_0} \tag{1.24}$$

where the radiation length has been introduced to describe the average matter necessary for a particular Energy loss.

- **Electron-positron creation**
  A photon of sufficient energy (2 x 511 keV) can create a electron-positron pair either in the field of an atom's electron hull or in the field of its core. With higher energies, other particles can be created considering the known conservation laws. This proccess can be seen as the inverse bremsstrahlung, assuming the outgoing anti-particle to be its time inverted particle. The energy loss can be described similarly and scales with the incident particle's energy linearly.

- **Cherenkov radiation**
  Much lower amounts of energy are lost in the creation of cherenkov light. The process is particularly important though as it makes for easily detectable particle indicators. Cherenkov radiation occurs when particles move through matter at speeds above the phase velocity of light c/n for a refractive index n. As the atmospheric refractive index is only slightly above 1, particles need to be super-relativistic to emit cherenkov light.

After cascading mostly through multiple intermediate particles, at sea level about 80 % of the cosmic particles are muons. These are super-relativistic due to their small masses though high energies. Even at these high speeds, the muons' average decay time of around 2.2 µs [28] is too small for many muons to reach the earth's surface from our reference frame's point of view. In the most common production height of 2 km [29], the non relativistic time of flight for a 90 % speed of light particle would be

$$t_{class} = 2\,\mathrm{km}/0.9 \cdot c = \tag{1.25}$$

meaning only time dilation from special relativity makes the muon flux as large as it is:

$$t_{rel} = t_{class}/\sqrt{1 - 0.9^2} \tag{1.26}$$

which, from our reference frame, prolongs the lifetime by a factor of around 5, being already enough to reach the surface from heights of 3 km. Most muons have even higher energies, making it possible for them to reach surface from greater heights and under non perpendicular angles towards it. For KATRIN, this poses a problem. A smaller flux would be advantageous, as muons may cause emission of electrons from the spectrometer vessels surface. Shielding against muons is difficult as it requires thick layers of dense matter due to the muons high energies and the low deposition in matter in relations to those. The fluctuation of energy deposition of a charged particle as the muon in matter can be described by the landau distribution that is parametrized as follows [26].

$$L(E) = \frac{1}{2\pi} \exp\left\{-\frac{1}{2}\left(E - \hat{E} + \exp\left(-(E - \hat{E})\right)\right)\right\} \tag{1.27}$$

$\hat{E}$ is the most probable energy deposition value. The analytic distribution is shown in figure 1.7. The muon modules show that distribution as expected, see 3 for details.

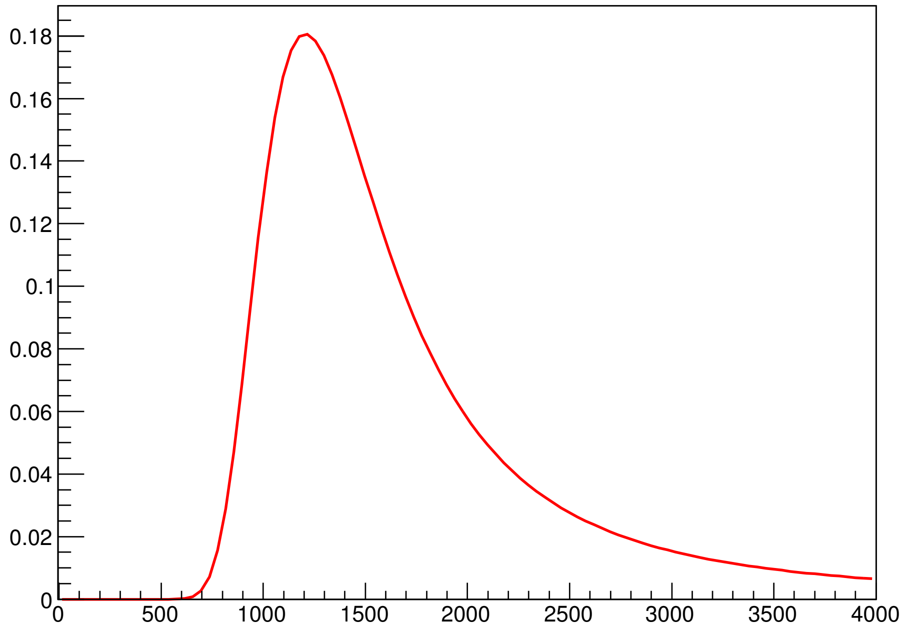

Figure 1.7.: Analytic landau distribution as implemented in the ROOT software. $\hat{E}$ was set to 1200.

2. KATRIN experiment

The KATRIN experiment is on its way to measure the neutrino mass or set new upper limits at precisions never achieved before. It will reach a sensitivity of $200\,\mathrm{meV/c^2}$ at $90\,\%$ C.L. excelling the previously best experiments of Mainz and Troisk by a factor of 10. Major challenges of the project are the requirement of ultra high vacuum, the exact knowledge of all magnetic and electric fields as well as external influences on those, the required high luminosity of the tritium source and the classification and reduction of background sources.

2.1. Measurement principle

A generally easy principle is used to find information on the neutrino mass. The energy of electrons from tritium decay is measured with high precision and compared to the standard model's presumption for a massless neutrino [30]

$$ {}^{3}_{1}\mathrm{T} \longrightarrow {}^{3}_{1}\mathrm{H}^{+} + \mathrm{e}^{-} + \bar{\nu}_{e}. \tag{2.1} $$

As the decay's energy is distributed between the constant neutrino's rest mass and the neutrino's and the electron's kinetic energies respectively, the decay electrons will show a continuous spectrum. The difference between the electron energy calculated by standard model presumptions and the extrapolated maximum electron energy from the spectrum is extracted. As all three mass eigenstates contribute to the electron neutrino's mass in any scenario (see 1.4, the difference will be a superposition of these. The knees occuring at each single eigenstates mass can not be resolved with the KATRIN spectrometer as the energy resolution is larger than the root of the squared mass differences. shown in figure 2.1. As all three flavors contribute to the electron neutrino's mass, what will be measured is the incoherent sum of all three as described in chapter 1.3.

A different light is shed on the simplicity of the task when considering the needed accuracy of $\Delta E < 0.93\,\mathrm{eV}$ needed for the electrostatic filter to achieve the desired sensitivity [31]. And this is just one in a meshwork of requirements necessary. All components need to work as a whole in the end, not a single one may contribute to the background much more than expected.

2.1.1. MAC-E Filter

To measure the energy of electrically charged decay electrons at high precision, an electrostatic filter comes to mind. As the electrons are emitted isotropically, they will have

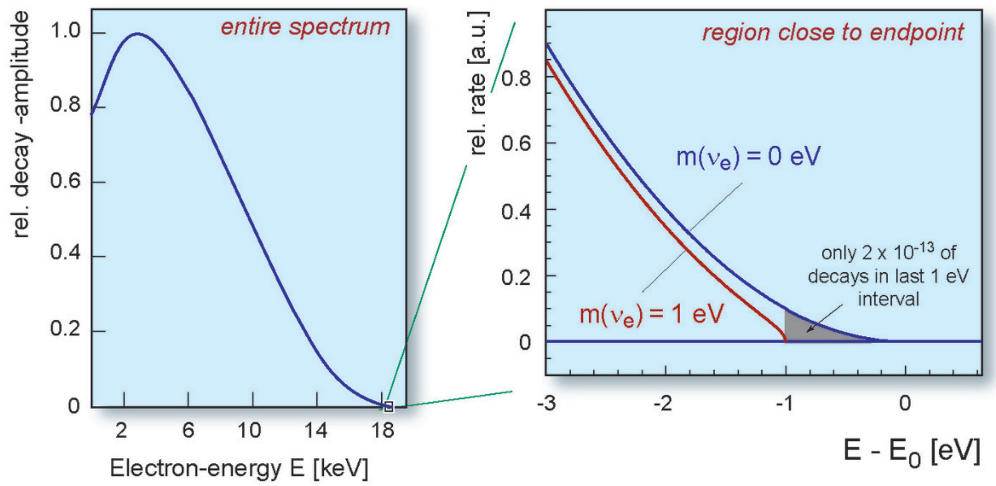

Figure 2.1.: Schematic energy spectrum for electrons from tritium beta decay. On the left, the entire spectrum with the peak at the energy most emitted - around 5 eV - can be seen. On the right, a zoom-in on the endpoint showing both the calculations for a massless and a 1 eV neutrino. As described in the graph, rates in this region are extremely low and extrapolation through advanced software tools needs to be applied.

momentum components both parallel and perpendicular to the source-detector axis (defined as the z-axis). To make statements on the overall energy, the momentum direction needs to be well defined. In case of an electrostatic filter, it needs to be parallel to the electric field to be analyzed. At the same time, a high luminosity is a major requirement for good statistics for the KATRIN experiment. To satisfy all these requirements, several techniques are combined in the MAC-E filter - magnetic adiabatic collimation with electrostatic filter [33].

Magnetic fieldlines connect the source and the detector. Electrons from tritium decays are guided from source side to detector in cyclotron motion around one of these field lines. This strongly raises luminosity as electrons with large angles towards the z axis will not necessarily hit the wall of the source but will be able to reach the detector.

Adiabatic motion in the magnetic field is defined by the allowance of momentum direction changes at constant momentum value. That is given if the magetic field change is small within each cyclotron orbit. If so, the magnetic momentum μ correlated to $E_\perp$ (the energy perpendicular to the magnetic field B) as follows remains constant

$$\mu = \frac{E_\perp}{B} = const \propto \frac{p_\perp^2}{B}. \tag{2.2}$$

Collimation in a MAC-E filter is based on the above adiabacity. Magnetic field strengths drop over several orders of magnitude from B_{max} at the solenoid magnets to B_{min} in the analysis plane (see figure 2.2). Considering equation 2.2, this means that the energy perpendicular to the magnetic field must drop over the same order of magnitude for μ to remain constant. This leads to a parallelization of momentum vector and B-field direction.

Electrostatic filtering occurs exactly at that point of minimal energies $E_\perp$ in the analysis plane. Here, the momentum vector is mostly defined by its component parallel to the

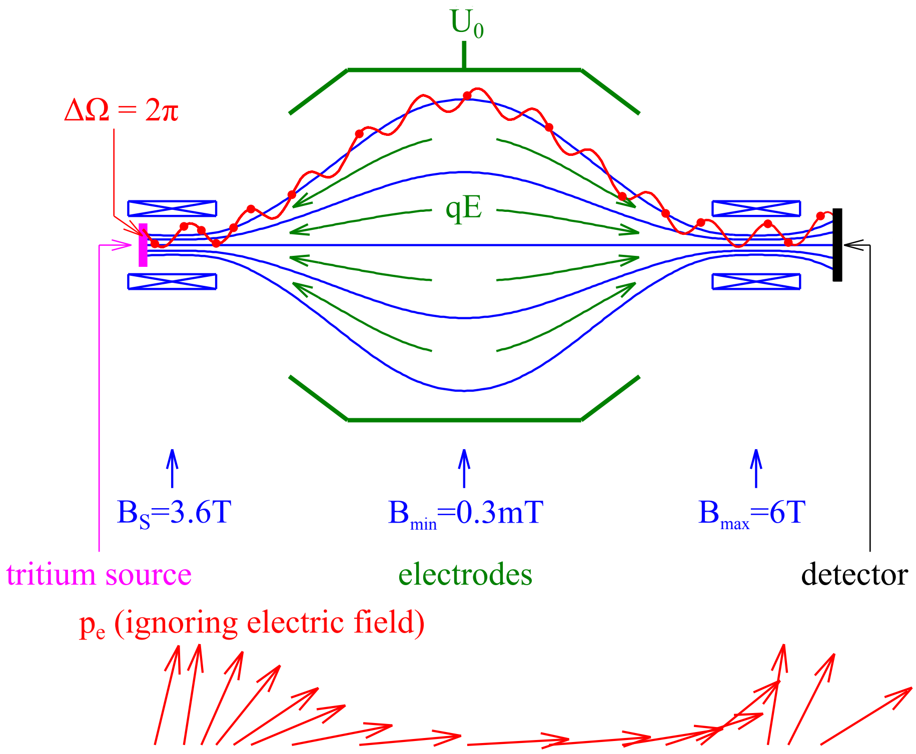

Figure 2.2.: Principle of a MAC E filter. In the upper part, magnetic fieldlies are plotted in blue together with fieldstrengths at the source (3.6 T) and inside the pinch solenoid (6 T). The accepted solid angle and a exemplary particle path are shown in red. The analysis plane is defined by the area of minimum magnetic fields B_{min}. Below, the momentum of an electron with a large starting angle towards the magnetic field lines is shown. It is tipping over as the field weakens. Meanwhile, the vessel voltage U_0 analyses the energy parallel to the electric field passing only electrons with large enough energies on to the detector [32].

magnetic field $E_{||}$. Setting the electrostatic filter to a fixed voltage U now reflects electrons with $E_{||} < U \cdot e$.
Most electrons are emitted at the source are non-parallel to the magnetic field lines and thus an energy $E_{\perp} \neq 0$. That means that it is very likely that electrons in the analysis plane have remaining energy $E_{\perp}$. This limits the filter resolution, with

$$\mu_{low} = \frac{E_{\perp min}}{B_{min}} = \frac{E_{\perp max}}{B_{max}} = \mu_{high} = \mu \tag{2.3}$$

the relative sharpness is given by the maximum transversal energy $E_{\perp max}$ that is still accepted in the filter. As for a

$$\Delta E = E_{\perp max} = E_0 \frac{B_{min}}{B_{max}} \tag{2.4}$$

Only in the edge case of $B \to 0$ in the analysing plane, the momentum would need to be exactly parallel to the field and the resolution would not be limited. After passing the analysing plane, the electrons are reaccelerated by the electric field and guided and focused onto a detector. To additionally dismiss electrons with large starting angles towards the magnetic field, the source field strengthsare chosen to be smaller than the maximum field strength inside the solenoid. This ensures that electrons with long paths that are more likely to scatter will not be analyzed through the effect of magnetic mirroring [34]. With the chosen settings, this results in an angular acceptance of 50.77°. The main spectrometer reaches a resolution of 0.93 eV (see section 2.2.4 for more details).

2.2. Experimental Setup

The KATRIN experiment is made up of different sections all fulfilling their own important purpose in the whole setup. All begins at the windowless gaseous tritium source "WGTS". Here, tritium decays isotropically emitting electrons. These are guided magnetically through the differential and cryogenic pumping sections "DPS" and "CPS" removing hydrogen ions and other residual gases in the process. At the same time, looking at the WGTS from the other direction, the rear section scans the activity of the source. For the electrons on their way to the detector, the path continues through the two spectrometers posing as a energetic high pass filter to the focal plane detector "FPD" registering them.
During the whole procedure, the electrons from the decay may not undergo energy changes as the knowledge of their kinetic energy after decaying is essential to the experiment. That is why the guiding needs to be adiabatic. This is guaranteed by spatially slowly changing and timewise very constant magnetic fields.
See figure 2.3 for a schematic overview of the whole experimantal setup. It follows a more detailed description of the individual components.

2.2.1. WGTS and Rear Section

To generate tritium decay electrons, a gaseous tritium source is utilized (see figure 2.4). Advantages of the principle are the absence of solid state effects and a high luminosity [35]. In a solid, like tritium films, most electrons from decays inside the structure would interact with the solid itself. That could lead to energy shifts threatening the energy resolution. Another advantage of using a gaseous source is that not only the surface facing the detector emits electrons at the required spectrum, but the electrons from the whole volume covered by the magnetic flux tube hitting the detector can be analyzed. Furthermore, the emission of this kind of source is very homogeneous. Of course, new challenges arise from the decision to use gas instead of solids.

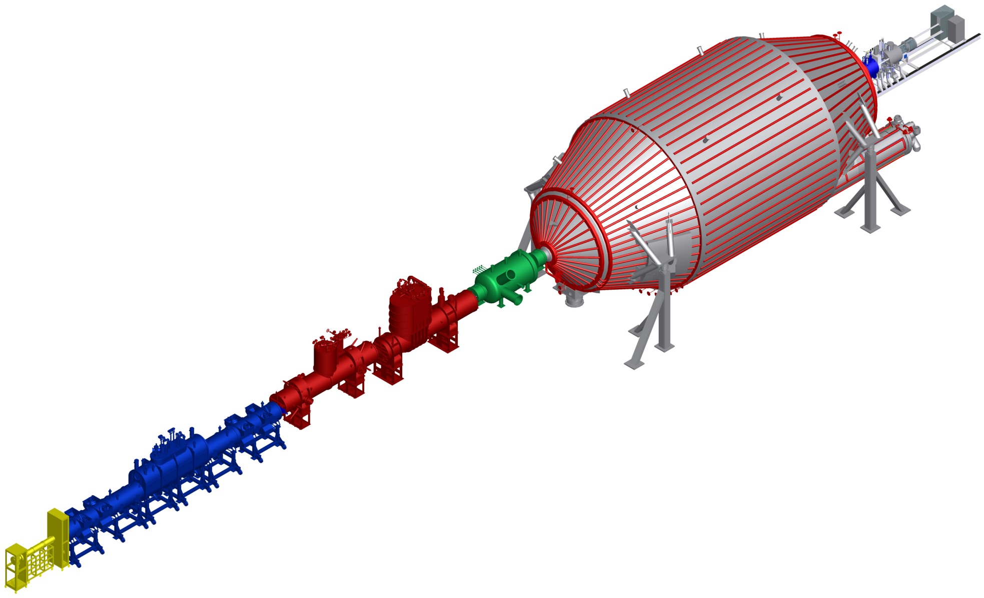

Figure 2.3.: The beam line of the KATRIN experiment with the different stages: Rear section (yellow) and WGTS (blue) on the very left, followed by the transport section (red) consisting of DPS and CPS. Energy analysis in pre- (green) and main spectrometer (grey-red) of the spectrometer section and electron detection at the detector section (grey-blue).

- The source's temperature needs to be very robust (max. $\pm 0.03\,\mathrm{K}$ at $30\,\mathrm{K}$) to guarantee a rate stability of $\pm 0.1\,\%$ for the decay electrons [36].
- The spectrometers further downstream require for ultra high vacuum, for the main spectrometer in the order of 10^{-11} mbar. With the tritium pressure is in the order of 10×10^{-3} mbar and the source's need to be windowless - no electron transparent window is known to stand such pressure differences - the pressure must be reduced to desired values without any physical barrier.
- The tritium isotope contributions of the gas need to be known precisely, for that purpose a laser-raman-system has been developed [37].
- All devices used in contact with tritium have to undergo excessive testing in tritium environment to fault failure safety under the harsh conditions.

2.2.2. Transport and Pumping Section

In the DPS, pressure is actively reduced by seven orders of magnitude with the use of turbo molecular pumps. These as well need to be tested thoroughly to withstand the constant radiation by tritium decays [40]. The tritium gas is then processed to be reused in the tritium cycle. Further downstream, the CPS uses strongly cooled walls to freeze residual gas, always keeping the information carrying electrons away from those by magnetic guidance.

2.2.3. Pre-Spectrometer

The pre-spectrometer was built to reduce the flux to the main spectrometer by 7 orders of magnitude [43]. It works on the MAC-E filter principle from chapter 2.1.1. Being a lot smaller, its energy resolution can of course not compete with the main spectrometer one. Its purpose is to cut off the spectum below energies of 18.4 keV, the electrons above that limit will pass and be further analyzed in the main spectrometer. Here, it is important that

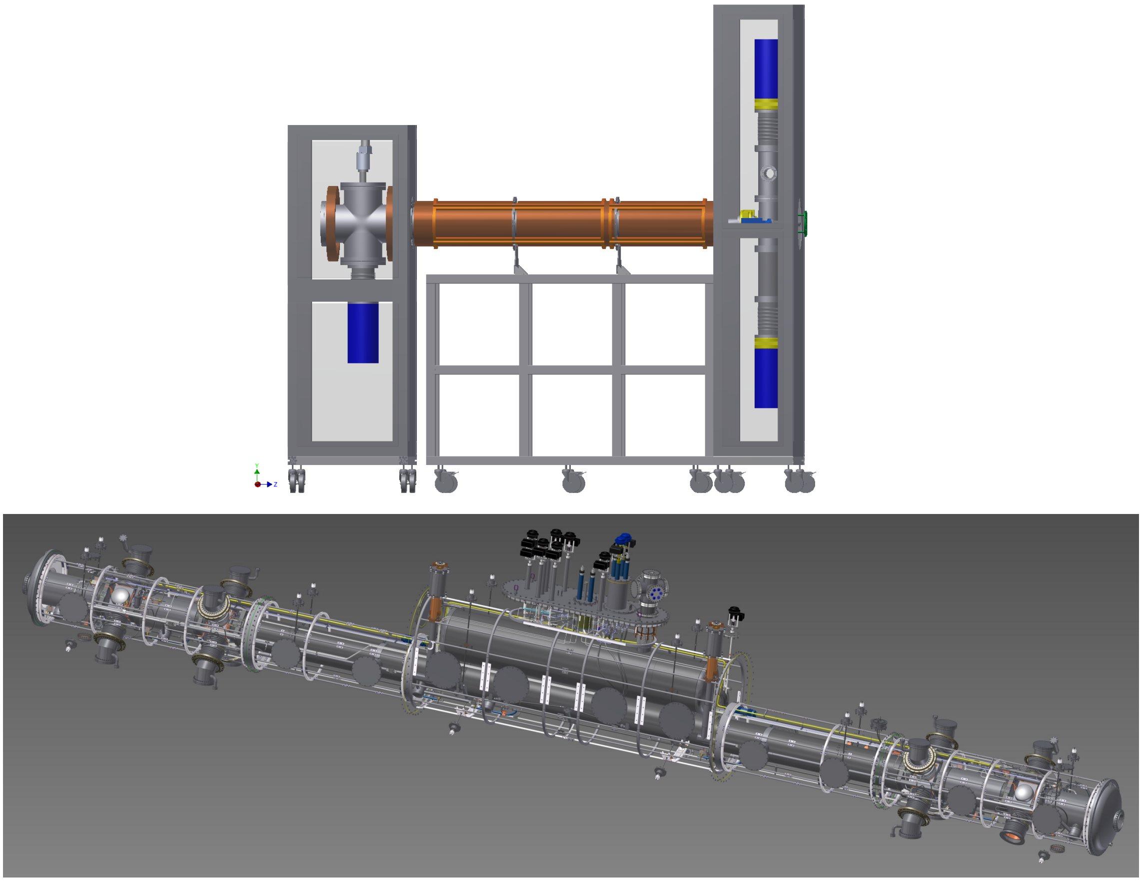

Figure 2.4.: On top, the rear section. In the model, there are two large attachments visible perpendicular to beam direction. The right one is the e-gun for calibration purposes. LEFT ONE!!!!. Also visible are the gray second containment boxes making for redundancy in radiation security. Below a model of the WGTS. The many pumping ports are clearly visible on the left and the right end, in the wider, middle section tritium is injected. Images from [38] and [39]

.

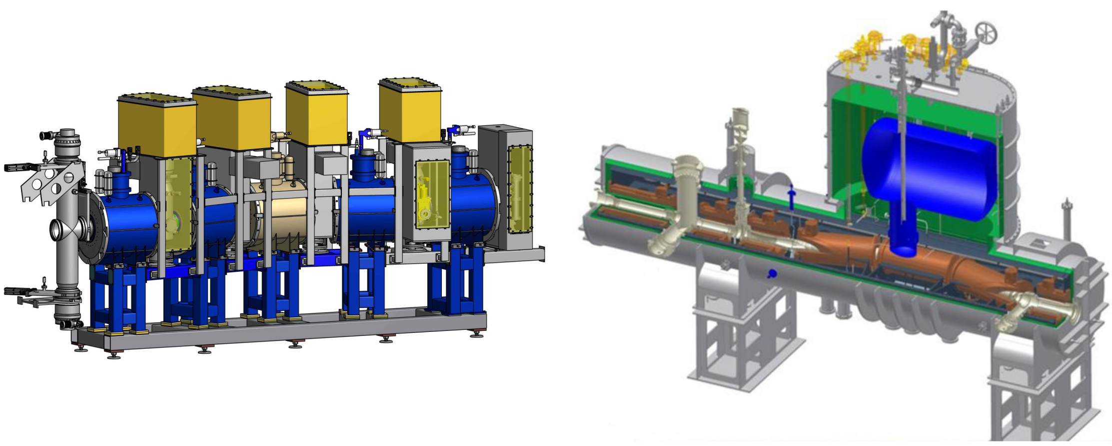

Figure 2.5.: Differential and cryogenic pumping sections, left the DPS with pumping ports all over the structure. All of the ports are isolated against the surroundings (yellow boxes) to protect against potential radiation leaks. On the right the CPS with its coolable wall structure to capture free particle as well as standard pumping ports [41, 42].

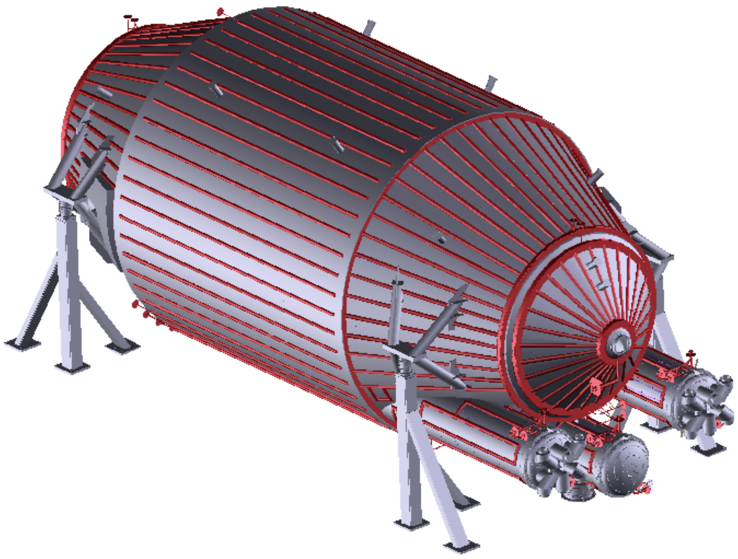

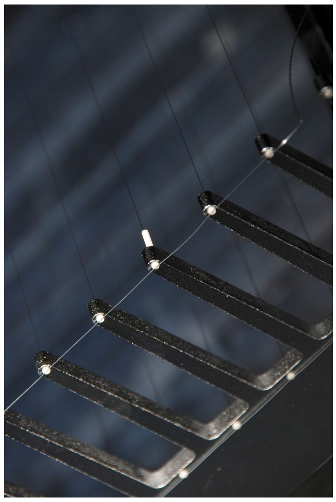

Figure 2.6.: On the left, the main spectrometer of the KATRIN experiment [47]. It is divided into a central, cylindric shape to which two flat cones, disemboguing in the steep cones, are attached. Also visible in this image are the 3 large pump ports on the lower right and the three-legged holding structures. On the right a image of the comb structure of the inner electrodes with both layers of wires visible. The white structures on both top and bottom of the combs are the insulation of the wires [48].

the momentum is restored after analysis which requires for a symmetric setup. To shield against externally induced electrons, the pre-spectrometer has a single layer of wires as a inner electrode. It can be set to negative voltages in comparison to the pre-spectrometer hull which then reflects electrons with energies up to Ue.

2.2.4. Main Spectrometer

The largest component of all is the main spectrometer. With a diameter of 10 m and a length of over 23 m, it incorporates around $1400\,\mathrm{m}^3$ that need to be evacuated to extremely high vacuum of $< 10^{-11}$ mbar. The main spectrometer, as the pre spectrometer, makes use of MAC-E filtering technique from 2.1.1. To do so, it features a uniquely designed electrode and a high voltage system [44]. A precision voltage divider was constructed to read out the high voltage applied to the vessel with the highest precision voltmeters, which operate in the order of 10 V [45]. Additionally, the voltage is fed to the monitor spectrometer from section 2.2.5 to ensure its long term stability.

The vessel is equipped with two layers of electrodes on a comb-like structure. This setup reduces the number of secondary electrons from the spectrometer walls entering the flux tube's volume. Keeping that count low, the rate of those electrons not reflected magnetically due to imperfect symmetries is reduced to the sub-eV level [46]. The layer made from thinner wires further to the inside shields the spectrometer volume from the one further towards the wall as cosmic rays may unleash electrons there as well. The main spectrometer as a whole is set to high voltage varied in the region below the endpoint of 18.6 kV. It constitutes the MAC-E filter from 2.1.1. The wire electrodes float on that voltage with a added more negative value to shield against electron background.

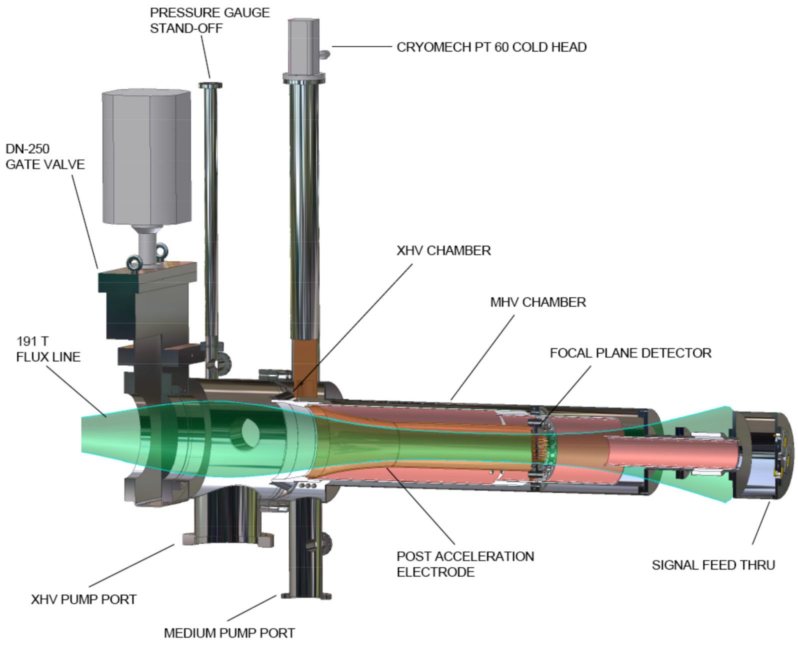

Figure 2.7.: The focal plane detector system including a flux tube (green). One can make out the different grade vacuum sections: extremely high vacuum (XHV) and medium high vacuum (MHV). The post acceleration electrode is visible left of the bronze colored actual detector and its signal feed trough on the very right. Multiple flanges and connectors are shown, not included in this picture are the calibration source holders [49].

2.2.5. Monitor spectrometer

The third MAC-E filter at KATRIN is the slightly modified Mainz spectrometer. It has been transported to Karlsruhe to work as a high voltage monitoring device. Here, electrons from ^{83m} Kr decays are detected and analyzed. The fact that the energy from these decays does not change over time (neglecting changes in the source material) can be used to detect shifts in the voltage of the MAC-E filter. For that purpose, the monitor spectrometer constantly measures transmission functions of The monitor spectrometer features two scintillation modules for muon detection that were used for a first inspection of muon induced background.

2.2.6. Focal Plane Detector System

The detector is located at the very north of the experiment. It is made up of a silicon wafer whose back-side is divided into 148 pixels attached to the readout electronics by pin connectors. The pattern is dartboard-like, multiple pixels with the same distance to the center form rings. Every pixel has the same surface area, making rates more easily comparable - that is for a magnetic flux through the wafer as homogeneous as in this experiment. The detector system is roughly divided into two chambers: one connected to the ultra high vacuum of the main spectrometer and one with a lower grade vacuum on the detectors readout side.

For background reduction, the detector system features both a passive shielding and an active veto system read out by the same data crate as the detector itself. It allows to discriminate against externally induced detector events. Due to the high magnetic fields from detector and pinch magnet, semiconductor readout electronics had to be used instead

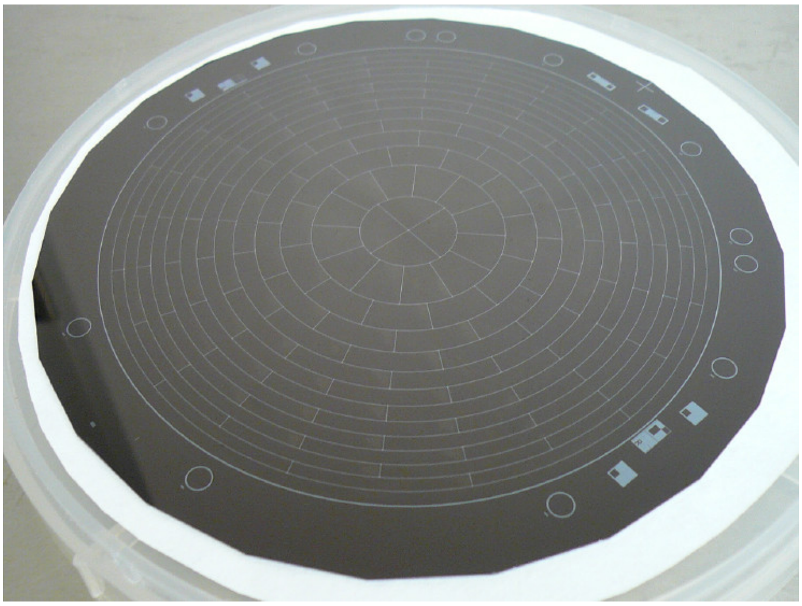

Figure 2.8.: The detector wafer as installed in the FPD system. Note the "dartboard pattern" with the four pixel bullseye in the center. This is the detectors back side to which the electronics are attached, the front is plaid making for high detection efficiencies.

of conventional photomultiplier tubes. As it may be necessary to investigate electrons with energies below the detector threshold, especially for background investigations, a post acceleration electrode has been installed - also visible in 2.7 that can add to the electrons' energies through an electric field of known strength.

2.2.7. Solenoids, LFCS and EMCS system

To achieve magnetic guidance as explained in chapter **??**, a sophisticated system of superconducting solenoids, the low field correction system LFCS and the earth magnetic field compensation system EMCS have been installed [50]. These make sure that the path of flight is kept away from the wall and can be considered adiabatic, that penning traps are avoided as far as possible, that the earth magnetic field is compensated for and, most importantly, that the field drop to the analysis plane is of the order of **(order?)** so the spectrometers resolution will achieve desired values. **ToDo**

2.2.8. Background sources

Different sources contribute to the background of electrons arriving at the detector. Background due to stored electrons is probably the largest source of detector background [51]. Penning traps cause electrons with energies in a certain range to be caught in a potential cup. Discharges of those traps due to scattering processes with either residual gas or due to excessive filling of the trap can cause high-rate events at the detector. This can be both dangerous for the detector itself as it is may inhibit data taking. Stored electrons can be both from external sources as from within the spectrometer. Decays of residual gas or wall absorbed molecules can contribute to the background. One large background source is radon, a neutral particle enabling it to move freely inside the vessel. Radon alpha decays, but shakeoff-, conversion- and auger electrons can be guided to the detector from inside the flux tube [52, 53]. Another large background source are cosmic rays interacting with the vessel hull and producing electrons like that. This background is reduced mainly by two factors, the symmetry of the magnetic field and the wire electrodes shielding the flux

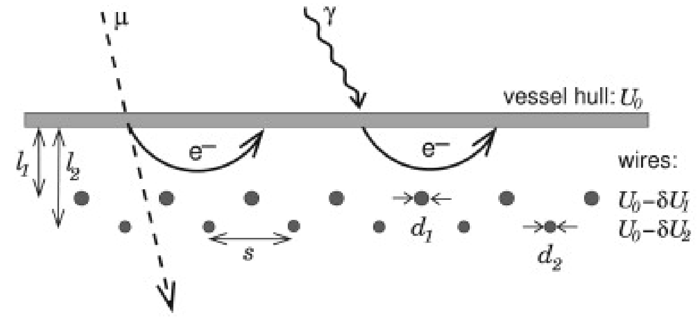

Figure 2.9.: A graph of the wire electrodes installed inside the main spectrometer. Both layers of electrodes with different distances to the spectrometer wall are visible, the inner being smaller in diameter than the outer one.

tube up to a certain threshold energy. To if the fields, both electric and magnetic, were perfectly symmetrical and parallel, only particles generated within the flux tube would be guided towards the detector. But through inhomogeneities and alignment errors, electrons may enter the flux tube even if generated externally, e.g at the spectrometer wall through $E \times B$ drifts. To keep this from happening, the wire electrodes, were installed. They shield the flux tube against electrons with energies up to $E_e = eU_{wire}$ depending on the wire electrodes voltage U_{wire}.

3. Muon detection system

The need for low background rates at the main detector requires for a good knowledge of background sources. Despite magnetic reflection and wire electrodes described in chapter 2.2.8, cosmic ray and particularly cosmic muon induced background may be an issue for the KATRIN experiment. To gather and asess muon related data, a muon detection system has been designed and set up at both the monitor spectrometer and the main spectrometer. Both are built on the same principle. Scintillator panels (sec. 3.3) are permeated by muons causing photon emissions in the material. The photons are detected by photomultipliers (sec. 3.4) and converted to detectable electrical signals. Readout is handled by a data acquisition crate "DAQ" (sec. 3.1) that is controlled via the "ORCA" software on Mac computer (ch. 3.2) While the monitor spectrometer is equipped with only two rather small modules of $A \approx 0.5\,\mathrm{m}^2$, at the larger main spectrometer, 8 modules have been installed at different positions in three groups. Their individual areas are about $2\,\mathrm{m}^2$ and they enable the user to cover different regions of the vessel (see figure **??**). This freedom is enlarged by installing the detection system on three independently movable trolleys. On the trolleys are not only the modules themselves, but also high voltage supplies and all readout electronics for a maximum of flexibility. The modules have been connected to the DAQ, for the connection scheme, see table B.1 in the annex.

All connections from modules to DAQ are made from coaxial cabling of equal length. As the DAQ is located on the east side of the main spectrometer, cable lengths of 30 m are necessary for readout of the west side modules. As timing is important and at that length, the cables introduce delays of $\approx 15\,\mathrm{ns}$ at $50\,\mathrm{ns}$ time bin in the DAQ software, the error for introduced by different lengths woud be too large. Equal lengths ensure comparable timestamps which are assigned only after the analogue signals arrive at the DAQ. High voltage is provided by two supplies, one on the east and one on the west side of the main hall. The settings used for the supplies are shown in table 3.1, figure 3.2 shows the front panel of the east side device. All appliances of the muon detection system are connected to two multiplugs that are both overcurrent protected and feature mains filters. These multiplugs have been modified 3.3 to connect to a ground other than the power outlet's. To ensure a common potential for all of the devices and the surrounding appliances this connection was made to the trough below the main vessel. The high voltage supplies first thought to be used for the main spectrometer modules but not available in large enough quantities were installed at the monitor spectrometer. Furthermore, one more FLT card (section 3.1.1) was set to read out the two monitor spectrometer modules in the manner modules one and two at the main spectrometer are read.

Figure 3.1.: A photograph of the west side trolley of the muon detection system.

V0	I0	I1	V1	Ramp Up	Ramp Down
1.5 kV or 1.6 kV	2000 mA			50 V	100 V

Table 3.1.: High voltage settings as used for the muon modules. Modules XX and XX are set to 1.6 kV.

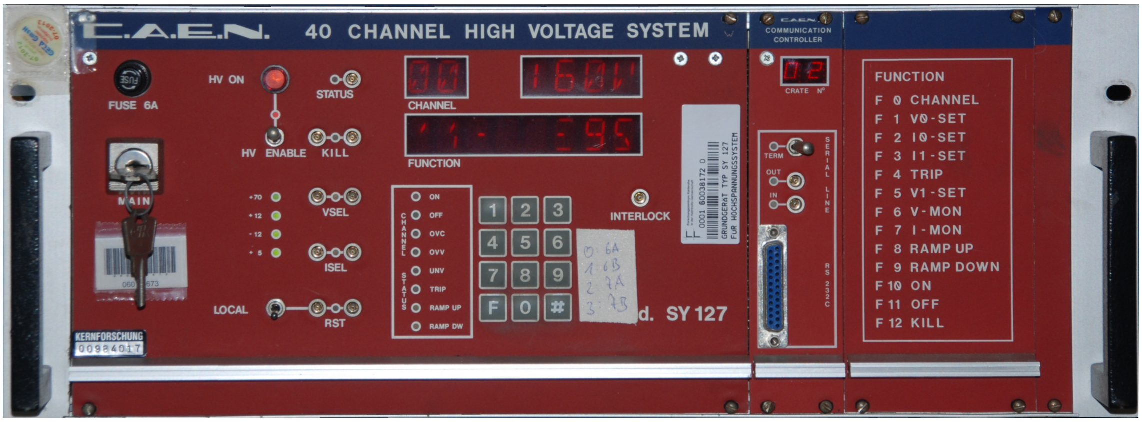

Figure 3.2.: A photograph of one of the two high voltage supplies used to power the muon modules photomultipliers. On the right side, the codes for setup are visible, see table 3.1 for the settings used.

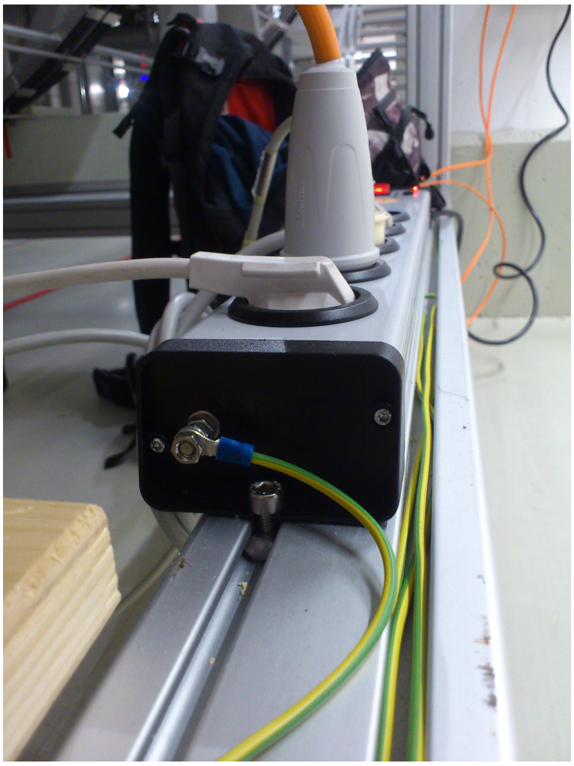

Figure 3.3.: A photograph of one of the two multiplugs. In the foreground, you can see the custom made ground outlet that connects to the same potential the modules are connected to.

3.1. Data aquisition crate

The data acquisition crate (DAQ), is the central part of event recording and by that the interface between hardware muon modules and software based ORCA machine. It was developed for the Pierre-Auger-Observatory in the first place, but was then distributed to many different experiments due to its large flexibility. There are two types of DAQs used in KATRIN: the standard model used at the main spectrometer and the mini DAQ used at the monitor spectrometer. The latter features only 4 FLT plus one SLT slot which is sufficient for the monitor spectrometer, but not for the main detector. Here, the larger model with up to NN cards is used. Both models feature first and second level trigger cards, the former with specific KATRIN firware in version 4 that are described in detail in the following sections 3.1.1 and 3.1.2. The Linux based system runs from an external hard drive connected to the second level trigger card via USB. Here, a screen and keyboard can be connected for network setup, then, access via Unix secure shell is possible. The DAQ can be connected to and controlled by the ORCA software 3.2.

3.1.1. First level trigger cards

The first level trigger cards (FLTs) directly receive the signal output of the photomultiplier tubes via coaxial cabling. To be able to find pulses in the length of the muon modules, they feature a anti-aliasing filter with a sampling frequency of 10×10^{10} Hz. Choosing the right filter settings is crucial for the detection efficiency (see section 5.1). The FLT cards then do first parts of data analysis to reduce data flow to the ORCA machine. In this case, only events with occur simultaneously on both sides of any module are passed on. This reduces the rate from **(look up non veto rate)** to around 250 Hz. The FLT cards are made up of a large main card and a smaller connector card entered at the back side. Every card has 28**(28?)** channels. These are sectioned into three groups if the card is operated in veto

ToDo

ToDo

Figure 3.4.: A image of the data acquisition crate's front panel. From left tor right, the three FLT cards and the SLT card with its Ethernet connection are visible.

Figure 3.5.: FLT back panel card with channel numbering scheme. Readout groups are 0,1,2,3,4,5,6,7 with 14 as the sum channel,

mode. then, every group consist of one sum channel that can be read out in coincidence with any other or multiple other channels from the group (see figure 3.5). In case of the muon modules, 1-fold coincidence is used; one side of each module is the sum channel, the other an arbitrary channel in the respective group. Every event recorded features not only the timing information and the ADC-value, but also the card slot and the channel it was recorded on.

ToDo **(channel numbers)**3.5

3.1.2. Second level trigger cards

Only one second level trigger card is installed on each DAQ. All signals remaining after SLT analysis are stacked here and passed on to the the ORCA machine. Networking runs directly through the SLT card's front panel. The connection is established via the SLT dialogue (see 3.1.2) Other connections, such as USB, a display port, and also the CAT 5 connectors for synchronization to a clock can be attached to the back panel card.

3.2. Orca control

The Object-oriented Real-time Control and Acquisition [54] (ORCA) software is the central software for data acquisition. It is able to control lots of different devices via various kinds

Figure 3.6.: FLT back panel card with channel numbering scheme. Readout groups are 0,1,2,3,4,5,6,7 with 14 as the sum channel,

Figure 3.7.: Data storage obect in ORCA. Marked is the dropdown for setting paths for data, logs and ...

of interfaces with Ethernet connections being the most common. The ORCA software for the muon detection system runs on an iMac Pro. It can be controlled locally as well as via screen share from the KATRIN control room. As the system is located in the restricted area for live high voltage on the vessel, this enables changes on the muon system during high voltage measurements. The different objects used for the muon detection system are explained and shown in the following.

3.2.1. Run control

All data taking is started and stopped through run control. Runs are the basic element of data storage, every time data is recorded, a run is created. Inside every run can be a number of subruns (at least there is one) that will in turn contain data classes such as “KaLi::KLVetoEvent”, the most used event class in case of the muon modules. Runs and subruns are started and stopped via the ”Start Run”, ”Stop Run”, ”Start SubRun” and ”Stop SubRun” buttons. While, from run control, runs can be set to end after a certain timespan and even repeat, subruns can only be used on the go. Using scripting tasks though, all clickable elements are also timeable (clause 3.2.4). On-line and off-line runs can be taken. The latter are not stored or uploaded for analysis but are available for direct reviewing. They are discarded as soon as another run is started. Online runs are handled as decribed in clause 3.2.2.

3.2.2. File handling

All online runs created are first saved to the local disc of the iMac machine as ORCA specific “.orca” files. Sorting in folders for year and month can be applied for quicker access to the data. They are then uploaded to servers of the IPE via cronjobs, a feature of the Linux based MacOS. The cronjob is set to upload only files from ”/home/../data/” **(add dirs)** - the folders in the data storage object should be set to that 3.7. Scripts on the servers convert the files to the .root format. Using the ROOT based KaLi software, data can be accessed and analyzed 4.1 from anywhere in the world with a Internet connection. **ToDo**

3.2.3. Software Gains and Thresholds

All data registered by the DAQ is amplified and cut off at certain, software set values. Theses can be entered for every channel of every card separately. Gains can vary from 0 to 4095 (12 bit), thresholds can be set to any value up to the maximum bin used. Depending on the filter settings, or more precisely with rising shaping length, bin values will be shifted towards higher absolute values 5.1. Scripting of the values is possible and reasonable for large numbers of readout channels such as at the FPD.

3.2.4. Scripting

Scripts are useful for repetitive tasks or such that require short interaction only at certain points in time. One example for scripting is the ramping of LFCS (clause 2.2.7) coils that has been used to check the rate dependence on the LFCS currents (clause 5.3). In that case, the script sends the values to be set to the a server (socalles ZEUS server), which passes them on to **(company name)** boxes which in turn set the desired values at the power supplies. As this was supposed to be a stability measurement, every LFCS setting was kept constant for half an hour after which the script changed the currents. Scripting **ToDo** makes it possible to take these 5 h runs without human interaction making it much more comfortable A.1. Of course, much more sophisticated tasks can be handled through scripts as well

3.2.5. Orca Fit

The Orca Fit function uses external servers to fit data acquired by the DAQ in user defined ways. Besides linear or Gaussian fits, landau fitting (clause 1.7) can be used. The fit software was primarily used to get an impression of the figure of merit of the data. R^2 values are directly displayed which was a first

3.3. Scintillator modules

The central part of the detection system are the eight scintillator modules. They are made of the synthetic material BC-412 which is utilized in applications requiring large area coverage [55]. These, as the DAQ system have previously been used at the Pierre Auger observatory. Every scintillator cuboid is read out by two sets of four photomultiplier tubes (PMT, see clause 3.4). Photons arriving at the short ends of the module are guided to the photomultiplier tubes via non-scintillating material which, away from the scintillation, exhibits similar optical properties. All other sides of the scintillator are covered in reflective foil to push detection efficiency to the maximum. The whole system of scintillator and PMTs is wrapped in thick, black foil to prevent ambient light from being detected as signals. This kind of noise would show especially in the low energy areas, as has been discovered over a broken seal of one of the foils. High voltage, readout and grounding cabling is fed through the foil at two points. Of the eight photomultiplier tubes per scintillator module installed, 4 are read out via one FLT channel. The background of low energy events can be reduced significantly by recording only events occuring on both sides of the module at once. Only coincident signals should be recorded by the DAQ, though, on some occasions, quite a lot of single side signals occur. This seems to be a known bug in the ORCA software that could not be fixed yet. To account for the single side events, in analysis every dataset is first analysed by a search algorithm to filter them out(4.2.2).

3.4. Photomultipliers

Photomultipliers work on two fundamental principles: photoemission and secondary emission. Each Photomultiplier tube is made up of a layer of bialkali metal where photons from scintillation ionize the layers' atoms via photoemission producing electrons with their initial energy less the ionization energy.

$$E_{e^-} = E_{phot} - E_{ion}$$

The electron is then accelerated and guided by the electric field from dynode to dynode (see figure 3.8), cascading to more and more electrons through secondary emission, as each electron's energy rises by $e \cdot U_{acc}$ between each pair of dynodes. This leads to an amplification of the initial electrons energy with the acceleration voltage. Photomultipliers are low noise and very linear amplifiers which makes them feasible for single photon detection.

3.5. Gains, Thresholds and Acceleration Voltages

To achieve the best possible event detection, the photomultipliers' acceleration voltages as well as the software gains and thresholds in Orca had to be adjusted. The focus here was

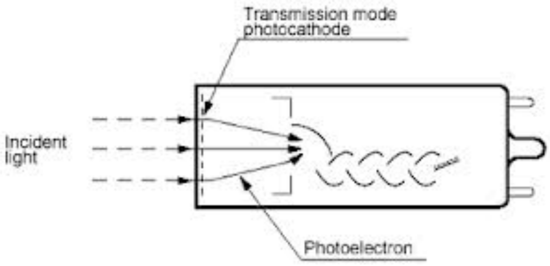

Figure 3.8.: Schematic view of a photomultiplier tube with incident photons and photoelectrons emerging. Note the nested dynode structure for cascading purposes.

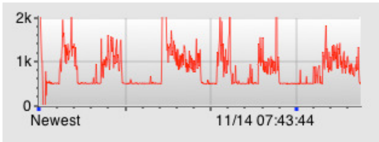

Figure 3.9.: Rate progression over the course of hours. Noticeable raise in the cumulative rate of all panels in certain intervals

to obtain landau peaks with equal heigt and width, as the rates throughout the modules can be considered equal over large time intervals compared to the inverse rate. During some preliminary measurements it became obvious that the panels' rates were peaking over certain, short time intervals at some arbitrary frequency. If the landau distributions (section 1.7) were not identifiable due to prevalent electronic noise, the measurement was rendered useless. That way, setting gains, thresholds and PMT voltages correctly was very difficult as one had to get lucky to measure in a noise free period. It seemed there was some kind of electronic pileup. As this did not appear at all the modules it was not noticed until later into the commissioning process.

As a countermeasure, in cooperation with Sascha Wuestling, potential equalization by connecting the modules to the trough below the main spectrometer has been established. This showed to prevent the peaking so the issue seems to be resolved. Now, gains, thresholds and acceleration voltages could be set **??**.

At first, the acceleration voltages were kept low to limit the signal peaks' heights to around 2 V. Carefully setting the mentioned parameters, one achieved the well aligned distributions from figure 3.11. A problem remaining at the time though was that the electronic noise set in pretty close to the peak position, only slightly shifted to lower energies. This made it not only very difficult to find suitable settings, but also meant that thresholds hat to be set close to the peak bin loosing low energy events in the process (see figure 3.11). This showed in rates of around 150 Hz that did not compare too well to literature values. The high energy region though was well fittable with landau distributions.

Later in the commissioning process, it got clear from the handbooks that the photomultiplier tubes had to be operated at acceleration voltages of 1.5 kV and above. This was found as the detection efficiencies 5.5 for the modules were not as high as expected, assuming that the acceleration voltages set lower than denoted in the user manual leads to loss of data in the low energy range. Consequently, the acceleration voltages were raised to 1.5 kV except for two channels, those of modules 2B and 6A, that were even ramped to 1.6 kV on account of showing lower overall rates. Most of the tubes were limited to this minimal voltage to keep the signals' height as small as possible protecting the DAQ from taking damage. Following this procedure, the tubes seemed much more stable and rates more comparable, as all the gains and thresholds could now be set to the same values of 0 **(enter thresh** **ToDo**

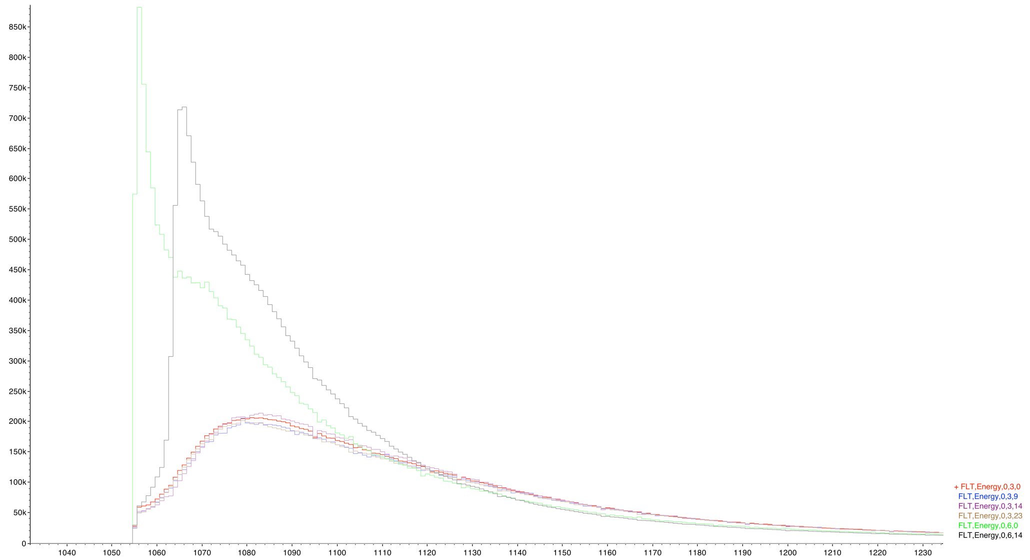

Figure 3.10.: Energy histogram of six channels, i.e. modules 6 through 8.Displayed are counts over ADC-Value. Two channels show a lot of noise at th low energy end of the histogram while four are developing nicely looking Landau Peaks.

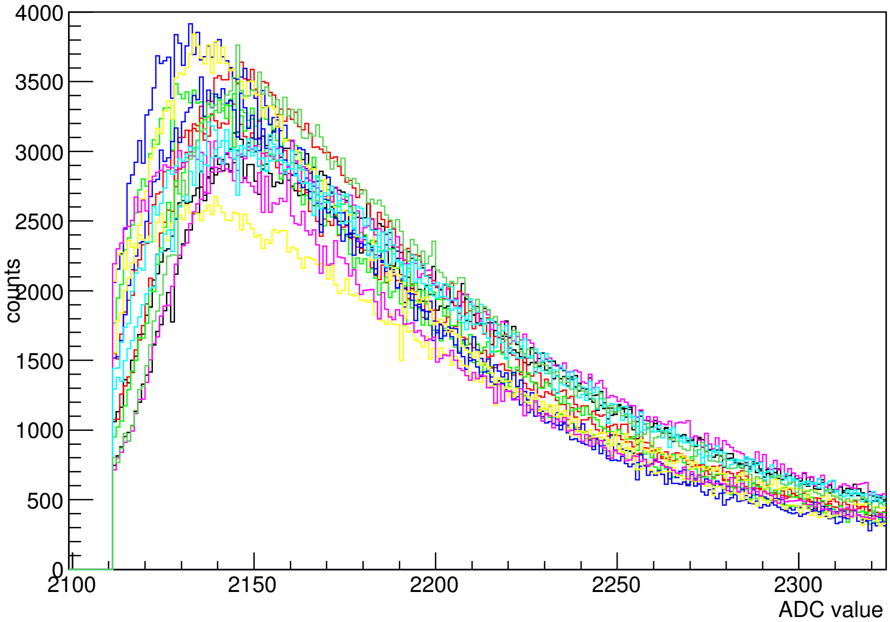

Figure 3.11.: The landau peak at acceleration voltages around 1200 V. All channels show similar width and height. Note that the thresholds had to be set pretty close to the peak position as noise was a huge issue under the conditions.

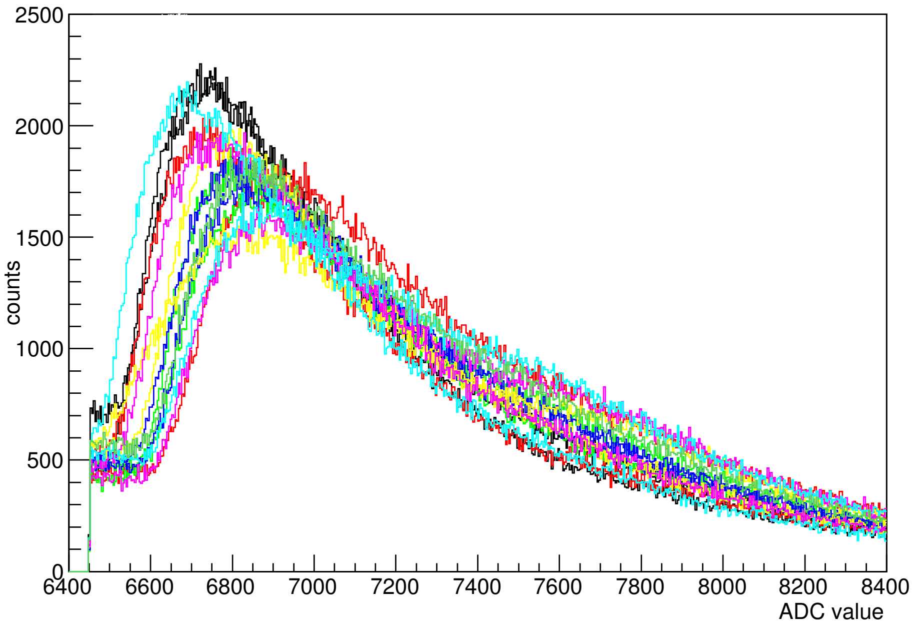

Figure 3.12.: Landau peaks after raising acceleration voltages to 1.5 kV or else 1.6 kV. Note that this pattern was achieved solely by raising two module's side's acceleration voltages to 1.6 kV leaving gains and thresholds at the same low level for all channels.

value) and respectively, while still showing well aligned peak positions 3.12. This is a huge advance to before when gains varied by factors almost up to four as it reduces potential non-linearities in amplification. Also, gains are left at lower values to begin with, leaving a larger part of the all in all amplification to the photomultiplier tubes known for their linear behavior and relatively low noise.

4. Analysis software

To analyze the data recorded by DAQ and ORCA software, completely new data structures fit to the needs of muon detection and coincidence analysis were created. Methods were implemented to further investigate data stored inside those structures. A cmake file has been created making it possible to install the programs on any machine used for analysis. That way, programs can be modified for custom analysis that shall include muon data making it very modular. All the sources including the main programs are available on the svn repository **(move program(s) to svn repository)**. **ToDo**

4.1. Data structure

All data from the IPE-servers arrives converted from ORCA-specific formatting to .root files compatible with CERN's analysis software ROOT (see section 3.2.2). Hence, ROOT Methods are used to extract data from these structures, while most of these methods are implemented as part of the KaLi package in the Kasper software which constitutes for a complete and closed data transfer protocol. The Kasper software is a simulation and analysis software tool developed and steadily extended by the KATRIN collaboration. Through those structures, data specified by the user will be cached locally and can be analyzed afterwards.// For analysis with the classes described here, all data is transfered from the cached files to runtime storage. Here, the newly written class **event** with the following members comes into play.

event private class members

- fADCValue
- fTimeSec
- fTimeSubSec
- fPanel
- fSide

For each member, corresponding set- and get-methods have been implemented making them accessible to the programmer. Furthermore, the operators ”<”, ”<=”, ”>”, ”>=”,

"==", and "-" have been overloaded to compare the timestamps of the event class. This was useful and since ADCValues are merely used for plausibility checking of the data but not for quantitative analysis, there was no need to compare energy values. Doing so, events and the classes derived can easily be compared and searching becomes cleaner and clearer. Derived from the base event class are two more storage classes:
panelEvent storing a second ADCValue

coincidentEvent additional member

- fADCValue2

and the common timestamp of events activating both panel sides and **coincidentEvent** storing ADCValues of simultaneous events in multiple modules and the number of modules involved:

coincidentEvent additional members

- std::vector fADCValues
- fnPanels

If a run file is downloaded, the constructor of the class **run** (section 4.3) stores the data of the .root files in vectors of events. Recorded events should already be filtered - only simultaneously occurring events on the two sides of the same module should be recorded. This is set in the FLT dialogue of the ORCA software (section 3.1.1). As, out of unknown reasons, single sided events are recorded as well, a software workaround is needed. All events of one side of each module are scanned to find whether a corresponding event with the same time stamp exists on the other side . If so, a coincidentEvent is created and pushed back into the run's vector of coincident events corresponding to the module it occurred in. With the setPanels() function, the modules for analysis can be chosen. This can be done sequentially for multiple sets of modules without newly reading the run's data, as all the primary data is stored inside the event and coincident event vectors.

run class members

- std::vector events
- std::vector detectorEvents
- std::vector eventsByPanels
- std::vector coincidentEvents
- std::vector selectedPanels

4.2. Search Algorithms

To analyze data, at various points searches for events with a particular time stamp have to be performed. This was simplified by the time-sorted recording of events. A first

Figure 4.1.: An illustration of the search algorithm utilizing the average rate of the run analyzed. Based on that, a guess is made (marked in). If that guess is wrong, the algorithm increments the guess in units of the rates standard deviation.

Figure 4.2.: All modules are stepped through, the one with the earliest time stamp is incremented. Then, all times are compared to each other.

implementation to search for coincident events was done on the base of average frequency and its standard deviation. This algorithm proved as fast and stable, though well applicable only for two sets of timed events. That is why an advanced incremental method has been created. The number of modules is now limited only by the physically available memory and the speed is even higher.

4.2.1. Frequency Search

As this algorithm was built to run on only two sets of data, it simply walks through one set incrementally and looks for corresponding data in the other. Latter is not done in a "dumb" way by incrementing through the second set as well, but by calculating the average frequency of events inside the set and performing an intelligent guess on that basis. If the guessed event shows a different time stamp, the algorithm will keep going forward or backward in time in steps of the frequency's standard deviation until the time stamp searched for is in between two steps. Lastly, simple incrementation is used to find out whether an event at the desired point in time exists or not.

4.2.2. Incremental Search

While the frequency search increments solely one dataset, the incremental search steps through all the event tress, incrementing the one with the smallest time stamp. It then compares all events to each other, writes out the coincident ones, if any, and goes on incrementing the next smallest stamp. This assures the finding of all coincident events while keeping the speed very high.

4.3. Member Functions of the class run

Constructor run()

Whenever a new instance of "run" is created, the constructor is called. Arguments to be passed are a KaLi::KLRunIdentifier, basically a string distinctively naming the run to be analyzed, such as "myo00000001", a instance of KaLi::KLDataManger, a class handling the download of the Files form IPE-servers and a toggle variable telling the constructor which data to read via the member function getRun() and what member functions to call afterwards:

Destructor run()

The destructor deletes all the contents of the vectors of events and inherited classes and clears them afterwards before deleting the member RUN which in fact frees all the memory reserved by the KaLi classes.

Toggle Choices

- **0:** Data is downloaded and both muon data and detector data are stored
- **1:** Data is downloaded and only detector data is stored
- **2:** Data is downloaded and only muon data is stored
- **3:** Data is read from local file system, only muon data is stored
- **10:** Monitor spectromer data is read. Different card and channel configurations are used.

getRun()

The getRun function sets the member KaLi::KLRun through the KaLi::KLDataManager and then returns KaLi::KLRunEvents. This means that here, the actual readout of data from the servers is happening. After the getRun function was called, the data is stored in the ram for analysis. The returned KaLi::KLRunEvents includes all recorded events meaning also both the relevant KaLi::KLEnergyEvents and KaLi::KLVetoEvents. The former is used to store events at the detector, it contains timing information and ADC value of the event as well as where it was recorded. The latter is used at the muon modules. Additionally to the data stored in a KaLi::KLEnergyEvent, this class stores information on one or more events in coincidence with the first. In our case this is always the other side of the module. The getRun() function is used in the constructor for example to read the run's data.

getLocalRun()

It is not always possible to read data from the file servers, example given are files too big leading to timeouts at least in older KaLi versions. That is why the getLocalRun() function was introduced reading data from the local filesystem via the KaLi::KLRunIdentifier. The path to the files can be adapted in the source code. Additionally a environment variable called "MUONLOCALPATH" can be set to change directories without recompiling. The standard setting is "/kalinka/storage/TBcube/rovedo/asymField/".

detectCoincidences()

The detectCoincidences function calls the member function channelCoincidences() and panelCoincidences(nPanels) sequentially. It then returns the output of panelCoincidences(nPanels) where nPanels defines, how many modules have to show coincidences for the counter to increment the number of panel coincidences. At the same time, this empties and refills the vectors of panelEvents and coincidentEvents according to the latest choice of selectedPanels. That makes it easy to call the function multiple times, especially since the analysis is fast compared to the downloading time.

channelCoincidences()

This always clears the vector eventsByPanels before filling it according to the current selectedPanels settings. To do so, it loops over all entries of selectedPanels, calling loopOverSides() of the current module.

loopOverSides()

LoopOverSides analyzes one of the modules for coincident events between the two sides. The function runs through all the events of one panel side using the operators ”<” and ”==” overloaded for the class run to compare event times. For the search itself, the ”A” side’s index is incremented step by step while the ”B” side’s index is pushed up as long as its event time is smaller than A’s. Every time that condition changes, it checks whether the events occured at the same time - pushing back a coincidentEvent with both the events’ ADCValues and their time stamps into the vector for the corresponding module if so - and then going on incrementing module A’s index.

panelCoincidences()

As mentioned in chapter 4’s introduction, the first algorithm to search for coincidences between different panels was based on the average event frequency and its standard deviation, soon beeing replaced by a simpler, more efficient incremental algorithm: This features a storage for the smallest timestamp in a group of events. **(change code to overl.ops)** This is set to the smallest timestamp of the first event of all the modules analysed. Now, all the events are compared to the smallest one. This has the advantage, that one does not need to cross check every event with every other one but can simply compare every event to the smallest in a linear way. If simultaneous events are found, they are pushed back into the coincidentEvents vector together with the timestamp and their ADC values, nPanels is risen by one. Subsequently, the index of the smallest event storage is incremented and the new smallest event in the changed pool is searched for via the member function findSmallest(). This is repeated until all the event storages have reached their last entry. The return value is the number of events fulfilling the requirement passed through nPanels to panelCoincidences: if it is zero, every coincident event with two or more modules involved is counted, for every other number, only the number of event with exactly this number of modules is counted. **ToDo**

findSmallest()

This function returns the smallest panelEvent’s time stamp through references as both a second and a subsecond count have to be returned. The findSmallest function accepts panelEvent-indices of the different modules and returns the one with the smallest time stamp.

TOFHist()

Setting the modules to be analysed to one and two, this function was designed to analyze monitor spectrometer data. This also reflects in the fact, that both muon data and detector data are expected to be stored within the same mosxxxxxxxx run file. The function then runs channelCoincidences() and panelCoincidences() before shifting through all the muon events searching for following detector events in a certain time interval. The time interval is chosen on function call. Time differences are stored in a vector of events passed by reference to the function.

TOFMuonDet()

In contrary to the TOFHist function, this one reads muon and detector data from different files as it is designed for the needs of main spectrometer analysis. Here, two DAQs record muon and electron detections to myoxxxxxxxx and fpdxxxxxxxx files respectively. That is why the function reads a muon run and requires a guess as to where corresponding detector data is located. It then searches the given detector and moves on as long as no change of sign in the time difference occurs. To do so, it might also read new detector runs. If the time difference sign changes, the function searches for a detector event within the time window passed on call and pushes it back into a vector of events of time difference. A histogram can now be filled with the data acquired to inspect it for cumulation of time difference events at particular times.

determineEfficiency

Efficiencies of modules can be determined through three of them located coextensively in front of each other. Then, all events recognised in both the uppermost and the lowest module have to - leaving geometrical inaccuracies unaccounted for - pass the middle module as well. By comparing the counts one can determine an efficiency for the middle module. Usually, the modules used are 6,7 and 8 though for testing purposes also modules 3, 4 and 5 have been analyzed.

$$\%_{eff} = \frac{\wedge_{68}}{\wedge_{678}} \tag{4.1}$$

To do so, the function reads a muon run, selects three modules and runs the channelCoincidences() and panelCoincidences(3) functions. The returned number of events detected in all three of the modules is stored. Then, only the outer modules are selected and panelCoincidences(2) is called. The ratio of the two panelCoincidences calls is the return value of the function.

getSize()

The getSize() function returns the size of one of the vectors storing events or one of the inherited classes depending on the passed integer ”what”:

- **default/1:** Size of events returned
- **2:** Size of eventsByPanels returned
- **3:** Size of coincidentEvents returned
- **4:** Size of detectorEvents returned

If one, two or three are chosen, the module number (and side in case of one, 0 being A and 1 being B) can be passed to choose the size of which vector to return. By default, module module 1 (side A) is returned. **(default nonsense, reimplement)**

ToDo

readVetoEventData(), readDetectorData() and readMOSDetectorData()

Depending on the toggle choice in the constructor, either one of the three or two of the functions are called. The readDetectorData() function reads all recorded KaLi::KLEnergyEvents which are only the FPD and the monitor spectrometer record those. The readVetoEventData() function reads all the KaLi::KLVetoEvents from the cards in slots three, six and nine. This can never interfere with veto data recorded at the FPD for the active veto for the detector signals, as cards 15 and 16 are used here. For analysis of monitor spectrometer data, a function readMOSDetectorData() has been implemented reading all energy events of card one independent of channel, while of course single channels can easily be excluded. The pulser usually active at the monitor spectrometer creating KaLi::KLEnergyEvents at constant frequency is standardly excluded from analysis. Inside the readVetoEventData function, an additional readout from card 4 has been integrated for monitor spectrometer veto signals. This slot is unused at the main spectrometer meaning the events can be easily distinguished in analysis. All the member functions reading data require the passage of an instance of the KaLi::KLRunEvents, usually the member of the same class set in the getRun() function.4.3

5. Comissioning measurements and analysis

While the moun detection system was still under construction at the beginning of my thesis-work, first measurements were taken at the time with some modules under preliminary conditions to look into the behaviour of these modules. Step by step, the system was completed and is now up and running. In the building phase, several measurements and test have been conducted to ensure the capabilities of the system meet the requirements for the KATRIN experiment. Starting with the setup of acceleration voltages, gains and thresholds, Using data obtained by the muon modules and the detector as well as other subsystems' data, the muon induced background rates and both spatial and energy distribution can be obtained. Before actual measurements were done, the modules had to be set up and calibrated, meaning high voltage and signal cabling needed to be installed and high voltage power supplies had to be acquired.

5.1. Finding the best filter settings

As the PMT tubes are directly, without any preamplifiers, connected to the DAQ, the signal lengths arriving at the latter are in the order of 20 ns. This poses a problem for filters as the sampling rates need to be high and anti-aliasing is inevitable. To find the best settings, a function generator has been set up to create events at known frequency and peak heigth. The pulser's signal form **(what form)** was chosen as closely to the actual shape as possible, which is the "pin diode" form. **ToDo**

In order to evaluate filter's figure of merit, the width of the resulting energy histogram, which should, assuming perfect pulser signals and perfect filters, be mono-energetic, was analyzed for each filter setting. For analysis, the width of the contributing ADC bins and their absolute position as well as the pulse height and the filter settings were noted.

On average, the boxcar filter at shaping lengths of 150 ns shows the most promising results, i.e. the sharpest energy resolutions for any signal height. This concurs with the settings chosen for the active fpd veto; here slightly longer (around 30 ns) but comparable signals enter the DAQ's FLT cards showing best results at the same filter settings[56]. That is why, for any measurements after **(run & date)**, the new filter settings were used, bringing up the need for new threshold and gain adaptions 3.5. **ToDo**

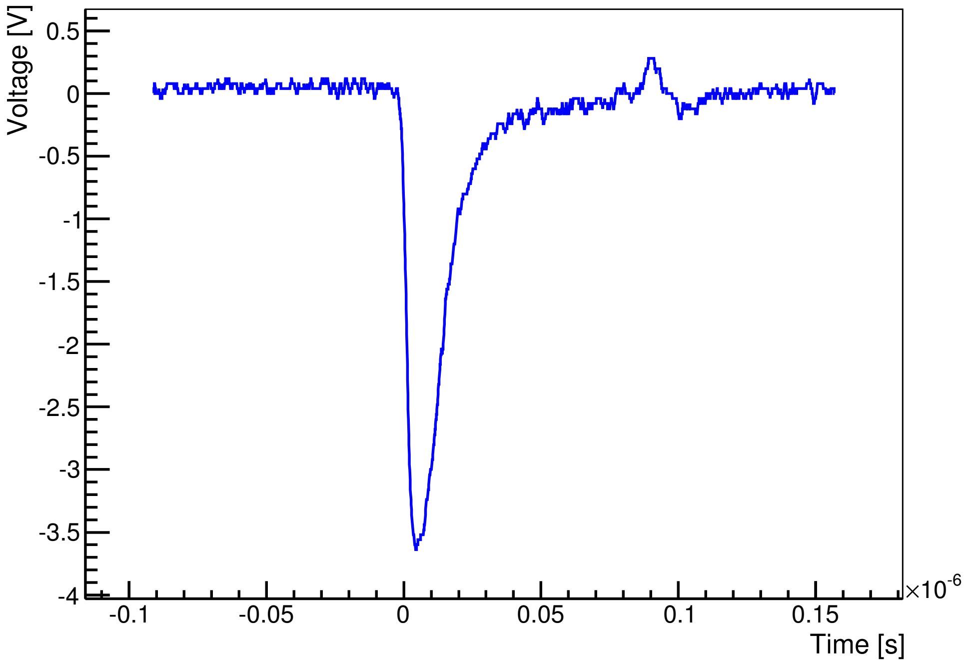

Figure 5.1.: A signal as recorded by the muon modules with a oscilloscope

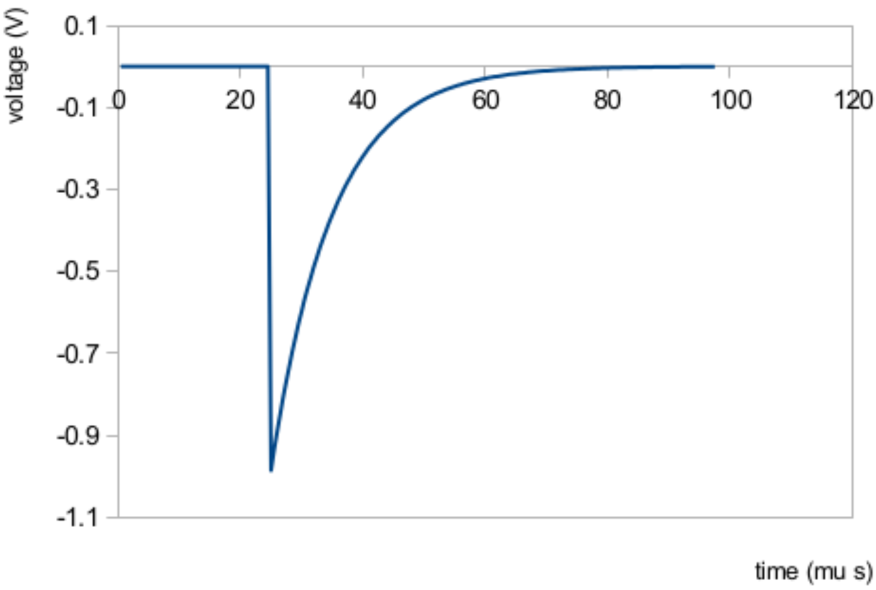

Figure 5.2.: The arbitrary pulse form used for testing purposes. Different voltages were tested. Here, the peak height of 1 V is shown.

Voltage[V]	Boxcar length [ns]	width	position	threshold
1	50	33	2160	2100
	100	37	2140	4200
	150	13	2140	6300
	200	21	2141	8400
2	40	25	2160	2100
	100	78	2140	4200
	150	78	2140	6300
	200	77	2141	8400
3	59	25	2160	2100
	100	113	2140	4200
	150	110	2140	6300
	200	112	2141	8400
4	80	25	2160	2100
	100	145	2140	4200
	150	147	2140	6300
	200	149	2141	8400
5	94	25	2160	2100
	100	180	2140	4200
	150	185	2140	6300
	200	41	2141	8400

Table 5.1.: Energy resolution at different filter settings. A function generator was used to simulate pulses from the muon modules.

5.2. Moun module's rates

A simple first check into the data was possible simply by comparing the rates measured to literature values. Here, a flux of around 1 per min and cm^2 through an area parallel to the ground is stated. Measured rates are in the order of 250 Hz. The muon modules' area is

$$315\,\mathrm{cm} \cdot 65\,\mathrm{cm} = 2.05\,\mathrm{m}^2 \tag{5.1}$$

considering the 45° tilt of the modules towards the horizontal, this area reduces to an effective area of

$$A_{\mathrm{eff}} = \sin(45°)A_{\mathrm{real}} = 1.45\,\mathrm{m}^2 \tag{5.2}$$

Further taking into account detection efficiencies η discussed in 5.5, we receive an estimation of effective rate of

$$\Phi_{est} = \eta \frac{1}{\mathrm{cm}^2 60\,\mathrm{s}} A_{\mathrm{eff}} = 225\,\mathrm{Hz} \tag{5.3}$$

This compares well to measured rates of **(calculate actual rates)** 250 Hz. **ToDo**

5.3. Modules in high magnetic fields

Photomultiplier tubes do not work in magnetic fields. As mentioned before, they use electrons cascading in electric fields to generate amplified signals. Additional magnetic fields can keep the electrons from reaching the dynodes stopping the cascade thus keeping single events from being registered. For there is the need of moving the muon modules as close to the spectrometer tank as possible to register mostly muons that indeed went through the vessel, they are aligned closely to the air coil system. As rate decreases strongly under these conditions **(are there runs showing that? ask nancy)**, a solution needed to be found. As a simple, yet efficient passive counter measurement, a layer of mu-metal **ToDo**

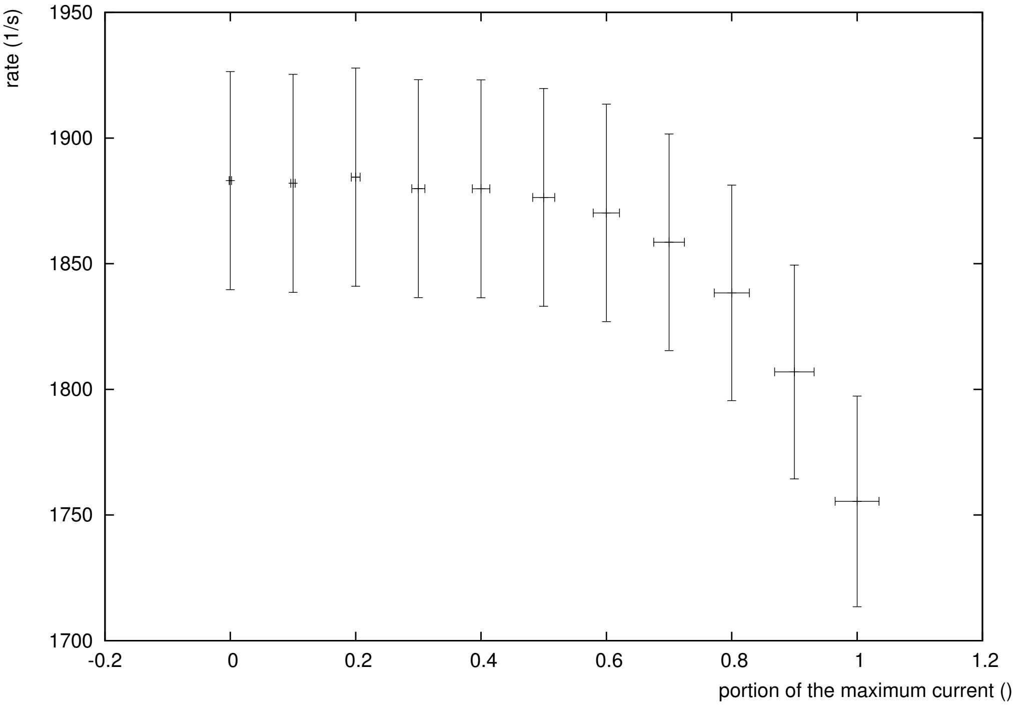

Figure 5.3.: Summed rate of all modules over air coil currents. Currents are displayed as parts of the maximum current. A clear decrease in rate is recognizable from 60 % of the maximum current upwards.

was wrapped around the modules. Mu-metal is a magnetically highly permeable material (μ_r in the order of 10×10^5 [57]) that guides the magnetic field lines inside itself. In doing so, the remaining flux inside a mu-metal surrounded volume, and with it the field strengths, drastically reduces. For a sphere with inner radius a and outer radius b, the shielding factor F is given by

$$F/B_0 = 9/\left(2\mu\left[1-(a/b)^3\right]\right) \tag{5.4}$$

where B_0 is the magnetic field strength without the and μ the magnetic permeability of the material [58]. Though the shape used is not spherical, already with layers if 1 mm thickness, a relative decrease in fields of a factor of two should occur.
To test the improvement the mu metal coverage produces, measurements with rising aircoil currents have been performed. Steps in the size of tenths of the maximum current were used to record rates over half an hour at each value. For most of the LFCS coils this were 100 A, in some cases (LFCS 1,2 and 14) only 70 A. During the first run, due to a slow control problem, the current was not raised between two steps. Although displaying the expected behavior - rates dropped much less than before - the measurement was repeated with the correct currents at every steppoint. Measurements show that the rate still drops at currents close to the maximum, though only to around 90 % of initial values, (figure 5.3). As, under normal measurement conditions, the LFCS currents are mostly around half the maximum value or less, the problem was solved. In that region, the reduction in rate is within the errors' order.

5.4. Module Stability

If consistent factual statements on muon induced background are to be made, the modules need to work stable over the course of days, as rates are supposed to be comparable. For this reason, over the Christmas time 2012, a two-weekly measurement of half hourly runs was taken, see table 5.2 for air coil settings used. Runs myo00000051 to myo00000675 contain

Coil #	1	2	3	4	5	6	7	EMCS h
Current [A]	10	10	14	25	42	39	54	50
Coil #	8	9	10	11	12	13	14	EMCS v
Current [A]	54	21	36	30	21	20	56	15

Table 5.2.: Runtime settings for air coils as proposed and for the commissioning measurements. These were kept static over the two weeks end 2012/beginning 2013

the data of this measurement. The time slot was chosen because of the lowly frequented spectrometer hall. The thought was to minimize external impacts on the measurement. During data taking, the LFCS coils were active. They generated magnetic fields in which the PMT tubes had to work throughout the measurement. The LFCS settings are found in 5.2. For analysis, a simple program to count events in variable time bins was written, creating a count histogram for all the runs in the measurement period. The result can be seen in figure 5.5. A fluctuation of 5 % of the average value is observable. This is describable by fluctuations in atmospheric density, i.e. pressure Δp and temperature ΔT and in muon production height Δh. The change in relative intensity is decribed by the following equation.

$$\frac{\Delta I}{I} = -(\alpha_\mu \Delta p + \beta \Delta h - \gamma \Delta T) \tag{5.5}$$

where α is a barometric coefficient in $0.215\,\%\,\mathrm{mmHg}^{-1}$, β a decay coefficient in $5\,\%/10\times10^3\,\mathrm{m}$ and γ a temperature coefficient in $0.1\,\%\,\mathrm{K}^{-1}$ [59]. Looking at weather data from [60] available on a daily basis, the fluctuations resulting from equation 5.5 do not fit the data very well. Both highest and lowest value for pressure and temperature were used to calculate daily maxima and minima in intensity. The relative change was projected onto the average rate in figure 5.5. Although the order of magnitude does not differ vastly, even the rate development does not always compare to the ones visible in the data of the stability measurements. Several reasons may contribute to this. It has to be kept in mind that the weather data was obtained from a weather station in Rheinstetten, about 20 km south of KIT campus north. Furthermore, the station only records data from the lowest atmospheric layer while muons are generated mostly in the upper layers of the atmosphere. Additionally, and this is probably the largest factor here, the muon production height was not included in the analysis as no data was available for this. As all of the fluctuations are in a window of around ± 5 %, the modules are stable enough for the purposes needed.

5.5. Module Efficiency

The runs used for stability measurements, as well as any other run including three modules coaligned in front of each other, can be used to check the middle module for efficiency. For tests on other modules, the geometry would need to be changed so that the one to be checked is in between at least two other modules. For analysis, the function determineEfficiency() 4.3 has been written. The principle is the following: considering the small change in momentum direction high energy muons achieve through interaction with matter, one can assume straight-lined paths. From that follows, that if two parallel planes, that can be used to describe the scintillating volumes, are hit, any other, also parallel plane, in between those two will be hit as well. Keeping this in mind, one can analyse data for events registered in both modules 6 and 8 and cross check whether a event has been detected in module 7 as well. The quota of events in all three modules compared to those detected in 6 and 8

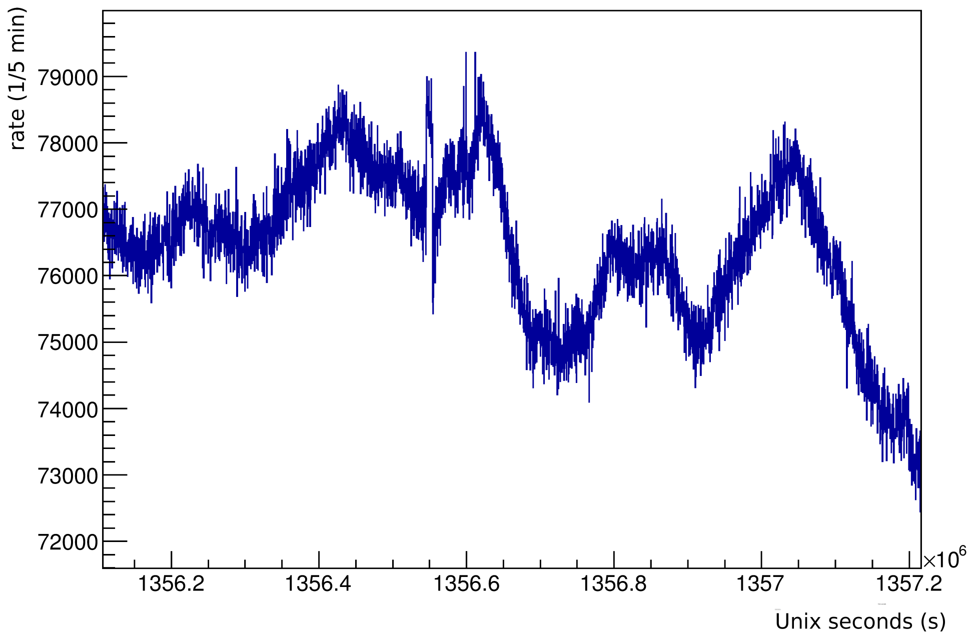

Figure 5.4.: Counts per five minutes over the course of about two weeks (21-12-2012 to 03-01-2013). The rate deviates 5 % from the average.

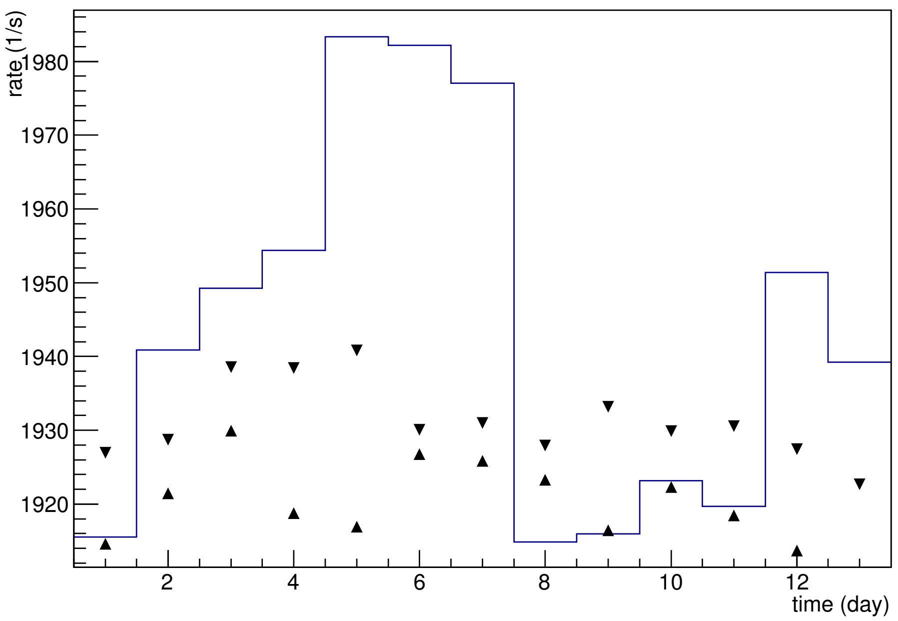

Figure 5.5.: Atmospheric density as a function of time over the course of two weeks the muon measurements took place. Note the

- including the triple events - shows the efficiency of module 7. It shows that during the measurement period end of 2012, the efficiencies were at **(rerun)** $(92.8 \pm 3.8)\,\%$ which is less than one would expect at a scintillator thickness of 5 cm. For that reason, the filter settings were checked and changed to the boxcar filter with a gap of 150 ns from the before used **(exact name)** filter. However, the expected efficiency increase was not observable. The average efficiencies were now at $(93.4 \pm 3.6)\,\%$, well within the margin of error of the other. To examine the problem further modules 3, 4 and 5, that are located next to each other, were used for efficiency measurements as well considering they are stacked in an upright way. Using the program on those three modules resulted in even lower efficiencies of $(50.0 \pm 3.2)\,\%$. This raises the question whether this is not an effect of signal filtering, but a previously not considered physics effect. One thing coming to mind is deviation of the muon track from linear forms. This feature would comply with the seemingly lower efficiency at the upright stacked modules, where, at equal bending radii, the ratio of muons traveling around the middle module is higher due to the lower total area in stacking direction. This thesis should be tested. This can be done both by simulating the cosmic muons including magnetic fields and empirically by varying the distance between the single modules. The latter is difficult not only because the modules are heavy and not made for lifting (no designated carrying structures), but also because movement always means potential danger to the photomultiplier tubes and their connection to the scintillators. Furthermore, if all coils and solenoids were to be turned off simultaneously at some point, one could collect data then and see how efficiencies change during that (there have been runs taken when that was still the case, but only few modules were working properly at that point). If the dependence on module distance turns out to be true, but the efficiencies are still below expected values at the lowest possible distances, a possible improvement would be to use pre-amplifiers before signals arrive at the DAQ. These would widen the signals timewise leading to a more easily detectable signal for the filters. **ToDo** **ToDo**

5.6. Photo Multiplier Tube Test with ^{90}Sr source

With sets of four photomultiplier tubes being read out over one cable, and, consequently, via one channel, the test of individual PMTs is not trivial. Nevertheless, a method using a MBq ^{90}Sr source to trigger events was used to check functionality. Of course, all tubes were able to detect the source's β-electrons at any position but rates were expected to rise as the distance to one of the tubes shrank. A source holder was constructed from acrylic glass to shield the user from radiation and to attach the source to the modules, as a large dependence of rate on the position was found when the source was simply duct taped to the modules. As the foil mantling of the modules absorbs a large part of the radiation emitted from the source, it had to be ensured that the number of layers was equal for all measurements. This was given only below the modules as the foil has been folded around them at the ends in a gift wrapping way. Thus, the source was pretty far away from the photomultiplier tubes making it more difficult to distinguish between them. A first measurement was to check for exactly this distinguishability.

The first though of being able to clearly identify the single PMT positions was soon dropped as all of the PMTs seemed to detect too much of the source's decays at any position (figure **??**). This behaviour got worse moving away from the photomultiplier tubes as the distances to the individual tubes equalized. At the same time, the closer the source was moved to the PMT tubes, the larger the position dependence got making it difficult to compare results (figure **??**). That is why it was decided to measure at the four points the PMTs were located at and compare both the behavior of the rates and their averall value. As one can see a rise in rate at the positions the tubes are located at, it was decided that four measurements per module and side were sufficient, especially as all measurements can afterwards be compared to each other. The tube positions at **(n,n,n,n cm)** were used as **ToDo**

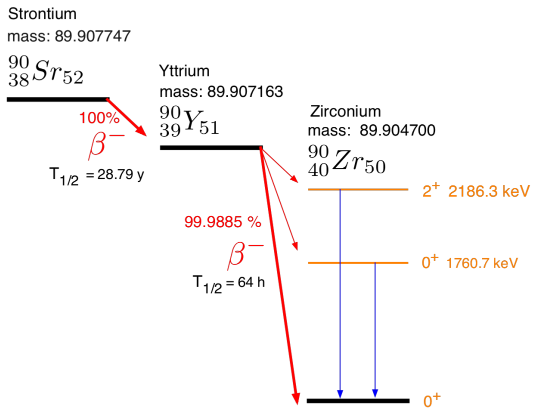

Figure 5.6.: Decay scheme of ^{90}Sr: first a lower energetic decay to ^{90}Y emitting 544 keV/c^2 electrons, from that most probably a higher energetic decay to ^{90}Zr ground state (2.29 MeV/c^2 electrons) or, with low probabilty, to one of two of its excited states.

measurement positions as well. For each side, a run has been taken containing five minute subruns for every position. Figure 5.9 to 5.11 show the result of these measurements. One can see that the general shapes compare well to the others. Exceptions are modules 2B and 6B that show lower rates than the others. This has been compensated for by a adaption of acceleration voltages.

5.7. Synchronisation of moun module and FPD DAQs

Measuring time differences between detector signals and muon events on a µs scale requires exact synchronization of the two different DAQs. For this purpose, a clock has been designed sending signals at two frequencies: one at 1 Hz and one at 10×10^6 Hz internally converted to a 20×10^6 Hz signal by the DAQ. Those signals can be synchronized to the timestamps of GPS satellites if a GPS antenna is connected. This has not yet been done as relative synchronization between the two crates is sufficient for the purposes of finding correlations between muon and detector events. As the cable length for signal transmission is pretty extensive - around 50 m - it was decided to use optical fibers instead of CAT 5 **ToDo** cabling. As two signals need to be transmitted, paired **(connection type name)** fibers were used. The clock itself has optical outputs, the DAQ though needs converters from optical to electrical signals and a modified SLT back panel card to receive the converted signals via Cat5 cabling. To test the setup, the muon DAQ was moved to the detector platform. Both crates were fed by a pulser signal. Runs at different frequencies were recorded to test both the synchronization and the detection of events. To synchronize **ToDo** timestamps to an external signal, the FLT cards drop down menu needs to be set to **(look** **ToDo** **up)** and the SLT needs to be set to **(lookup too)**. At first, manually triggered signals were used in minute runs to check the timestamps equality. Several runs were taken, all showing that the events were shifted by several µs. In close cooperation with the IPE it was found that this was merely a problem of firmware versioning as well as software settings in ORCA resolving the problem quickly. After installing the latest firmware, more runs were taken now displaying the desired behavior. The spread over the bins makes an estimate of the actual synchronization possible. Following the manually triggered events, runs with fixed frequency events were recorded, raising the frequency to up to 10 kHz. Doing so, different recording modes and filter settings were applied - see table 5.3. All the tests worked fine including starting one DAQ's run way ahead of the other or mixed filter settings. Those events recorded in both run files were always synchronized.

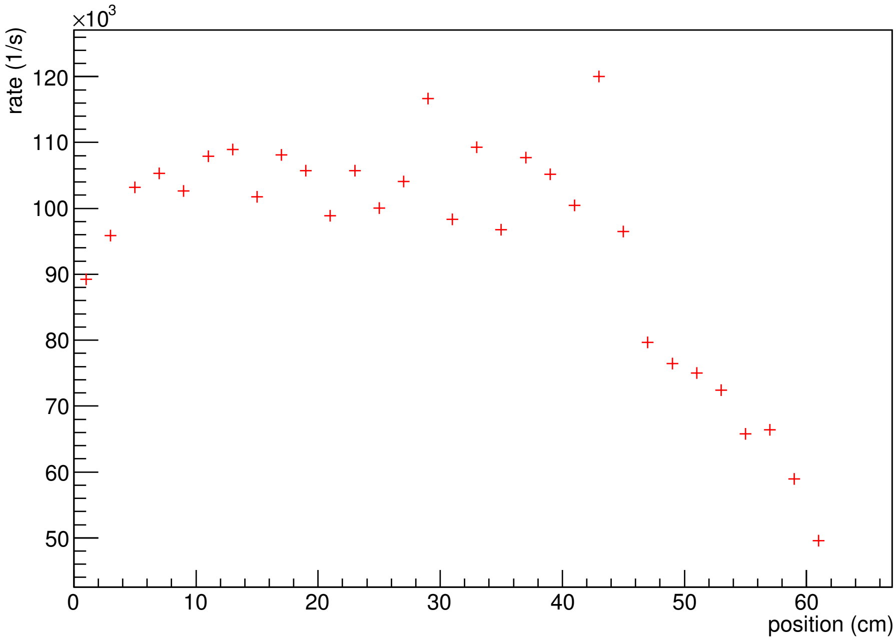

Figure 5.7.: One of multiple scans taken showing that individual PMT tube positions can not be resolved. The rate at different positions along a line parallel to the PMT alignment is plotted. Only the peripheral areas show drops in rate as the angular coverage of the source gets smaller there.

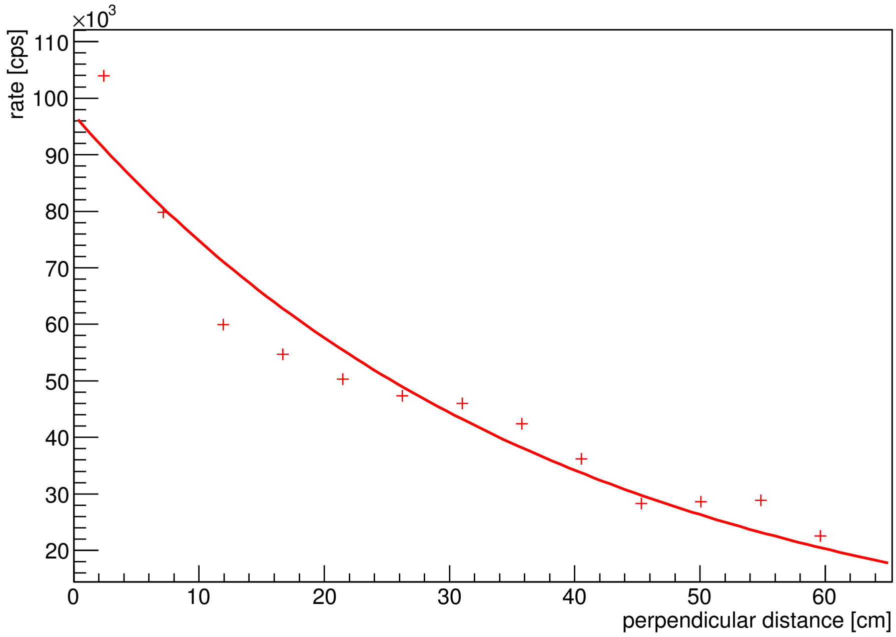

Figure 5.8.: A position scan along a line perpendicular to the PMT alignment. The rate decreases strongly as the distance gets larger.

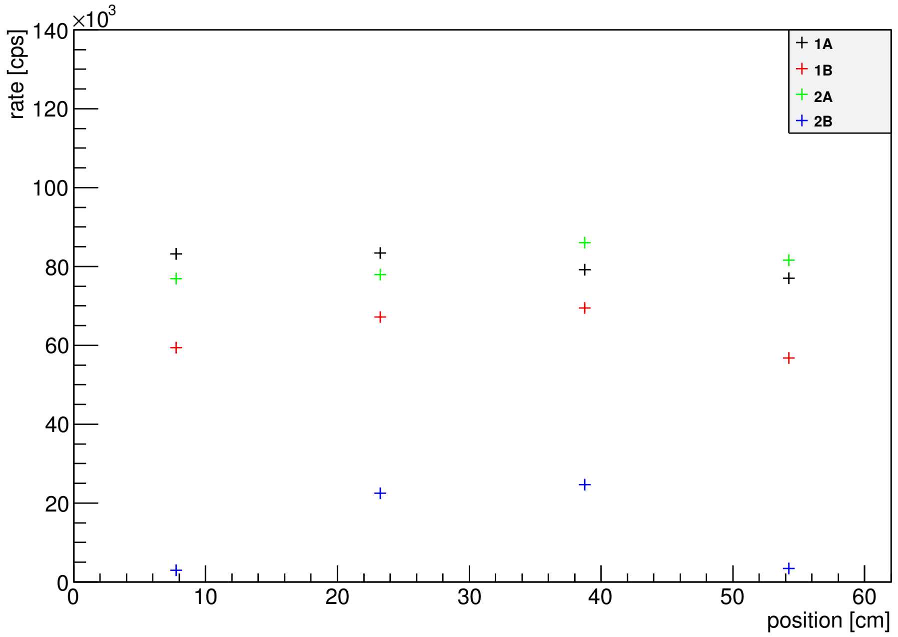

Figure 5.9.: Measurements with the source at four different positions. Both sides of modules 1 and 2. Noticable are the much lower rates for module 2B which is one of the two that was later set to 1.6 kV acceleration voltage.

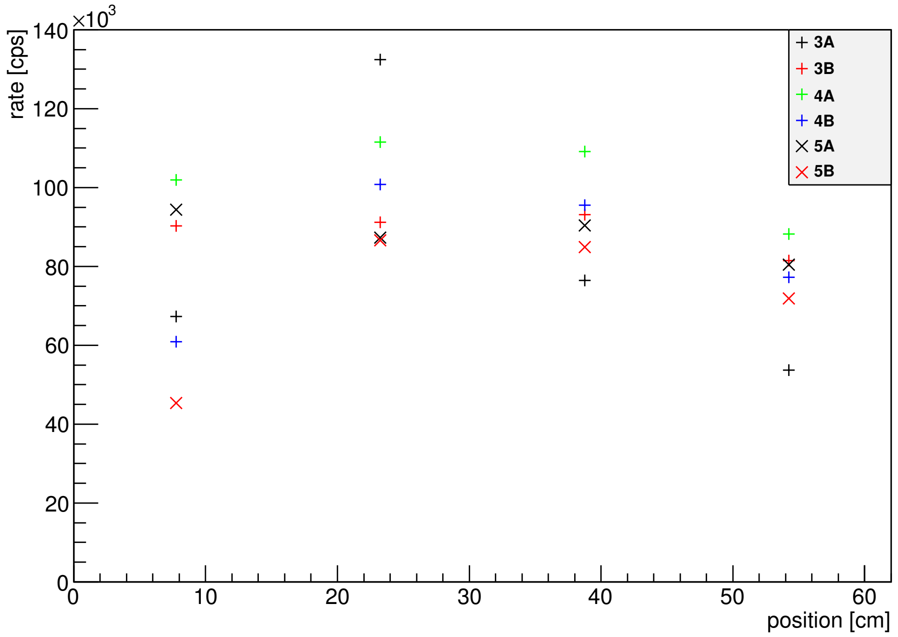

Figure 5.10.: Measurements with the source at four different positions. Both sides of modules 3 to 5 are shown. Except for single measurement points that are standing out, the different sides show similar rates.

Settings	**fpd run**	**myo run**
Pulser voltage 250mV, freq (sampling) 100000, waveform: needle negative		
as before, but 300sec runs	4174	710
as before, but 300sec runs and energy+trace mode (sync)	4175	711
5 random pulses within 60sec run	4176	712
pulser frequency: 1 Hz, 60sec run	4177	713
pulser frequency: 10 Hz, 60sec run	4178	714
pulser frequency: 100 Hz, 60sec run	4180	715
pulser frequency: 1 kHz, 60sec run	4181	716
pulser frequency: 10 kHz, 60sec run	4182	717
Pulser:		
Pulser voltage 150mV, Freq (sampling) 1000, waveform: Pin diode negative		
5 random pulses within 60sec run	4184	719
increased thresholds from 500 to 1000 (both) pulser frequency: 1 Hz, 60sec run	4185	720
pulser frequency: 10 Hz, 60sec run	4186	721
pulser frequency: 10 Hz, 300sec run	4187	722
pulser frequency: 100 Hz, 300sec run	4188	723
pulser frequency: 10 Hz, 300sec run	4189	724
Removing Cat5 cables from synchronization clock and installing fiber optic cables + converter boxes		
pulser frequency: 0.2 Hz, 60sec run	4190	725
5 random pulses within 60sec run, both energy mode	4191	726
pulser frequency: 1 Hz, both energy mode, 60sec run	4192	727
pulser frequency: 10 Hz, both energy mode, 60sec run	4193	728
pulser frequency: 10 Hz, both energy mode, 300sec run	4194	729
pulser frequency: 100 Hz, both energy mode, 300sec run	4195	730
pulser frequency: 10 Hz, both energy+trace (sync) mode, 300sec run	4196	731

Table 5.3.: All settings including run numbers tested with the two DAQs from detector system and muon modules. In the leftmost column, pulser settings and run lengths are described. In front of the different parts the pulser settings kept constant for the following measurements are described.

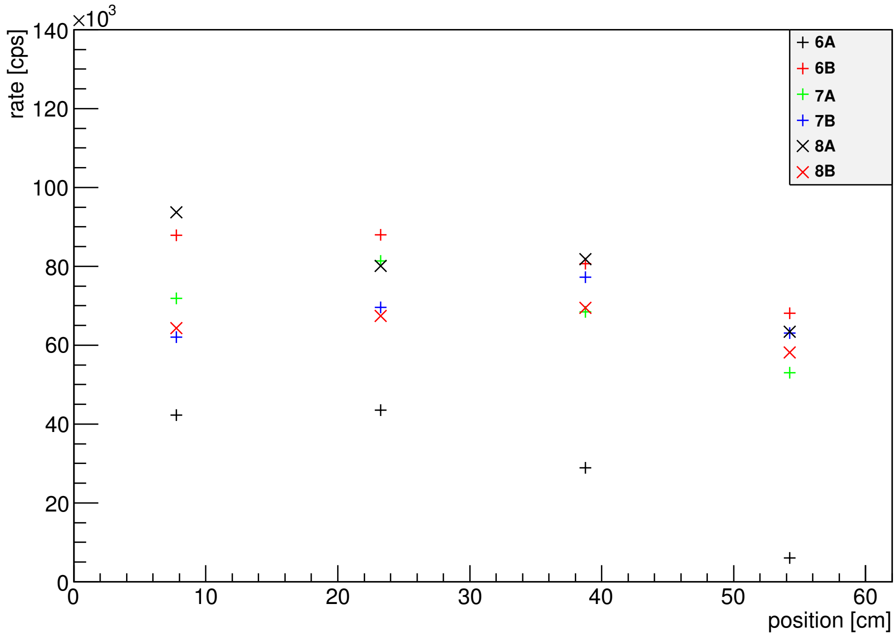

Figure 5.11.: Measurements with the source at four different positions. Both sides of modules 6 to 8. Noticable are the lower rates for module 6B which again is one of the two that was later set to 1.6 kV acceleration voltage.

Afterwards, the muon DAQ was moved back to its original position and the optical fibers were stowed in wire-ways guiding it from the detector platform down to the basement where the muon detection system is located. Another problem occurred here, as signal transmission was impaired by a kink at one of the turns, but was quickly resolved by smooth rewiring. Concluding, it can be said that the clock runs continuously without any problems throughout all the measurements - including main spectrometer commissioning measurements.

5.8. Coincidence Search between Muon- and Detector Events

If one wants to actually detect background induced by muonic events detected by the muon modules, those events need to be correlated to detector events time wise. For this purpose, the analysis code's class run was extended by the member functions TOFHist()4.3 and TOFMuonDet()4.3, where the former is used for monitor spectrometer analysis and the latter for the main spectrometer. The biggest difference is that, for the main spectrometer, runs by two DAQs leading to different starting times and different lengths are created that need to be compared. Here, the necessity for synchronization from chapter 5.7 becomes clear. Different magnetic field configurations were used that can be split into two generalized groups.
Asymmetric magnetic fields are configurations in which the magnetic field lines do not pass through the spectrometer vessel, but are widened to hit the spectrometer wall. This way, muon induced secondary electrons are guided to the detector on cyclotron tracks around those field lines.
In non-axially symmetric configurations, the fieldlines show no rotational symmetry around the z-axis. This change in fields is achieved by an additional coil on top of the monitor spectrometer vessel. At the main spectrometer, it would only be possible using the EMCS coils 2.2.7 but no measurements of that kind have been taken until now.

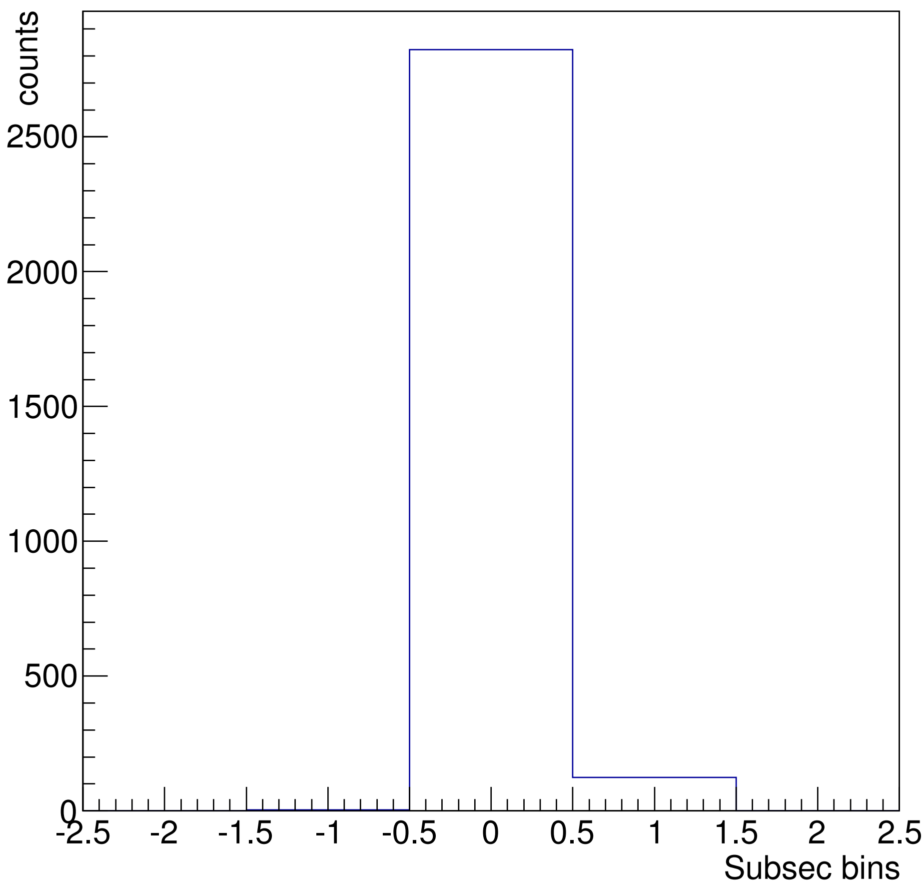

Figure 5.12.: Time differences between events after firmware upgrades. The difference in subsecond counts, i.e multiples of 50 ns is displayed. Differences between the event times are within one bin.

5.8.1. Monitor Spectrometer

Measurements at the monitor spectrometer are easily manageable due to the fast accessibility of all the components and the collection of data in a single run-file through the mini-crate. ToDo For measurements, high voltage supplies have been added to the **(name of the rack)** rack and the muon modules were connected to a newly added second FLT-card. Readout was handled by the mini-DAQ , the new FLT card was operated in veto-mode. Gains and thresholds were easily set as only four sides had to be adjusted - compared to the 16 main spectrometer channels. The PMT tubes were operated at 1.5 kV. The detector gain and threshold settings for the 5 pixel detector have been kept at standard monitor spectrometer operation settings. The detector position though was shifted to the position at which the center pixel exhibited maximum rate and the pairs of east-west and top-bottom pixels showed comparable count rates. Furthermore, the recording mode was switched from histogram-mode to energy-mode as the timestamps for every single event were needed for analysis. Several hourly runs were taken under different magnetic field compositions. Both asymmetric magnetic field (see table 5.4 and non-axially-symmetric field (see table 5.5 configurations were investigated.

The TOFHist function (chapter 4.3) has been used to analyze the data as well as "Beans" code. Both browse through all the muon-events detected and finds any detector event in a definable timespan after (or before) the muon-event. This can be more than one detector-event per muon-event. In all of the settings, a peak is visible at around 2 µs. Count rates are a lot higher in the asymmetric magnetic field setup as secondary electrons are guided from their point of origin to the detector instead of mostly being magnetically shielded. In this setup, only the reflection through the rise in magnetic field on the electrons' paths takes its toll on the rate (see section 2.1.1). As data with a lot of different field configurations was analyzed, the major part of setups and analysis can be found in the annex on pages 79. The asymmetric magnetic field measurements show the expected behavior. With high field strengths at the wall, i.e. dense field lines, the angular acceptance is high and the peak is clearly distinguishable (see figures E.5 and E.4). As the field strengths decrease, the peak

Run	solenoid source	solenoid detector	inner aircoil	outer central aircoil	outer aircoil	emcs x	emcs y
mos00159395	0	25	0	-4	-4	2	-19.5
mos00159396-mos00159398	0	50	0	-8	-8	2	-19.5
mos00159399	0	50	0	-7	-7	2	-19.5
mos00159400	0	50	0	-6	-6	2	-19.5
mos00160713-mos00160717	0.1	12.5	0	-2	-2	0	0
mos00160718-mos00160730	0.1	12.5	0	-2	-2	0	0
mos00161105-mos00161107	0.1	12.5	0	-2	-2	0	0
mos00161108-mos00161110	0.1	25	0	-2	-2	0	0
mos00161108-mos00161110	0.1	25	0	-2	-2	0	0

Table 5.4.: Measurements at asymmetric magnetic fields. The source side magnet was turned off for all measurements leaving the flux tube entering the spectrometer walls.

Run mos00...	**2 Horizontal loops**	solenoid source	solenoid detector	inner aircoil	outer aircoil	outer cent. aircoil	EMCS x	EMCS y
161111-161125	0	25	25	6.8	-7	5	0	-14
161126-161129	+50	12.5	12.5	3.5	-3.5	2.5	0	0
161130-161133	+25	12.5	12.5	1.75	-1.75	1.25	0	0
161134-161149	-25	12.5	12.5	1.75	-1.75	1.25	0	0
161150-161155	-50	12.5	12.5	3.5	-3.5	2.5	0	0
161156-161158	0	12.5	12.5	3.5	-3.5	2.5	0	0

Table 5.5.: Measurements in energy mode at non axially symmetric magnetic field. Both solenoid and air coil currents have bee changed, though always by a multiplication factor for all of them so that the ration remained the same.

height falls in correlation to the surrounding noise until it is indistinguishable (pages 79 to 83).
Non axially symmetric setups also generally showed more muon induced counts the more deformed the field was (pages 84 to 89). One exception is the setup in figure E.14 showing only few events (figure E.15). A possible explanation here is the flux tube moving off center. All in all, the mechanism of muon inducing secondary electrons that are then being guided to the detector was confirmed. And, even more importantly, the very good shielding of the symmetrical flux tube was demonstrated. Once again, the necessity of well known symmetric fields was demonstrated.

5.8.2. Main Spectrometer

Monitor-spectrometer results suggested that the time of flight was well measurable, even if on bigger scale, at the main spectrometer. So, during commissioning measurements, already parallel to first measurements “M1”, some runs with asymmetric magnetic field have been taken with switched polarity or turned off pre spectrometer magnets compared to standard setup. The data was analysed for each single ring of the FPD. Search parameters were the time slot from 0 s to 15 µs. Data remained inconclusive at the time (figure **??**). The failure to find a clear runtime for electrons induced by muonic events might have been due to the combination of muon module position and the magnetic field setup. In the first measurements, the wall area covered by the flux tubes and the volume surveilled by the muon modules did not overlap very much. Furthermore, due to the very low magnetic field at the wall compared to the volume inside the detector and pinch magnet, most of the induced electrons are magnetically reflected as the maximum polar angle towards magnetic field lines θ_{max} is defined by

$$\frac{B_{min}}{B_{max}} \approx \frac{3\,\mathrm{G}}{4\,\mathrm{T}} = sin^2(\theta_{max}) \tag{5.6}$$

meaning only angles satisfying the inequation

$$\theta < \arcsin\sqrt{\frac{B_{min}}{B_{max}}} = \arcsin\sqrt{\frac{3\,\mathrm{G}}{4\,\mathrm{T}}} = 0.004° \tag{5.7}$$

will be able to reach the detector. All others will be reflected and fly back to the wall to be absorbed in the conducting wall material. **ToDo** **(set real field values)** As a result, compared to the monitor spectrometer, where the ratio is a lot greater, less of the muon induced electrons arrive at the detector making long measurements a requirement for good statistics. This leads to detector rates of only around 2 cps, depending on the inner electrode voltages. At high inner electrode voltages, the rate increases strongly to 150 cps which is probably due to field emission from the electrodes. Here, the rate of events actually analyzed can be reduced by using energy cuts and excluding pixels with either known problems - for example the two defective pixels - or such covered by the misaligned flapper valve. The energies were cut below 25.6 keV and above 30.6 keV including the PAE voltage of 10 kV.

Analysis for every single pixel was not possible due to far too low statistics, though it might be more conclusive as less different path lengths can contribute to a single pixel. On the other hand, after the non-central alignment of the detector has been fixed using different settings for the LFCS-system, the fields should be rotationally symmetric around the z-axis disregarding small deviations. Assuming this, the path lengths for every pixel of one ring should be very comparable.

In the anticipation of better results, different field configurations were used. One widened the flux tube so the coverages of the volume surveilled by the muon detectors and the flux tube got larger. (figure 5.15). The second configuration also densified the field lines in

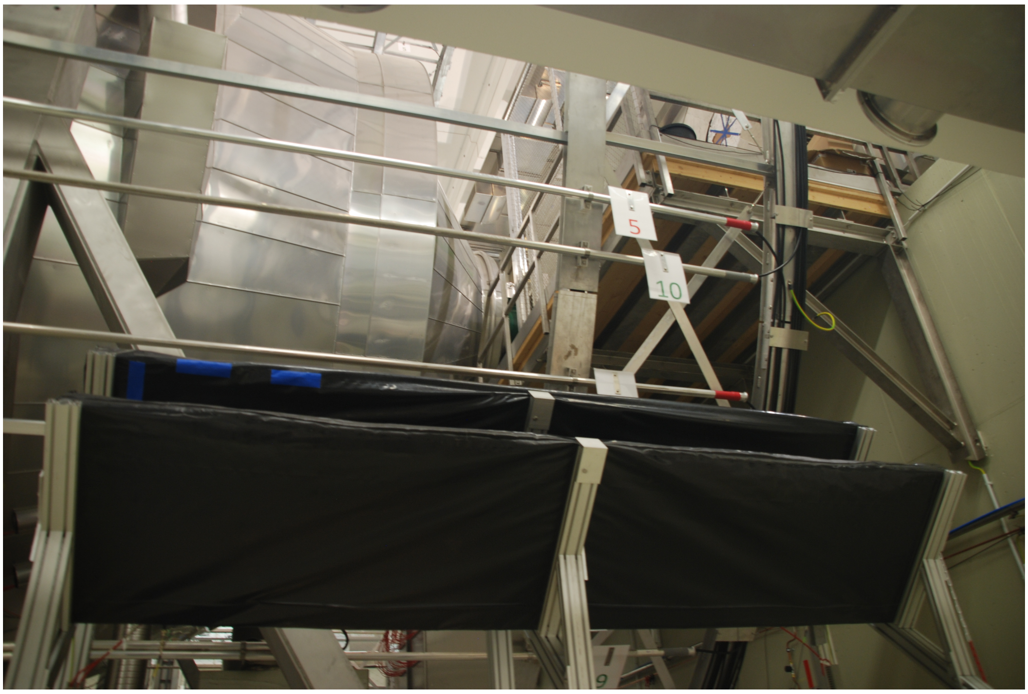

Figure 5.13.: A photograph of modules 1 and 2 after being moved into a position observing the steep cone rather than the central

the area of the muon modules. This again raised the probability of seeing electrons from detected muons at the detector, but also raised the angular acceptance by increasing the magnetic field at the walls by a factor of two (figure **??**). All in all, three different magnetic field configurations were used, they are shown in figures 5.14, 5.15, 5.16 and described in tables 5.7 and 5.6.

To raise the overall acceptance of the muon induced events, these measurements were repeated with the main vessel on high voltage of 18.6 kV accelerating all the electrons towards the FPD. This was done for measurements “C” (table 5.6). The setup was changed as the flux tube was returned to its initial setting (figure 5.14) but the muon modules were moved towards the steep cone now surveilling exactly this region of interest (figure 5.13).

None of the settings showed time peaks as clear as the monitor spectrometer. Simulations of single events show that the fastest particles arrive after times comparable to the ones of the monitor spectrometer, i.e. at 1.5 µs (figure **??**). This already poses a problem. The anticipated rate of muons through the area of the main spectrometer covered by the flux tube is

$$r_\mu A_{MS} = 1/\mathrm{cm}^2\,\mathrm{s} \cdot 66\,\mathrm{m}^2 = 660\,000\,\mathrm{s}^{-1}. \tag{5.8}$$

The area has been taken from [**?**]. This means that the average time between muon events of $1/660\,000\,\mathrm{s} \approx 1.5\,\mu\mathrm{s}$ is of equal size as the time of flight for a single electron. This of course makes it difficult to distinguish between the different events. The measurements with field setting “C” were not as promising as previously thought despite the larger acceptance angle. The ones on high voltage showed a lot higher rates, though a lot of this effect may be cotributed to field emission. There are runs in which one could interpret peaks at the position of the simulation, though all of these are small compared to ambient signals. The most prominent one is displayed in figure 5.18. It could be interpreted as a signal peak with a exponential tail. This remains very speculative at the moment. Further measurements with magnetic field setups reducing the overall area of the flux tube covered might shed more light on this. Sadly, as the time of the commissioning measurements was limited, these have to be taken at a later date.

measurement setting	myo start	end	fpd start	end
A1	5159	5164	939	949
	5166	5172	950	977
B	5255	5256	1052	1055
A2	6306	6307	1090	1096
	6308	6311	1097	1104
	6312	6315	1105	1112
	6316	6321	1113	1124
	6322	6327	1125	1136
	6328	6333	1137	1148
C	6401	6404	1226	1229
	6405	6408	1230	1233
	6409	6412	1234	1237
A3	7111	7134	1301	1325

Table 5.6.: Main spectrometer runs taken for the search of muon induced background events. The runs are split into groups of same magnetic field settings. The individual settings are listet in 5.7. All group member have different inner electrode voltages, refer to appendix for those as well.

Measurement setting	IE[V]	PS I [T]	PS II [T]	Pinch [T]	Det [T]	LFCS [A]	EMCS h [A]	EMCS v [A]
A1, A2, A3	-700	0	0	5	3.5	#1 - #13: 100 A; #14: 0 A	50	9
B	0	0	0	5	3.5	#1 - #3: 0 A; #4: 50 A; #5 - #13: 100 A; #14: 0 A	50	9
C	-600	0	0	5	3.5	#1 & #2: -50 A; #3: 0 A; #4 - #13: 100 A #14: 70 A	40	9

Table 5.7.: Magnetic field settings for the individual groups from table 5.6

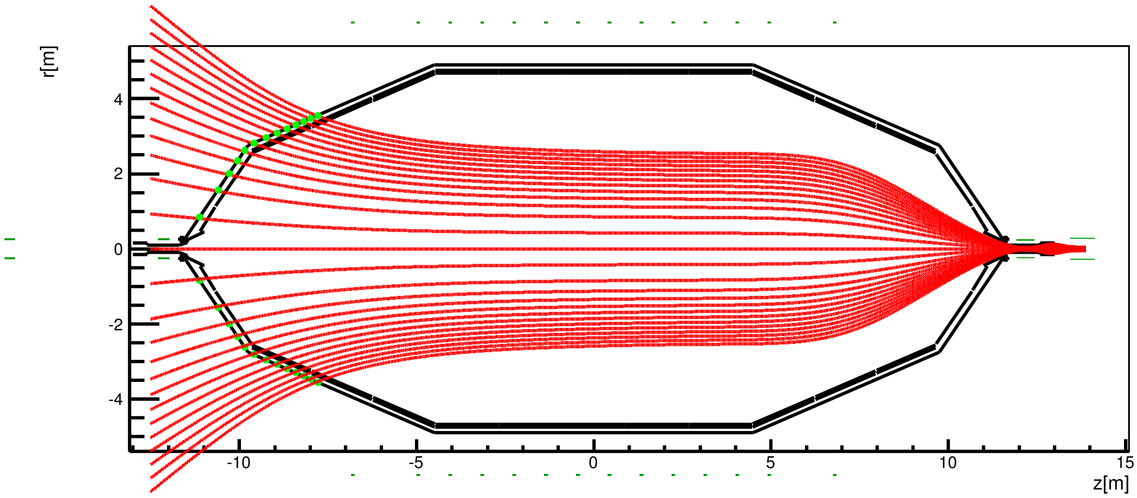

Figure 5.14.: First used magnetic field setup. Note that the largest part of the flux tube is in the area of the steep cone. With the initial positions of the muon modules, the probability of the detected muons having caused secondary electrons inside the flux tube was too low.

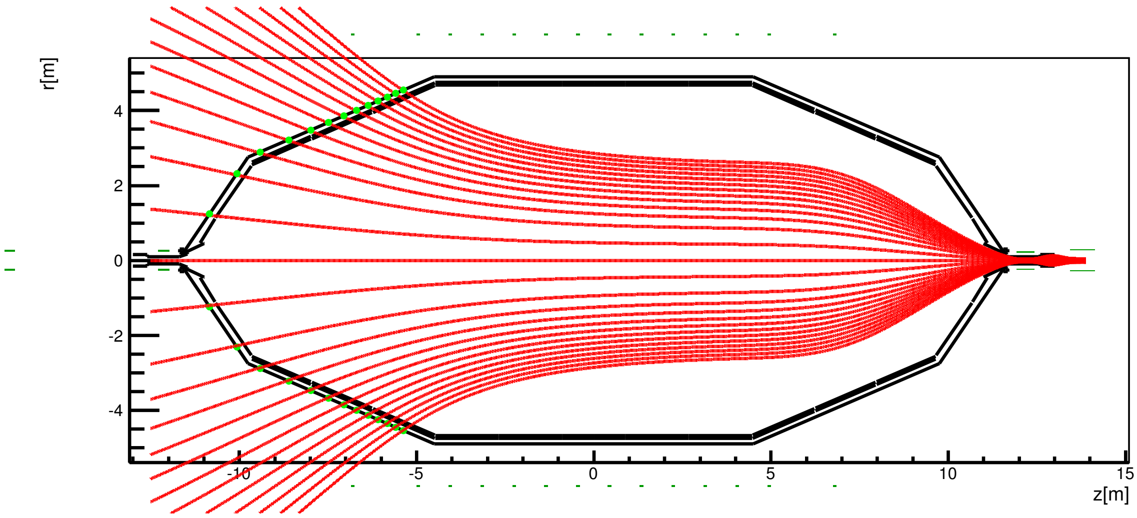

Figure 5.15.: Widened magnetic flux tube for better coverage by the muon modules. The flat cone is now almost completely covered.

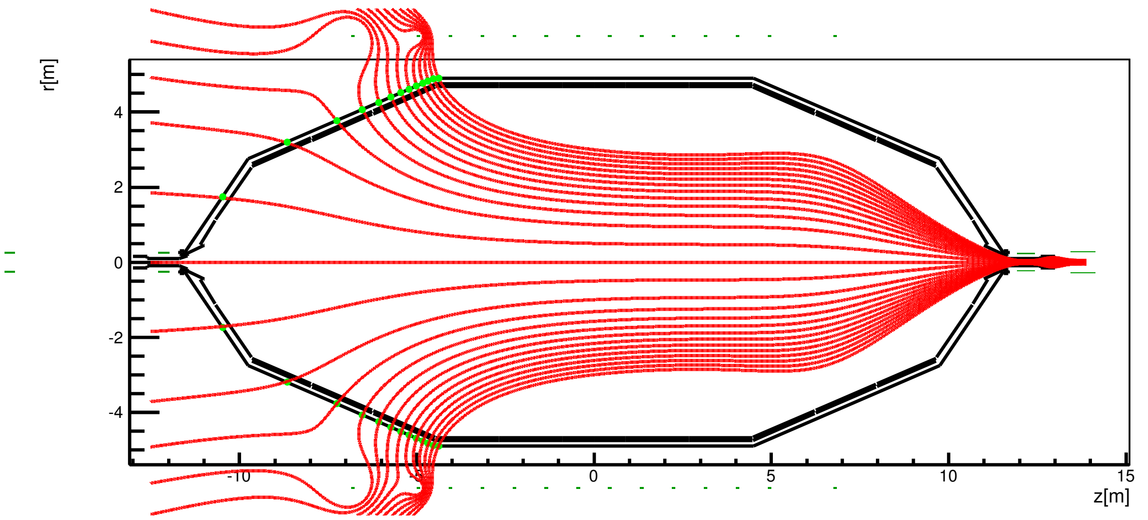

Figure 5.16.: Flux tube as proposed in [61]. Here, two LFCS coils on the source side were operated with switched polarity. This creates a denser flux tube in the region of interest.

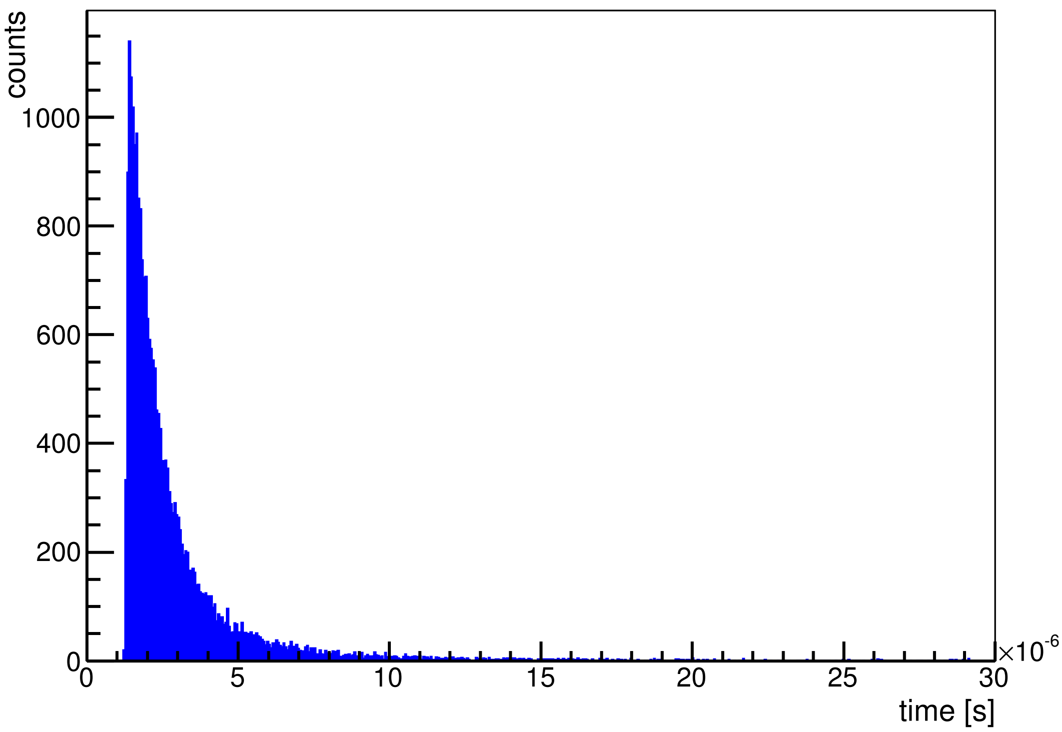

Figure 5.17.: Time of flight for simulated electrons starting at the spectrometer wall. The "fastest" electron arrives at 1.5 µs. The distribution has an exponential charakter.

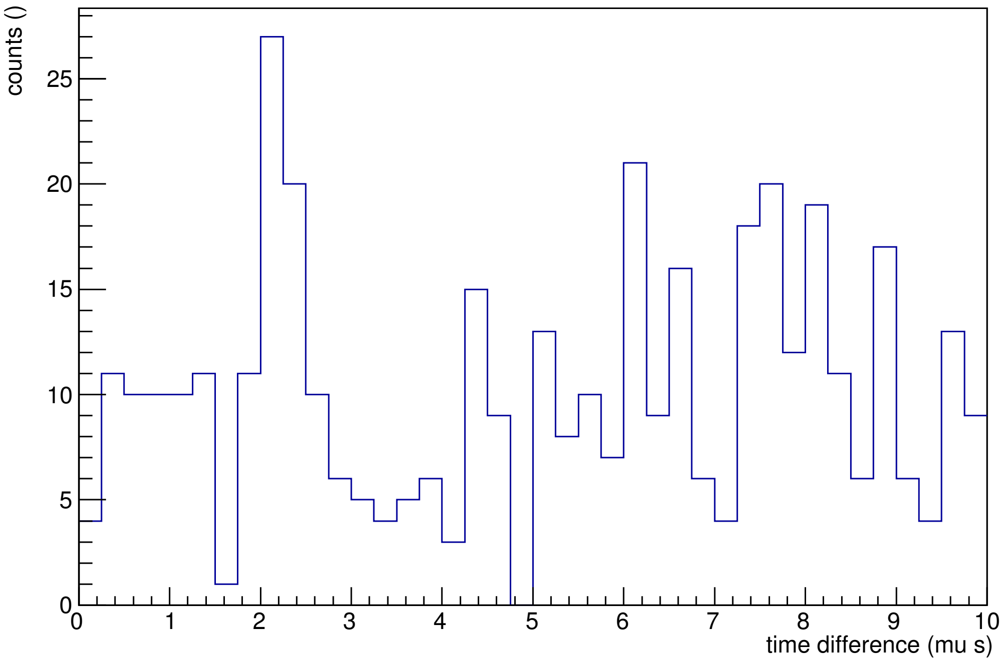

Figure 5.18.: The mos promising result so far for the main spectrometer. The peak at around 2 µs resembles the simulation with its exponential tail. The counts before after might already be other muon induced events.

6. Simulation of muon induced background

To compare the data aquired to theoretically expected values, a Geant4 simulation of cosmic showers has been set up including the geometry of the main spectrometer as well as the muon modules. Using this software, any number of inciding muons can be simulated and the effect on the main spectrometer and the muon modules can be evaluated. It was especially relevant to achieve estimations on which amount of the muons travelling through the main spectrometer would be registered by the muon modules. This would then make it possible to estimate the overall rate and probabilities for muons inciding to also induce electrons etering the spectrometer.

6.1. Geant4

The Geant4 package is a powerful tool for simulation of particles. It has loads of possible interactions already integrated making it easy for the user to set up and run simulations. After setting up geometry and detectors, the user starts a run. Each run may consist of one or more events. During a single run, a loop of processes is called:

- Primary Generator Action
- Run action
- Event action
- Stacking action
- Tracking action
- Stepping action

Of course inside each run usually there are many event actions and inside every event action, there are multiple tracking actions. For user interaction, for each item above, classes with the addition 'user' to the base classes name can be called before or after the standard action class. An example is the class G4UserEventAction invoked before and after each call of G4TrackingAction. It contains two member classes, namely BeginOfEventAction and EndOfEventAction that let the user decide what to do at this point. Through those, it is possible to change behavior of the simulation or extract data needed. In this case, for every event, if more than one module has been hit, the copy numbers of those are pushed back to a vector of event data. Running the simulation, one can either interactively enter commands or write those to a .mac file, by default the vis.mac file, which are then sequentially executed.

6.2. Geometry setup

To set up a geometry, the class G4VUserDetectorConstruction is used. B1DetectorConstruction inherits from that as a base class and additionally contains all of the geometrical parameters needed for the setup such as radii of the main spectrometer cones or positions and extent of the muon modules. Every shape generated is made up of both a logical volume G4LogicalVolume and a physical volume G4PhysicalVolume. The logical volume describes the intrinsic properties of the geometric object added: its shape, its size and its material. The physical volume accepts a logical volume as input providing position and alignment of the previously defined. Inside the detector construction class, all of the materials used in the simulation need to be defined as well. These are the components of the air outside and inside the spectrometer including pressures and constitution, the stainless steel of the spectrometer wall and the scintillator material of the muon modules. The main spectrometer geometry was already **(written by who?)** existent but had to be modified as many border volumes were implemented. These were very flat volumes covering any area of the main spectrometer not needed for this simulation. Additionally, the muon modules have been added as sensitive volume. Keeping in mind that one wants to not only distinguish whether a module has been hit, but also which one. That is why the logical volume for every module is the same whereas the physical volume is a copy of the first at different world coordinates making them identifiable via their individual copy number.

ToDo

6.3. Muon generator

Muon generation was realized through the primary generator action. The angular distribution suggested by Henrik Arlinghaus [62] was implemented. The angular rate dependence is shown in 6.2.The energy was set to **(reasonable value)** disregarding the actual energy distribution as this was mainly about flight paths that are not strongly dependent on energy at high energies. Starting positions were spherically distributed, with the direction towards the origin, which is in the center of the main spectrometer. Positions were then randomly moved in a volume surrounding the spectrometer to account for the non-point like structure of the detection system as a whole, while the distribution describes a single point in space. The distribution used is the cos* distribution.

ToDo

$$\cos^*(\theta) = S(\Theta)\cos^{**}(\theta) \tag{6.1}$$

with

$$S(\theta) = 0.986 + 0.0007\sec\theta \tag{6.2}$$

and $S(\theta)$ described by a polynomial

$$\sum_{i=0}^{4} c_i \cos^i\theta. \tag{6.3}$$

The coefficients are defined differently for different angular ranges shown in table **??**.

6.4. Visualisation - the vis.mac file

To display results of a the calculations made, the tracks of all particles can be displayed as well as the geometry setup itself. This can be done interactively after running the program,

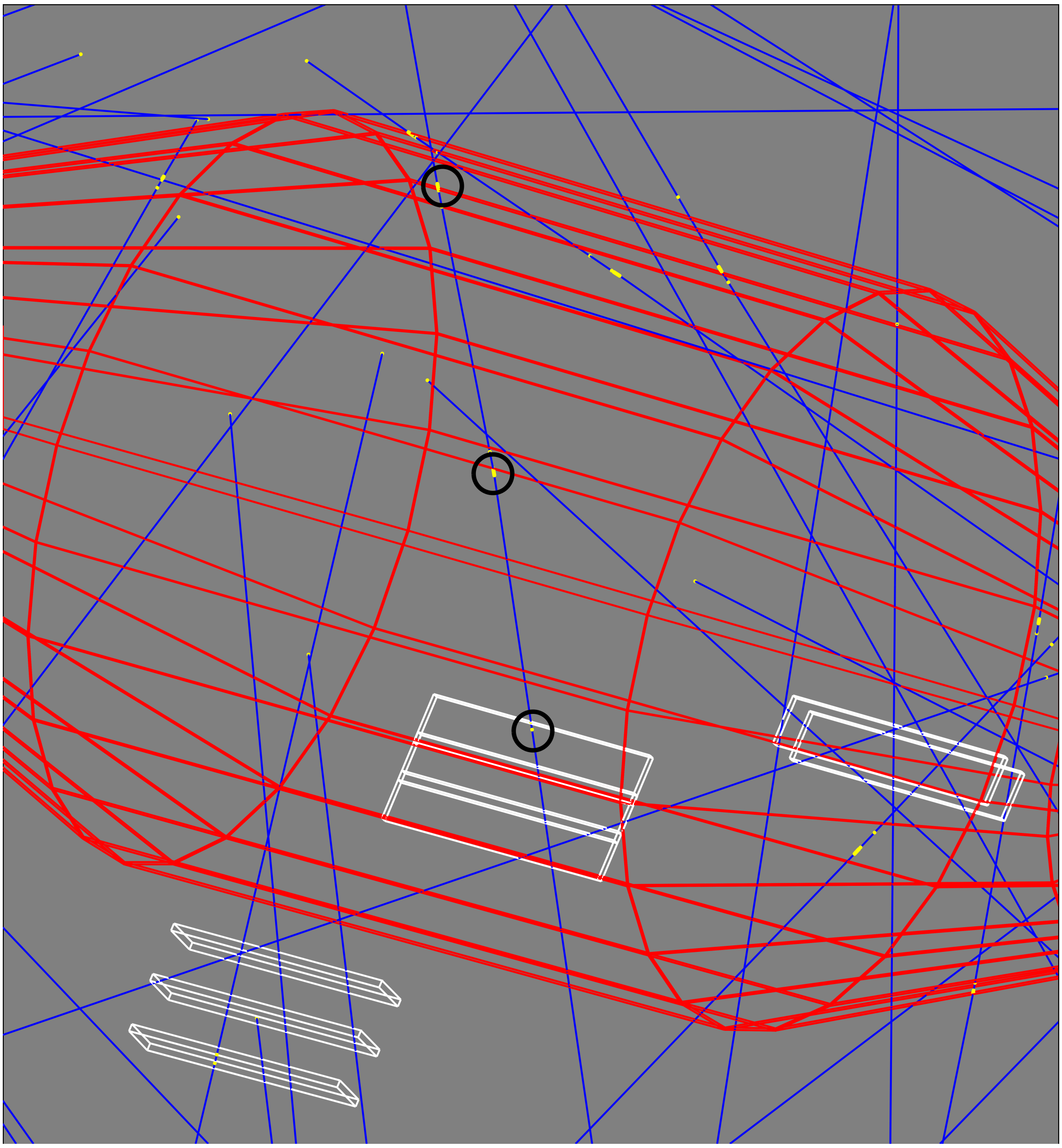

Figure 6.1.: The image shows a screenshot of the geometry setup as displayed in the OpenGL viewer. The view is upwards through the main spectrometer standing on the west side of it. The three groups of muon modules (white) are visible right below the large main spectrometer structure (red). A variety of incident muons is shown (blue). Hits are set to be marked yellow by the Geant4 viewer. Additionally, the hit points of one muon hitting a muon detector have been circled black. One can see both entry and exit point of the main spectrometer and the detection point.

$\cos(\theta)$	c_0	c_1	c_2	c_3	c_4	max. rel. error
0 - 0.002	0.11137	0	0	0	0	0.004
0.002 - 0.2	0.11148	-0.03427	5.2053	-14.1971	6.138	0.3
0.2 - 0.8	0.06714	0.71578	0.42377	-0.19634	-0.021145	0.7

Table 6.1.: These are the coefficients for equation 6.3. every set of coefficients is applicable to a certain angular region indicated in the first column. the last column shows the largest occurring relative error in each region.

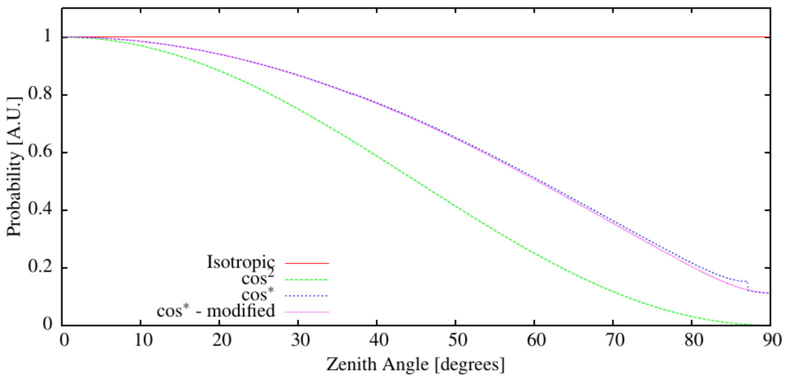

Figure 6.2.: Different distributions of

though the faster approach is to use *.mac files, standardly the vis.mac file. Here, different parameters can be changed and simple visualisation settings like viewing angles and zooms can be chosen. For an example of a vis.mac file see annex G.
Included are

-

6.5. Hit counter

For comparing the simulation to real data, of all the events generated, those hitting modules were counted. Each event containing at least one hit is written into a file for further analysis. To do so, the functions UserSteppingAction inheriting from G4UserSteppingAction, EndOfEventAction inheriting from G4UserEventAction and EndOfRunAction inheriting from G4UserRunAction are used. They are handing the information up from function to function. At the end of a run, the results of every single event are written to a file called hitOutputAll while those containing only such events in which the muon hit the spectrometer and at least one of the muon modules are written to the file hitOutput. This made it possible to compare the rates of the single modules, showing that the generator works fine. furthermore, it allowed for a estimation of muons hitting the modules compared to the total of inciding muons. This work should now be continued. Muons that hit the main spectrometer and were detected by the muon modules should be saved. The entry and exit points into and out of the main spectrometer can then be recycled. Electron tracking from these points can give information on the rates induced by detected muons to be expected at the detector. This can then further improve the understanding of the main spectrometer background processes.

7. Conclusion

The whole muon detection system has been set up at the main- and readopted at the monitor spectrometer. Both systems are able to take data at rates that compare well to literature values.

It was shown that the muon induced electron rate is well shielded by axially symmetric magnetic fields and that, under circumstances differing from those, this rate increases strongly.

8. Outlook

…

Bibliography

[1] E. Fermi. Versuch einer theorie der β strahlen. 1934. [Online, accessed 06-09-2013].

[2] C. L. Cowan, F. Reines, F. B. Harrison, H. W. Kruse, and A. D. McGuire. Detection of the free neutrino: a confirmation. *Science*, 124(3211):103–104, 1956. [Online, accessed 06-09-2013].

[3] G. Danby, J-M. Gaillard, K. Goulianos, et al. Observation of high-energy neutrino reactions and the existence of two kinds of neutrinos. *Phys. Rev. Lett.*, 9:36–44, Jul 1962.

[4] K. Kodama, N. Ushida, C. Andreopoulos, et al. Observation of tau neutrino interactions. *Physics Letters B*, 504(3):218 – 224, 2001.

[5] Bethge and Walter. *Kernphysik*. Springer, 2006.

[6] F.P. An et al. Observation of electron-antineutrino disappearance at daya bay. *Phys. Rev. Lett. 108*, 108, 2012.

[7] S. Chatrchyan, V. Khachatryan, A.M. Sirunyan, et al. Observation of a new boson at a mass of 125 gev with the {CMS} experiment at the {LHC}. *Physics Letters B*, 716(1):30 – 61, 2012.

[8] G. Aad, T. Abajyan, B. Abbott, et al. Observation of a new particle in the search for the standard model higgs boson with the atlas detector at the lhc. *Physics Letters B*, 716(1):1 – 29, 2012.

[9] W. Rodejohann. standard model elementary particles. `http://www.mpi-hd.mpg.de/manitop/StandardModel/pics/standard_model_elementary_particles.png`, 2013. [Online, accessed 05-09-2013].

[10] M. Ageron et al. ANTARES: the first undersea neutrino telescope. *Nucl.Instrum.Meth.*, A656:11–38, 2011.

[11] M.G. Aartsen et al. Measurement of the Atmospheric ν_e flux in IceCube. *Phys.Rev.Lett.*, 110:151105, 2013.

[12] K. et al Abe. Evidence for the appearance of atmospheric tau neutrinos in super-kamiokande. *Phys. Rev. Lett.*, 110:181802, May 2013.

[13] Zhou Bin, Ruan Xi-Chao, Nie Yang-Bo, Zhou Zu-Ying, et al. A study of antineutrino spectra from spent nuclear fuel at daya bay. *Chinese Physics C*, 36(1):1, 2012.

[14] M. Maltoni, T. Schwetz, M. A. Tórtola, and J. W. F. Valle. Status of three-neutrino oscillations after the sno-salt data. *Phys. Rev. D*, 68:113010, Dec 2003.

[15] R. Davis. A review of the Homestake solar neutrino experiment. *Prog.Part.Nucl.Phys.*, 32:13–32, 1994.

[16] J. Beringer et al. 2012 review of particle physics. *Phys. Rev. D86*, 010001, 2012.

[17] Michael Wurm et al. The next-generation liquid-scintillator neutrino observatory LENA. *Astropart.Phys.*, 35:685–732, 2012.

[18] G. Drexlin, V. Hannen, S. Mertens, and C. Weinheimer. Current Direct Neutrino Mass Experiments. *ArXiv e-prints*, June 2013.

[19] Beth A. Reid et al. Cosmological Constraints from the Clustering of the Sloan Digital Sky Survey DR7 Luminous Red Galaxies. *Mon.Not.Roy.Astron.Soc.*, 404:60–85, 2010.

[20] E. Komatsu, Smith, et al. Seven-year Wilkinson Microwave Anisotropy Probe (WMAP) Observations: Cosmological Interpretation. *apjs*, 192:18, February 2011.

[21] P.A.R. Ade et al. Planck 2013 results. XVI. Cosmological parameters. 2013.

[22] D. A. Knapp R. G. H. Robertson. Direct measurements of neutrino mass. *Annual Review of Nucear Science*, 1988.

[23] E. Andreotti, C. Arnaboldi, et al. Mare, microcalorimeter arrays for a rhenium experiment: A detector overview. *Nuclear Instruments and Methods in Physics Research Section A: Accelerators, Spectrometers, Detectors and Associated Equipment*, 572(1):208 – 210, 2007. Frontier Detectors for Frontier Physics - Proceedings of the 10th Pisa Meeting on Advanced Detectors.

[24] Todor Stanev. *High energy cosmic rays : with 19 tab.* Springer-Praxis books in astrophysics and astronomy. Springer, Berlin, 2. ed. edition, 2004. 2010 nochmals eine 2. ed. erschienen.

[25] Anais Schaeffer. `http://cds.cern.ch/record/1345733/files/Cosmic_image.jpg`, 2013. [Online; accessed 01-09-2013].

[26] Claus Grupen. *Astroparticle Physics.* Springer, Berlin [u.a.], 1. ed. edition, 2005.

[27] S. Hayakawa. *Cosmic ray physics. Nuclear and astrophysical aspects.* 1969.

[28] T. P. Gorringe. MuLan Measurement of the Positive Muon Lifetime and Determination of the Fermi Constant. *ArXiv e-prints*, January 2013.

[29] P. Doll, W. D. Apel, J. C. Arteaga, and et al. Muon Production Height in the Air-Shower Experiment KASCADE-Grande. In *International Cosmic Ray Conference*, volume 4 of *International Cosmic Ray Conference*, pages 115–118, 2008.

[30] E.W. Otten and C. Weinheimer. Neutrino mass limit from tritium beta decay. *Rept.Prog.Phys.*, 71:086201, 2008.

[31] J. Wolf. The katrin neutrino mass experiment. *Nuclear Instruments and Methods in Physics Research Section A: Accelerators, Spectrometers, Detectors and Associated Equipment*, 623(1):442 – 444, 2010.

[32] KATRIN. Mac e filter. `http://www.katrin.kit.edu/img/mace_electrodes_rdax_1200x1200.gif`, 2006.

[33] Markus Steidl. `http://www.katrin.kit.edu/79.php`, 2011. [Online, accesse 18-09-2013].

[34] Lyndsay. `http://www.astro.gla.ac.uk/users/lyndsay/TEACHING/NLPII/Lecture4_06.pdf`, 2006. [Online, accesse 18-09-2013].

[35] A. Osipowicza, H. Blueumer, G. Drexlin, K. Eitel, et al. Katrin: A next generation tritium beta decay experimentwith sub-ev sensitivity for the electron neutrino mass. 2002. [Online, accessed 16-09-2013].

[36] S. Grohmann, T. Bode, M. HÃ¶tzel, et al. The thermal behaviour of the tritium source in {KATRIN}. *Cryogenics*, 55â56(0):5 – 11, 2013.

[37] Magnus SchlÃ¶sser, Simone Rupp, Hendrik Seitz, Sebastian Fischer, et al. Accurate calibration of the laser raman system for the karlsruhe tritium neutrino experiment. *Journal of Molecular Structure*, 1044(0):61 – 66, 2013. <ce:title>EUCMOS XXXI</ce:title> <ce:subtitle>EUCMOS XXXI</ce:subtitle>.

[38] M. Babutzka. 24th katrin collaboration meeting - status of the rearsection. `http://fuzzy.fzk.de/bscw/bscw.cgi/d847077/95-TRP-5401-S1-MBabutzka.pptx`, 2013. [Online; accessed 01-09-2013].

[39] G. Drexlin. Wgts. `http://fuzzy.fzk.de/bscw/bscw.cgi/d736434/95-TRP-5205-S2-GDrexlin.pptx`, 2012.

[40] F. Priester. 24th katrin collaboration meeting - tritium test experiments. `http://fuzzy.fzk.de/bscw/bscw.cgi/d774076/95-TRP-5403-S1-FPriester.pptx`, 2013. [Online; accessed 01-09-2013].

[41] L. Bornschein. 24th katrin collaboration meeting - status of dps. `http://fuzzy.fzk.de/bscw/bscw.cgi/d774094/95-TRP-5405-S2-LBornschein.ppt`, 2013. [Online; accessed 01-09-2013].

[42] W. Gil. 24th katrin collaboration meeting - status of cryogenic pumping section. `http://fuzzy.fzk.de/bscw/bscw.cgi/d774107/95-TRP-5406-S2-WGIL.pptx`, 2013. [Online; accessed 01-09-2013].

[43] Joachim Wolf. Status of the pre-spectrometer of the katrin experiment. `http://www.katrin.kit.edu/publikationen/talk_DPG-2004-03-11-prespec.pdf`, 2004. [Online, accessed 17-09-2013].

[44] K. Valerius. Electromagnetic design and inner electrode for the katrin main spectrometer. *Progress in Particle and Nuclear Physics*, 57(1):58 – 60, 2006.

[45] Th ThÃ¼mmler, R Marx, and Ch Weinheimer. Precision high voltage divider for the katrin experiment. *New Journal of Physics*, 11(10):103007, 2009.

[46] K. Valerius. The wire electrode system for the {KATRIN} main spectrometer. *Progress in Particle and Nuclear Physics*, 64(2):291 – 293, 2010.

[47] T. Thümmler. 24th katrin collaboration meeting - sds status & spectrometer bake-out. `http://fuzzy.fzk.de/bscw/bscw.cgi/d774576/95-TRP-5409-S3-TThuemmler.pdf`, 2013. [Online; accessed 01-09-2013].

[48] M. Zacher. 20th katrin collaboration meeting - wire electrode system installation status. `http://fuzzy.fzk.de/bscw/bscw.cgi/d694360/95-TRP-5006-S2-MZacher.pdf`, 2011. [Online; accessed 01-09-2013].

[49] J. Schwarz. 24th katrin collaboration meeting - the focal-plane detector system. `http://fuzzy.fzk.de/bscw/bscw.cgi/d774296/95-TRP-5414-S4-JSchwarz.pdf`, 2013. [Online; accessed 01-09-2013].

[50] F. Glück et al. Air coil system & magnetic field sensor system. `http://fuzzy.fzk.de/bscw/bscw.cgi/d530439/Air%20Coil%20System%20and%20Magnetic%20Field%20Sensor%20System.pdf`, 2009. [Online; accessed 24-08-2013].

[51] S. Mertens, G. Drexlin, F.M. FrÃ¤nkle, et al. Background due to stored electrons following nuclear decays in the {KATRIN} spectrometers and its impact on the neutrino mass sensitivity. *Astroparticle Physics*, 41(0):52 – 62, 2013.

[52] S. Görhardt. Reduktion der durch radon induzierten untergrundprozesse in den katrin spektrometern. http://www.katrin.kit.edu/publikationen/dth-goerhardt.pdf, 2010. [Online; accessed 27-08-2013].

[53] F.M. FrÃ¤nkle, L. Bornschein, G. Drexlin, et al. Radon induced background processes in the katrin pre-spectrometer. *Astroparticle Physics*, 35(3):128 – 134, 2011.

[54] Howe, M. A. *et al. TUNL Progress Report*, XLVIII:179, 2009.

[55] Saint-Gobain Crystals. Premium plastic scintillators. http://www.detectors.saint-gobain.com/uploadedFiles/SGdetectors/Documents/Product_Data_Sheets/BC400-404-408-412-416-Data-Sheet.pdf, 2005. [Online; accessed 11-07-2013].

[56] Kevin Wierman. personal conversation, 2013.

[57] Myer Kutz. *Eshbach's Handbook of Engineering Fundamanetals.* Wiley, 2009.

[58] T. Tsang. *Classical Electrodynamics.* Advanced Series on Theoretical Physical Sciences. World Scientific, 1997.

[59] O.C. Allkofer. *Introduction to cosmic radiation.* Karl Thiemig, 1975.

[60] Manfred Klemann. pressure and temperature data from wetter.com. http://www.wetter.com/wetter_aktuell/rueckblick/?id=DE0005309, 2012.

[61] M. Asda. Katrin sds measurements - proposal m12. http://www.katrin.kit.edu, 2013.

[62] Henrik Arlinghaus. Investigation of the muon-induced secondary electron background in the katrin experiment. http://www.uni-muenster.de/Physik.KP/AGWeinheimer/Files/theses/Diplom_Henrik_Arlinghaus.pdf, 2009. [Online; accessed 21-08-2013].

Annex

A. ORCA air coil script

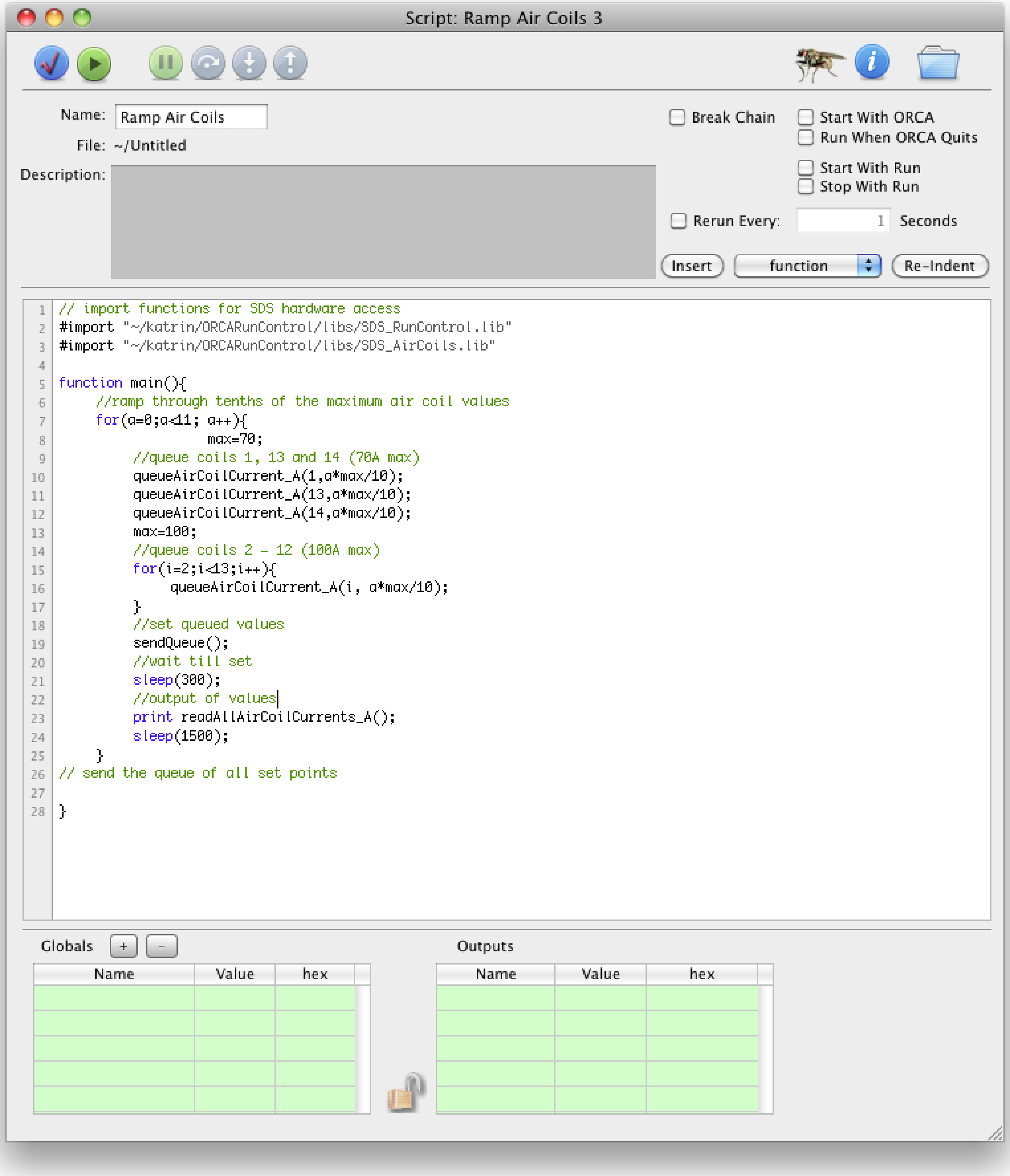

Figure A.1.: Scripting task through the example of a LFCS current ramping script. All currents are incremented in thenths of the maximum current for the individual coil.

Module	1A	1B	2A	2B	3A	3B	4A	4B
Card	3	3	3	3	6	6	6	6
Channel	0	14	3	7	0	14	3	7
Module	5A	5B	6A	6B	7A	7B	8A	8B
Card	6	6	8	8	8	8	8	8
Channel	9	23	0	14	3	7	9	23

Table B.1.: Assignment of main spectrometer module sides to FLT cards and their channels.

B. Connection scheme DAQ

C. Weather data Christmas 2012

Date	T_{low} [K]	T_{high} [K]	p_{low} [kPa]	p_{high} [kPa]	p_l / T_l	p_h / T_h
21.12.12	274.95	281.25	1010.10	1018.20	3.67	3.62
22.12.12	278.55	282.15	1009.50	1020.60	3.62	3.62
23.12.12	282.85	287.25	1009.50	1013.70	3.57	3.53
24.12.12	277.05	287.15	1007.40	1013.50	3.64	3.53
25.12.12	276.05	288.35	1004.00	1010.30	3.64	3.50
26.12.12	281.25	282.85	1010.40	1016.40	3.59	3.59
27.12.12	280.75	283.25	1004.80	1014.70	3.58	3.58
28.12.12	279.65	281.85	1016.20	1029.50	3.63	3.65
29.12.12	276.05	284.55	1014.90	1026.00	3.68	3.61
30.12.12	279.05	282.85	1015.90	1024.60	3.64	3.62
31.12.12	277.05	283.15	1011.60	1024.40	3.65	3.62
01.01.13	274.45	281.45	1008.10	1016.90	3.67	3.61
02.01.13	272.25	279.15	1017.50	1033.00	3.74	3.70
03.01.13	273.65	280.45	1033.10	1038.30	3.78	3.70

Table C.2.: Temperature and pressure data from the weather station in Rheinstetten. Daily high and low were given, included are the ratio of pressure and temperature for both the high and the low values. This ratio is proportional to the air's density . Bare in mind that this data is only for the low atmospheric layer and the station is also around 20 km away from the KATRIN muon modules.

D. Monitor spectrometer settings

non-axially symmetric magnetic field

solenoid source	solenoid detector	inner aircoil	outer aircoil	outer cent. aircoil	emcs x	emcs y
25	25	7	-7	5	0	-14

mos00159753-mos00159754	Two horizontal loops at 100 A
mos00159755-mos00159758	Two horizontal loops at −100 A
mos00159759-mos00159771	No current in horizontal loops - background measurement
mos00159772-mos00159773	Two horizontal loops at 100 A

solenoid source	solenoid detector	inner aircoil	outer aircoil	outer cent. aircoil	emcs x	emcs y
12.5	12.5	3.5	-3.5	2.5	0	0

mos00160661-mos00160666	Two horizontal loops at 50 A
mos00160667-mos00160682	No current in horizontal loops - background measurement
mos00160684-mos00160687	Two horizontal loops at −50 A

solenoid source	solenoid detector	inner aircoil	outer aircoil	outer cent. aircoil	emcs x	emcs y
6.2	6.2	1.7	-1.7	1.2	0	0

mos00160688-mos00160691	Two horizontal loops at 25 A
mos00160692-mos00160706	No current in horizontal loops - background measurement
mos00160707-mos00160711	Two horizontal loops at −25 A

E. Monitor spectrometer field setup and analysis

For all settings see 5.5, line 1.

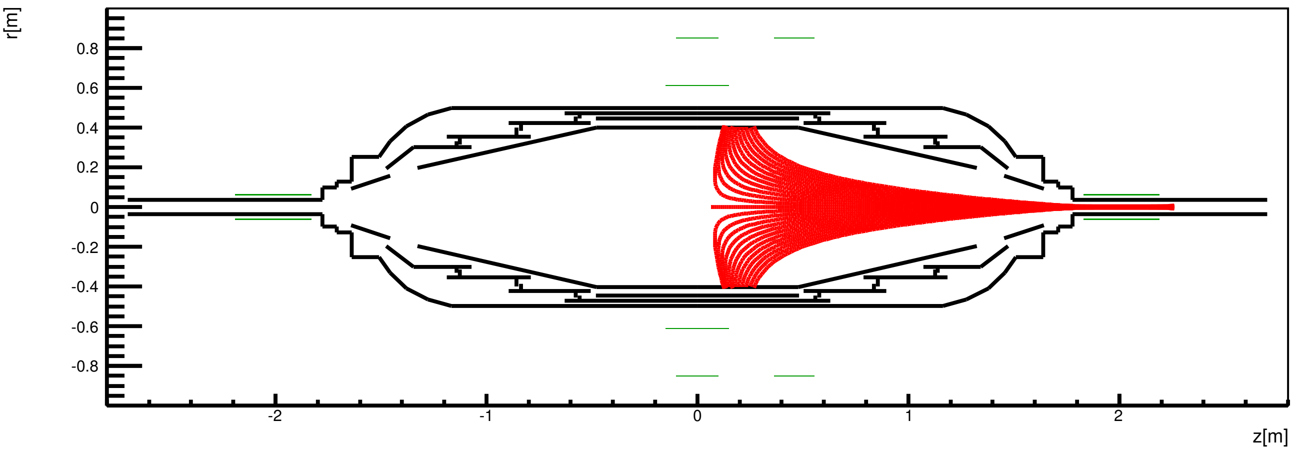

Figure E.2.: Flux tube for a 50 A detector solenoid, -8 A outer central air coil current.

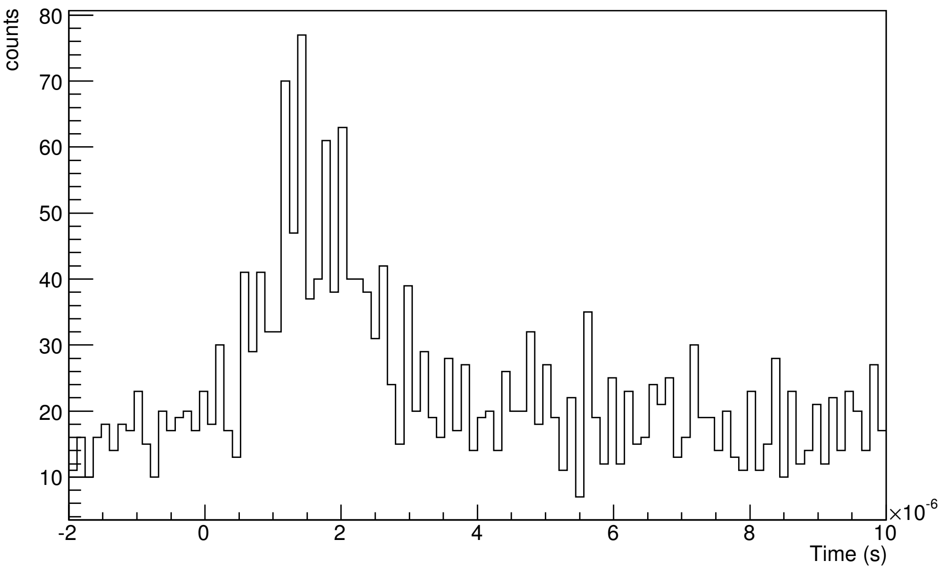

Figure E.3.

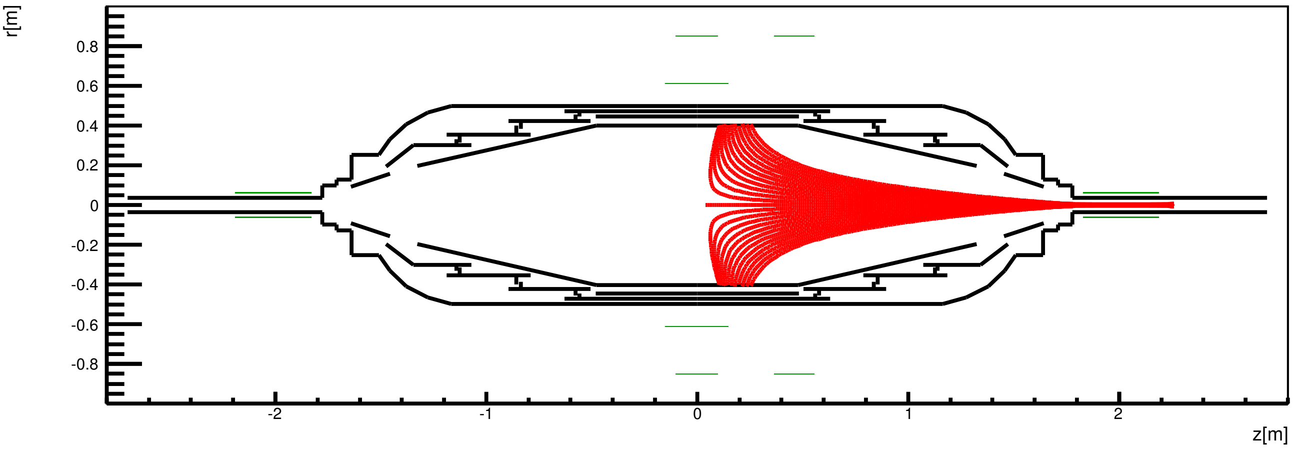

Figure E.4.: Flux tube for a 25 A detector solenoid.

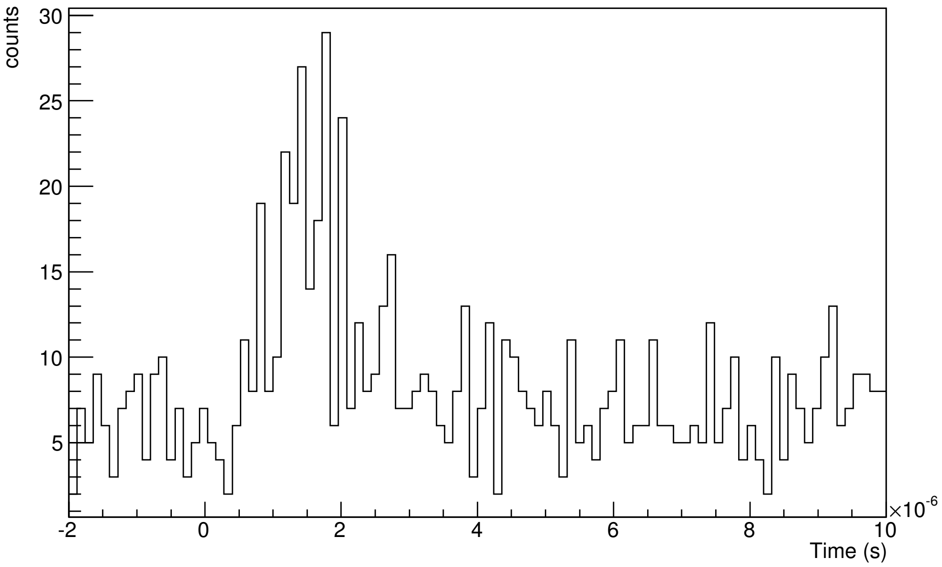

Figure E.5.: Source solenoid off, detector solenoid at 25 A

.

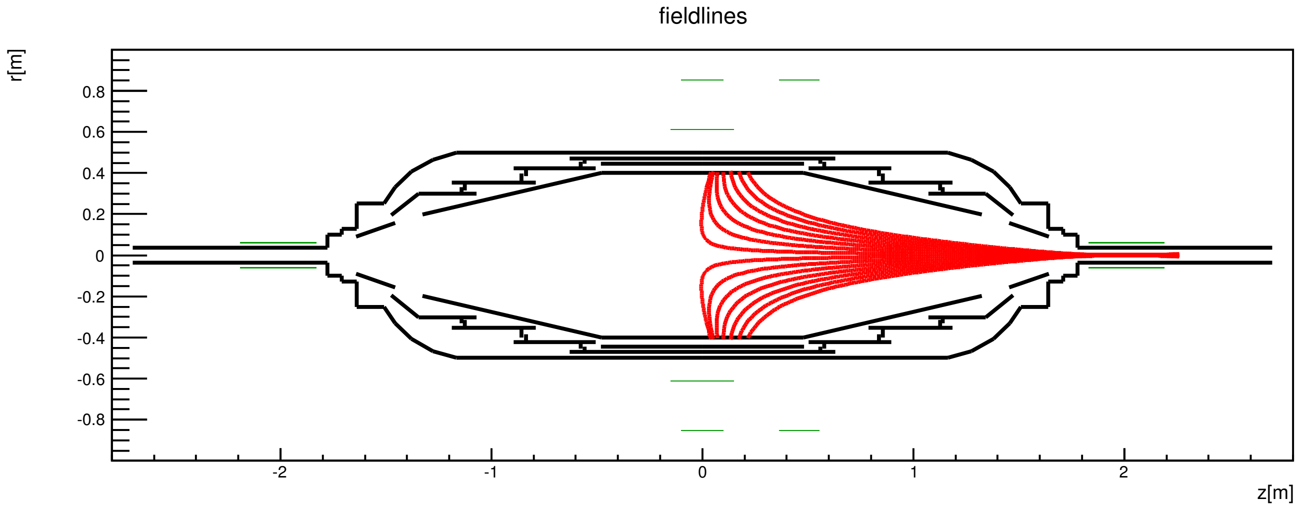

Figure E.6.: Flux tube for a 50 A detector solenoid, −7 A outer central air coil current.

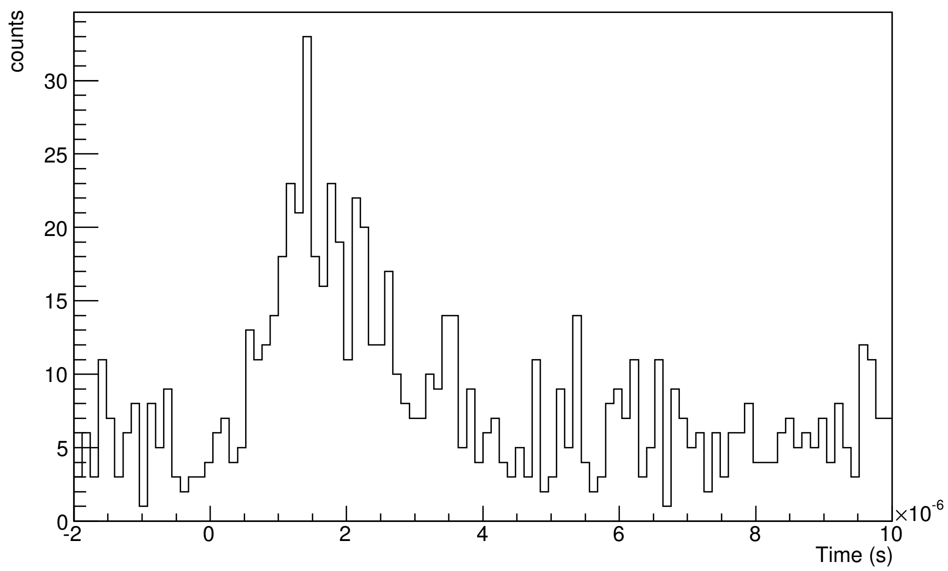

Figure E.7.: Two horizontal loops at 0 A current. Both solenoids at 25 A.

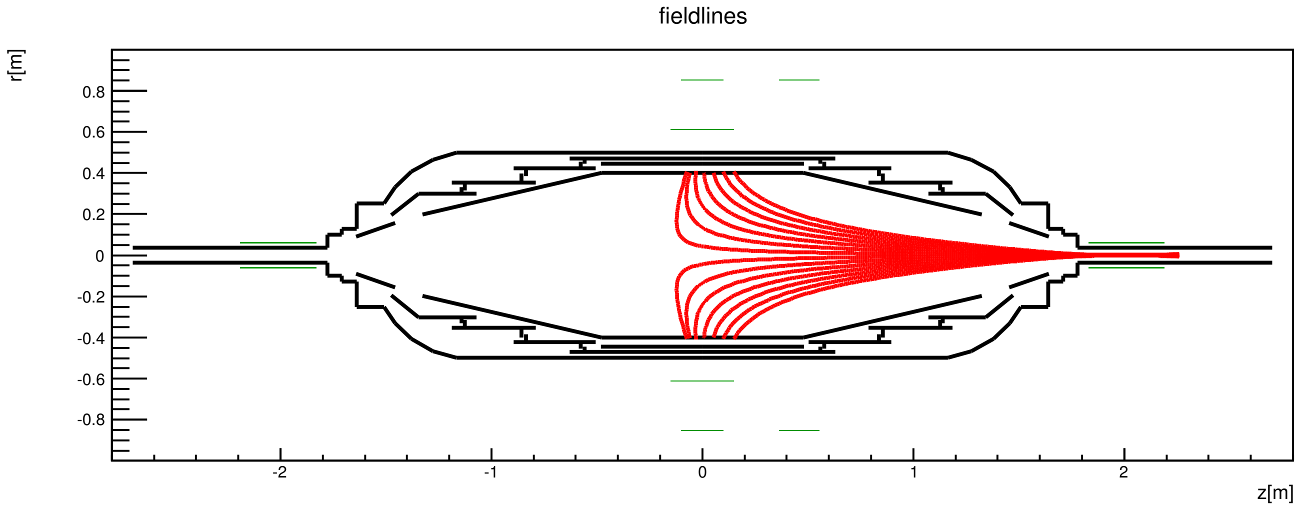

Figure E.8.: Flux tube for a 50 A detector solenoid, −6 A outer central air coil current.

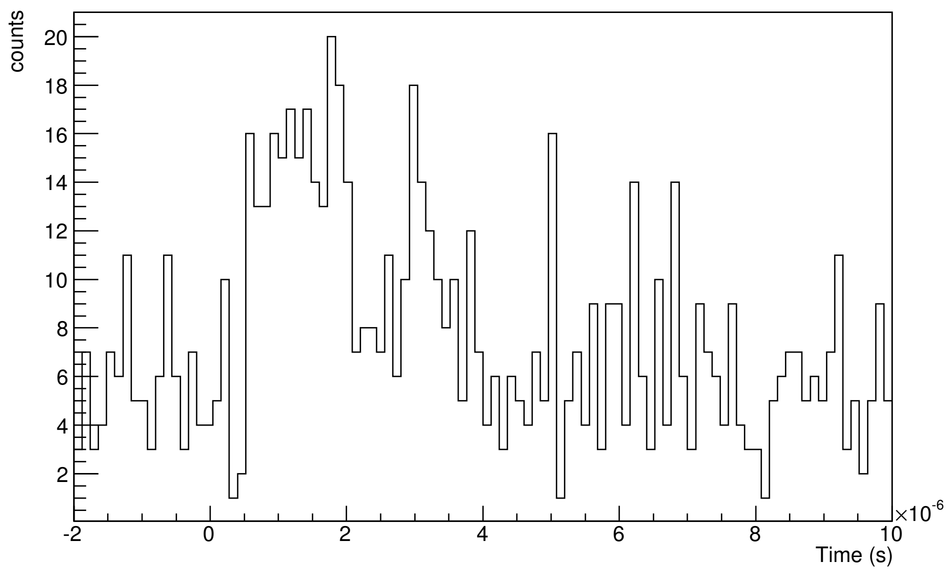

Figure E.9.: Two horizontal loops at 0 A current. Both solenoids at 25 A.

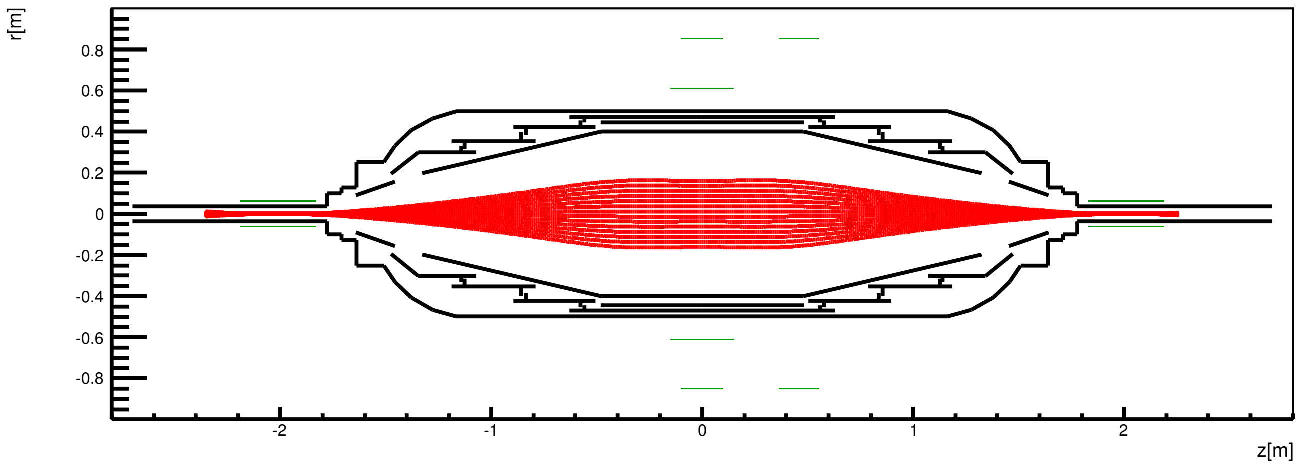

Figure E.10.: Two horizontal loops at 0 A current. Both solenoids at 25 A for a comparison of the background at different field widening.

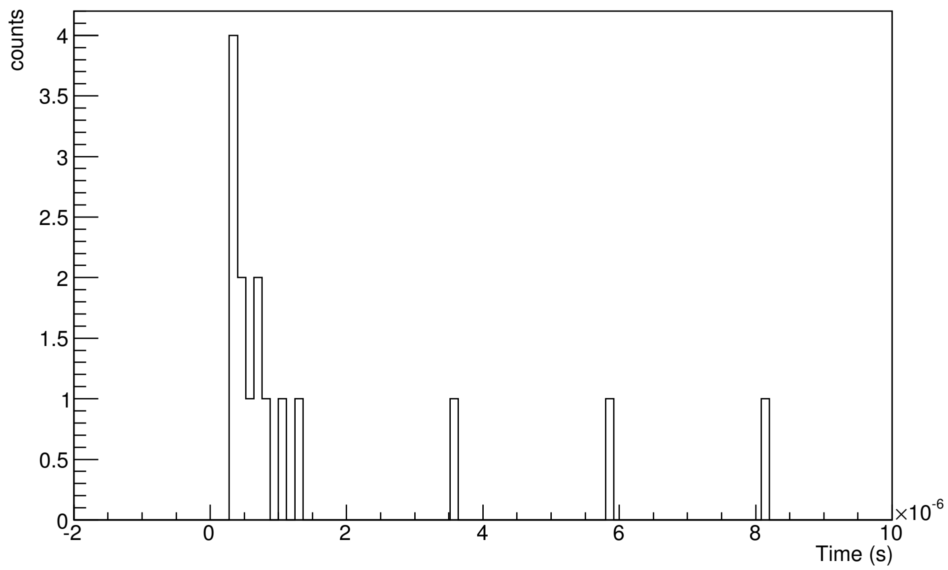

Figure E.11.: Two horizontal loops at 0 A current. Both solenoids at 25 A for a comparison of the background at different field widening. Some events occur in the expected time window.

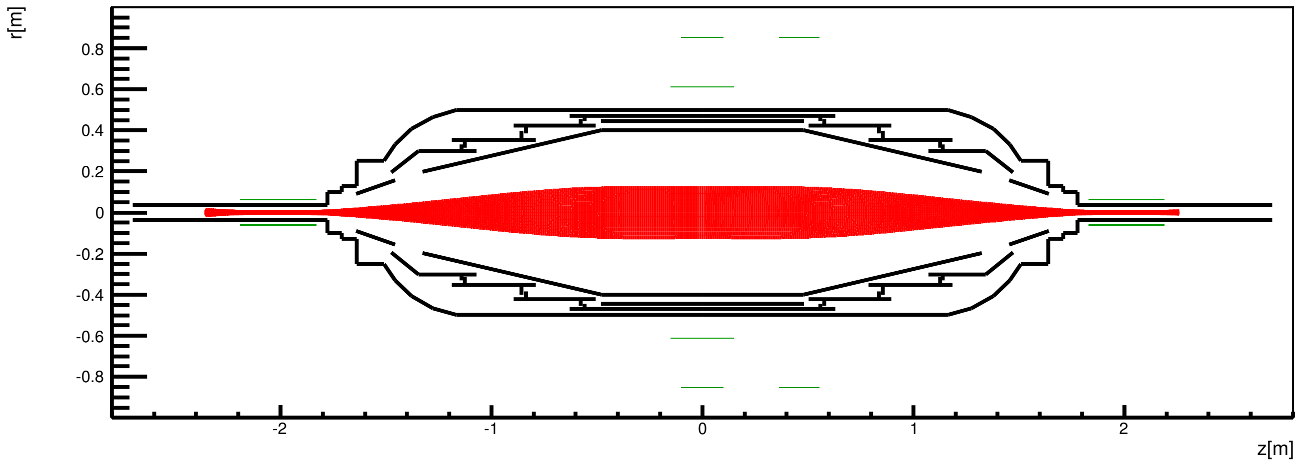

Figure E.12.: Two horizontal loops at 0 A current. Both solenoids at 12.5 A for a comparison of the background at different field widening.

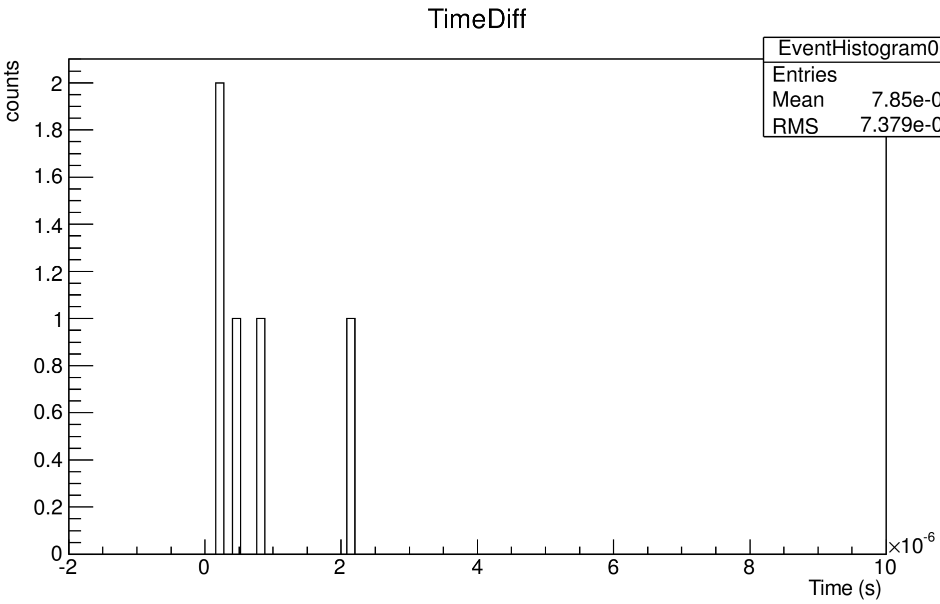

Figure E.13.: Two horizontal loops at 0 A current. Both solenoids at 12.5 A for a comparison of the background at different field widening.

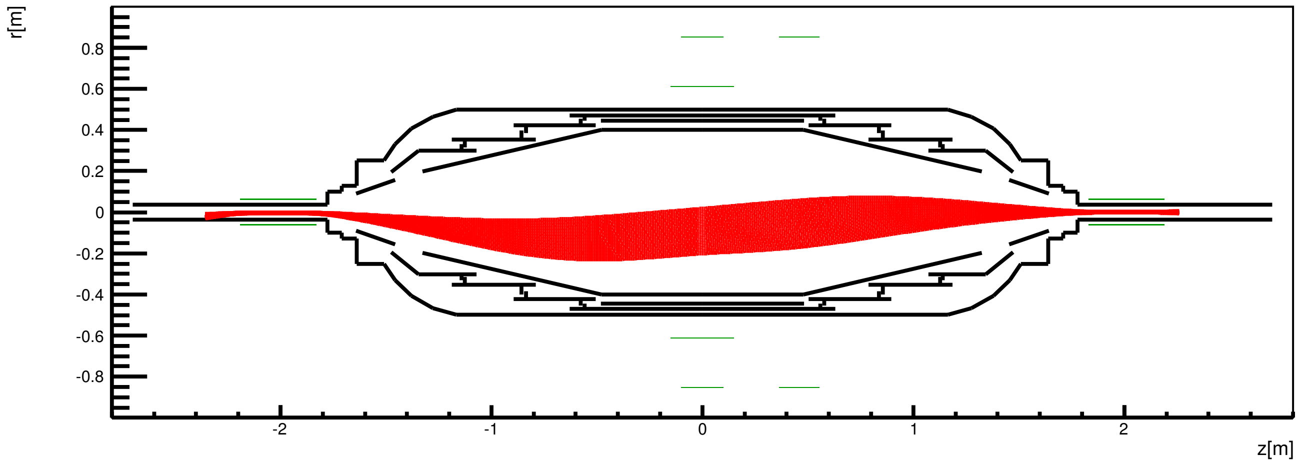

Figure E.14.: Two horizontal loops at 50 A current. Both solenoids at 12.5 A. Shift of the flux tube downwards visible.

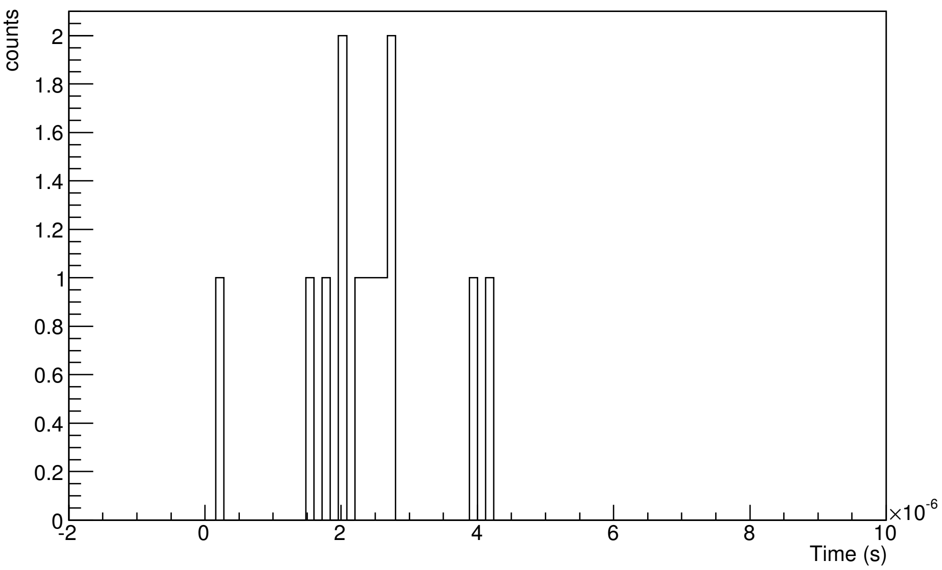

Figure E.15.: Two horizontal loops at 50 A current. Both solenoids at 12.5 A

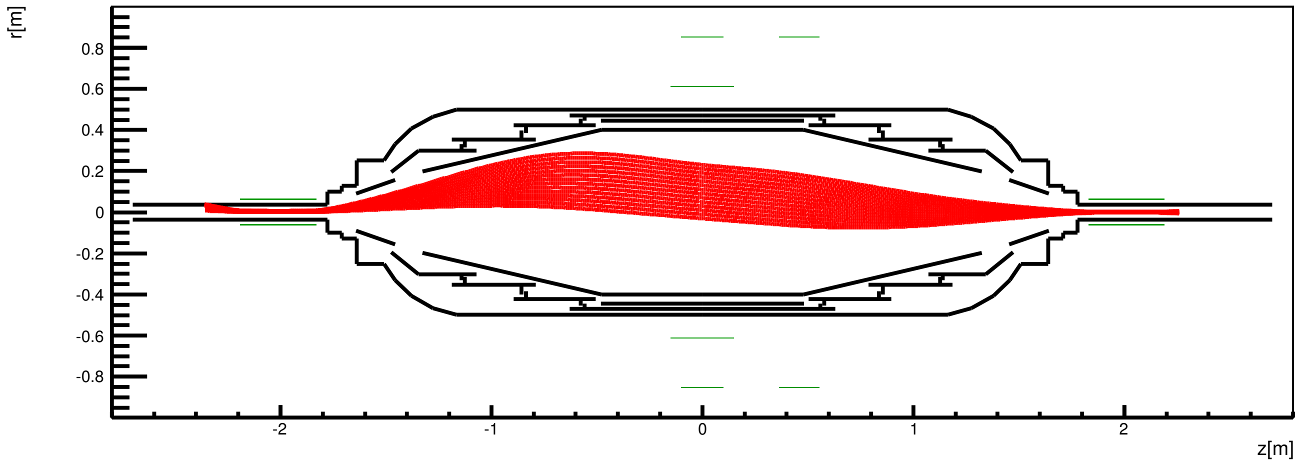

Figure E.16.: Two horizontal loops at −50 A current. Both solenoids at 12.5 A. Shift of the flux tube upwards visible.

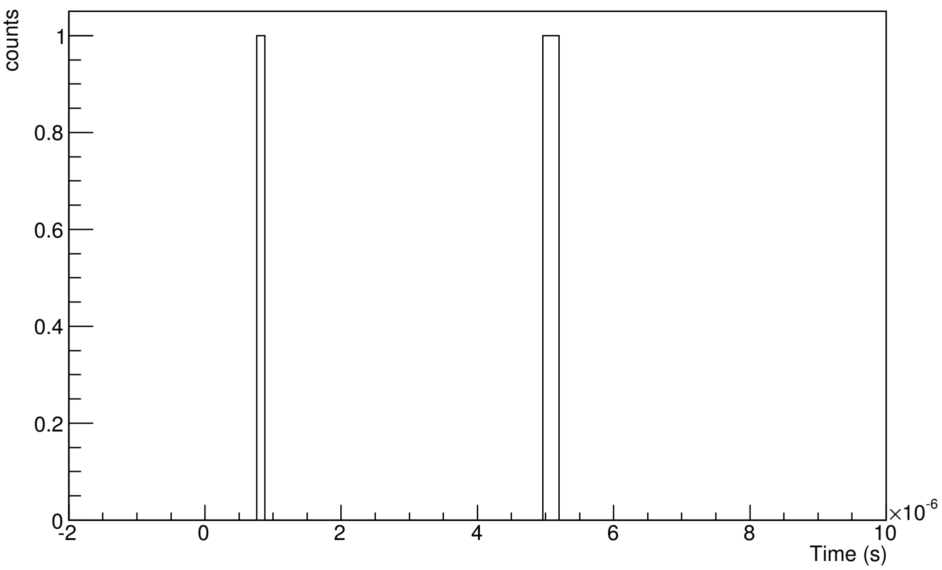

Figure E.17.: Two horizontal loops at −50 A current. Both solenoids at 12.5 A.

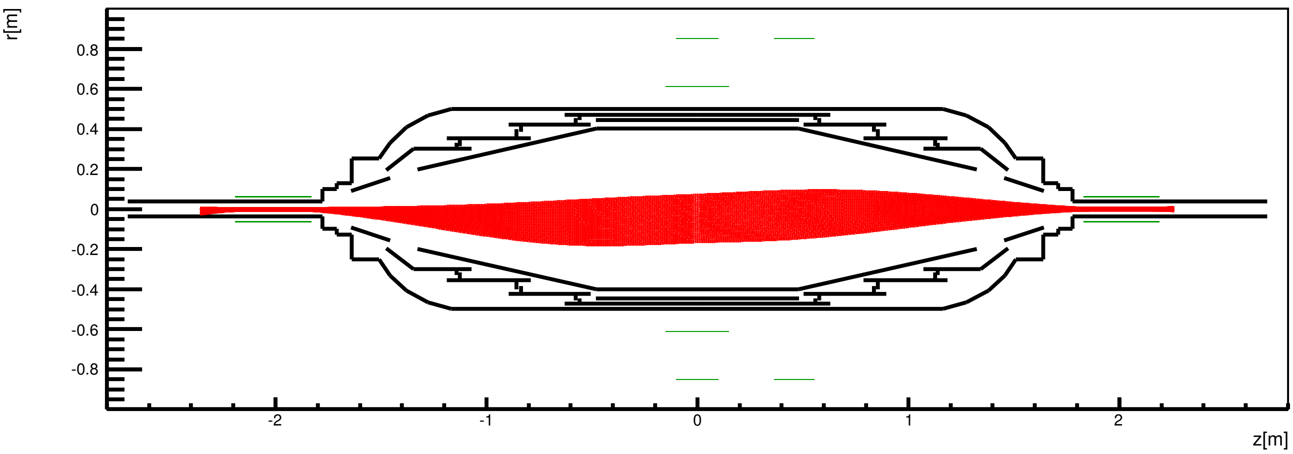

Figure E.18.: Two horizontal loops at 25 A current. Both solenoids at 12.5 A. Shift of the flux tube downwards visible.

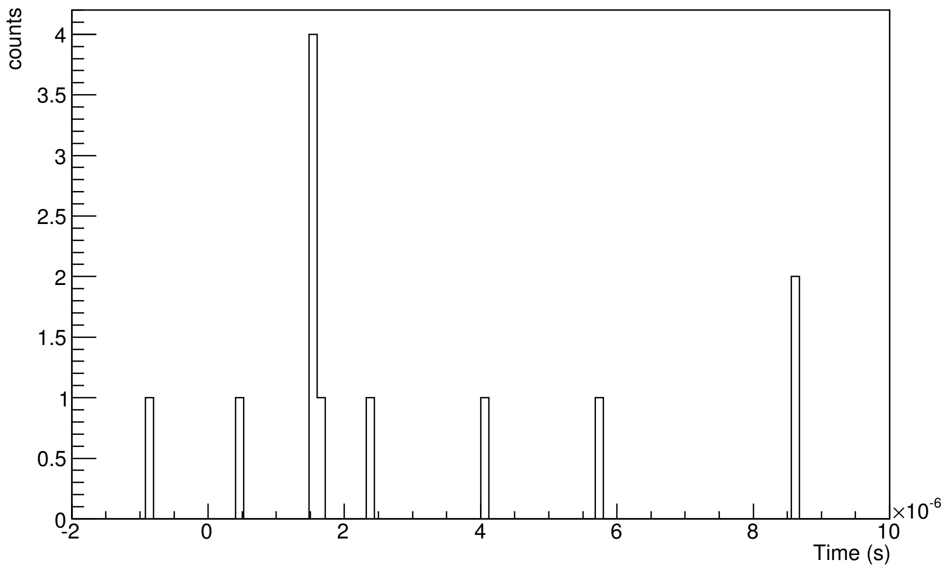

Figure E.19.: Two horizontal loops at 25 A current. Both solenoids at 12.5 A.

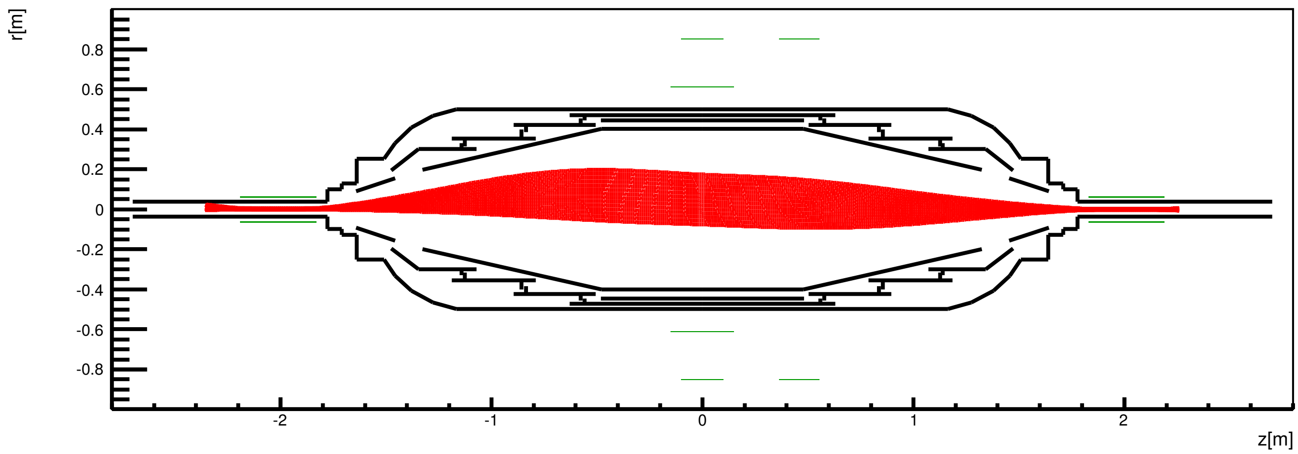

Figure E.20.: Two horizontal loops at 0 A current. Both solenoids at 25 A. Shift of the flux tube upwards visible.

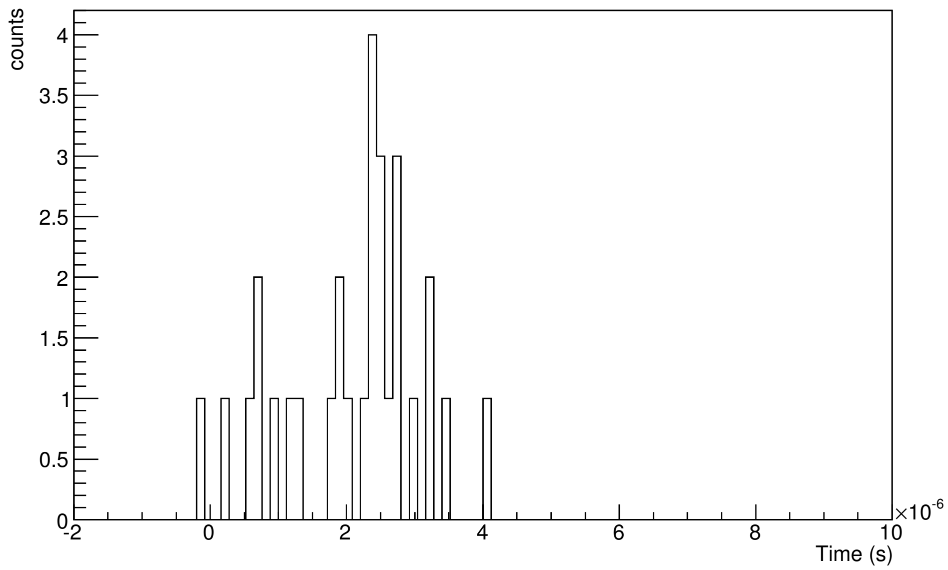

Figure E.21.: Two horizontal loops at 0 A current. Both solenoids at 25 A. Unexpectedly low counts probably due to a off-detector flux tube.

F. Main spectrometer analysis

G. A vis.mac file

```
# Macro file for the visualization setting in the initialization phase
# of the Geant4 simulation when running in interactive mode
#
# Use this open statement to create an OpenGL view:
/vis/open OGL 600x600-0+0
#
# Disable auto refresh and quieten vis messages whilst scene and
# trajectories are established:
/vis/viewer/set/autoRefresh false
/vis/verbose warnings
#
# Draw geometry:
/vis/drawVolume
#
# Specify view angle and zoom:
/vis/viewer/set/viewpointVector 0 0 1
#/vis/viewer/set/viewpointThetaPhi 40 40
/vis/viewer/zoomTo 2
#
# Specify style (surface, wireframe, auxiliary edges, display limit...)
/vis/viewer/set/style wireframe
/vis/viewer/set/auxiliaryEdge true
/vis/ogl/set/displayListLimit 100000000
#
# Draw smooth trajectories at end of event, showing trajectory points
# as markers 1 pixel wide:
/vis/scene/add/trajectories smooth
/vis/modeling/trajectories/create/drawByCharge
/vis/modeling/trajectories/drawByCharge-0/default/setDrawStepPts true
/vis/modeling/trajectories/drawByCharge-0/default/setStepPtsSize 1
#
# Draw hits at end of event:
/vis/scene/add/hits
#
# To draw only muons:
/vis/filtering/trajectories/create/particleFilter
/vis/filtering/trajectories/particleFilter-0/add mu+
# To superimpose all of the events from a given run:
/vis/scene/endOfEventAction accumulate
#
# Re-establish auto refreshing and verbosity:
/vis/viewer/set/autoRefresh true
/vis/viewer/set/background grey
/vis/viewer/set/projection perspective
/vis/verbose warnings
#
#Generate 5 muon events with the distribution provided in the code
/run/beamOn 5
```

Danksagung

Bei der Entstehung dieser Arbeit hatte Unterstüstzung von zahlreichen Personen, ohne die ich die Vielzahl an Aufgaben nicht in diesem Umfang hätte bearbeiten können.

Ich danke Prof. Drexlin dafür, meine Diplomarbeit am Großprojekt KATRIN schreiben zu dürfen und dafür, durch eine interessante Vorlesung mein Interesse an Teilchenphysik geweckt zu haben.

Ich danke Prof. Husemann für das Interesse an meiner Arbeit und die Übernahme der Zweitkorrektur.